공학박사 학위논문

Synthesis of heterostructured oxide nanomaterials and their application to catalyst

이종구조 산화물 나노입자의 합성과 촉매로의 응용

2022 년 8 월

서울대학교 대학원

화학생물공학부

조진웅

Synthesis of heterostructured oxide nanomaterials and their application to catalyst

지도 교수 현택환

이 논문을 공학박사 학위논문으로 제출함
2022 년 8 월

서울대학교 대학원
화학생물공학부
조진웅

조진웅의 공학박사 학위논문을 인준함
2022 년 8 월

위 원 장 _____ 성영은 _____ (인)

부위원장 _____ 현택환 _____ (인)

위 원 _____ 김대형 _____ (인)

위 원 _____ 유성종 _____ (인)

위 원 _____ 유승호 _____ (인)

Abstract

Synthesis of heterostructured oxide nanomaterials and their application to catalyst

Jinwoung Jo

School of Chemical and Biological Engineering

The graduate School

Seoul National University

In the past decade, heterogeneous oxide nanocrystals, which combine two or more distinct oxides in one nanocrystal, have been synthesized through colloidal synthesis with heterogeneous nucleation to improve the intrinsic properties of earth-abundant oxide nanomaterials. By controlling the unique interfacial structures in heterogeneous oxide nanocrystals, highly active oxide nanocatalysts for electrocatalytic reactions, industrial gas-phase reactions, organic reactions, and photocatalytic reactions can be generated. This dissertation presents the synthesis of interface-controlled Co_3O_4/CeO_2 and facet-defined $Co_3O_4/Co_yMn_{1-y}O_x$ for

CO oxidation reaction and electrocatalytic oxygen reduction reaction respectively.

Firstly, a novel synthetic procedure for Co_3O_4, Mn_3O_4, and Fe_3O_4 nanocubes (NCs) with a controlled CeO_2 layer enables exploration of the role of the interface in catalytic oxidation. Notably, CeO_2-deposited Co_3O_4 NCs presents up to 12 times higher CO oxidation rate than the pristine Co_3O_4 NCs. In situ characterization corroborates that the deposited CeO_2 hinders the reduction of Co_3O_4 by replenishing oxygen. The maximized interface formation in Co_3O_4 NCs with three facets covered by CeO_2 layers results in the highest CO oxidation rate even under O_2-deficient conditions, which resulted from the versatile variation in the oxidation state. This study gives a deep understanding of the Mars−van Krevelen mechanism occurring on the nanoscale at the Co_3O_4−CeO_2 interfaces. The same activity trend and hot electron flow are observed for H_2 oxidation reactions utilizing catalytic nanodiodes, thereby showing that the origin of the activity enhancement is charge transfer at the interface.

Secondly, (001) facet-defined Co−Mn spinel oxide surface with diverse surface compositions is synthesized through epitaxial growth on Co_3O_4 nanocube template. Composition gradient synthesis to alleviate the strain layer by layer minimizes the surface strain effect on catalytic activity. In this system, experimental and calculational inspection of model oxygen reduction reaction (ORR) activity discloses a volcano-like trend with Mn/Co ratios because of an adequate charge transfer from octahedral-Mn to

neighboring Co. $Co_{0.5}Mn_{0.5}$ as an optimized Mn/Co ratio exhibits both distinctive ORR activity (0.894 V vs RHE in 1 M KOH) and stability (2% activity loss against chronoamperometry). By controlling facet and strain, this study delivers a well-defined platform for investigating composition−structure− activity relationships in electrocatalytic processes.

Keywords: oxide, heterostructure, catalyst, nanomaterials, spinel, interface

Student number: 2016-22356

Contents

Chapter 1. Review for Recent Advances in the Synthesis of Heterostructured Oxide Nanomaterials and their Application on Catalysis 1

1.1. Introduction 1

1.2. Synthesis of Heterostructured Oxide Nanocrystals 9

1.3. Application of Heterostructured Oxide Nanocrystals for Catalytic Applications. 17

1.3.1. Electrocatalytic Reactions 17

1.3.2. Industrial Gas Phase Reactions. 26

1.3.2. Photocatalytic Reactions. 30

1.4. Dissertation Overview 33

1.5. References 35

Chapter 2. Revealing Charge Transfer at the Interface of Spinel Oxide and Ceria during CO Oxidation 42

2.1. Introduction 42

2.2. Materials and Methods 45

2.2.1. Chemicals 45

2.2.2. Synthesis of Spinel Oxide NCs. 45

2.2.3. Selective Deposition of CeO_2 on the Oxide NCs. 46

2.2.4. Preparation of the Monolayer Films using the Langmuir-Blodgett Technique. 46

2.2.5. Catalytic CO Oxidation 47

2.2.6. Characterization. 48

2.2.7. In Situ XRD, XAS, and NAP-XPS 49

2.2.8. Catalytic H_2 Oxidation on a Nanodiode. 50

2.3. Results and Discussions. 52

2.3.1. Spinel Oxide NCs with Controlled CeO_2 Layers by Selective Deposition. 52

2.3.2. Catalytic CO Oxidation. 68

2.3.3. Changes in the Crystal Structure under Different Reaction Conditions. 78

2.3.4. Changes in the Oxidation State under Different Reaction Environments.. 84

2.3.5. Hot Electron Detection at the Co_3O_4-CeO_2 Interface. 95

2.4. Conclusions 100

2.5. Referneces 102

Chapter 3. Facet-Defined Strain-Free Spinel Oxide for Oxygen Reduction 107

3.1. Introduction 107

3.2. Experimental Section 110

3.2.1. Synthesis of template spinel oxide nanocubes 110

3.2.2. Synthesis of Co_3O_4@$Co_yMn_{1-y}O_x$ and Mn_3O_4@$Co_yMn_{1-y}O_x$ core-shell nanocubes. 110

3.2.3. Synthesis of Co_3O_4@Mn_3O_4 core-shell nanocrystals 111

3.2.4. Characterizations. 111

3.2.5. Electrochemical characterization 113

3.2.6. Computational Details. 114

3.2.7. Computational Models of Spinel Oxides 115

3.3. Results and Discussions. 122

3.3.1 Structural characterization of spinel Co_3O_4@$Co_yMn_{1-y}O_x$ core-shell nanocubes. 122

3.3.2 Charge distribution between Co and Mn in $Co_yMn_{1-y}O_x$ shell structure. 141

3.3.3. Composition-structure-correlation with alkaline ORR activities on Co-Mn spinel surface 151

3.3.4. Theoretical investigation of structure-activity correlation on $Co_yMn_{1-y}O_x$ spinel surface 166

3.4. Conclusions 169

3.5. Referneces 170

Bibliography 177

Abstract in Korean 180

List of Tables

Table 2.1 Calculated TOFs of Co_3O_4-CeO_2 NCs at different CO oxidation conditions.. 76

Table 2.2 Calculated TOFs of Mn_3O_4-CeO_2 NCs in CO oxidation 77

Table 3.1 Free energy correction values for adsorbates and gaseous molecules.. 119

Table 3.2 The experimentally determined lattice parameters and *c/a* values for various Mn/Co ratio.. 120

Table 3.3 The interpolated lattice parameters and *c/a* values for various Mn/Co ratio.. 121

Table 3.4 Comparison of alkaline ORR activity and measurement conditions of various spinel oxide electrocatalysts.. 165

List of Figures

Figure 1.1 Inorganic nanomaterials and their unique properties for catalysis 5

Figure 1.2 Synthesis of unform-sized Fe_3O_4 nanocrystals using "heat-up" method which decomposing iron oleate precursor 6

Figure 1.3 Multimetallic oxide nanomaterials for cathode material of Li-ion battery. 7

Figure 1.4 Multimetallic oxide nanomaterials for cathode material of Li-ion battery. 8

Figure 1.5 Colloidal synthesis of oxide nanocrystals 14

Figure 1.6 Energetics and nucleation probability of heterogeneous nucleation. 15

Figure 1.7 Synthesis of heterostructured oxide nanocrystals with epitaxial growth. 16

Figure 1.8 Oxygen reduction reaction with Co_3O_4/Mn_3O_4 based nanomaterials.....21

Figure 1.9 Oxygen evolution reaction at the oxide nanomaterials 23

Figure 1.10 Oxygen evolution reaction with heterostructured oxide nanomaterials. 25

Figure 1.11 Effect of interface structure on catalysis. 28

Figure 1.12 Heterostructured oxide nanocrystals for CO oxidation. 29

Figure 1.13 Heterostructured oxide nanomaterials for photocatalytic

reactions.....32

Figure 2.1 Synthesis and characterization of the Co_3O_4-CeO_2 NCs.....56

Figure 2.2 Detailed electron microscopy images of the Co_3O_4/CeO_2 NCs 57

Figure 2.3 TGA analysis of Co_3O_4/CeO_2 NCs 58

Figure 2.4 . Powder X-ray diffraction (XRD) patterns of Co_3O_4-CeO_2 NCs with different CeO2 coverages 59

Figure 2.5 X-ray absorption spectroscopy (XAS) of Co_3O_4-CeO_2 NCs with different CeO2 coverages 60

Figure 2.6 TEM images of Co_3O_4-CeO_2 NCs generated by the coverage control according to the pH 61

Figure 2.7 TEM images of Co_3O_4-CeO_2 NCs generated by coverage control according to surfactant concentration.....62

Figure 2.8 TEM images of various Co_3O_4-CeO_2 NCs controlled by pH and surfactant concentration.....63

Figure 2.9 Structural characterization of the Mn_3O_4-CeO_2 NCs and the Fe_3O_4-CeO_2 NCs. 64

Figure 2.10 Fast Fourier Transform (FFT) patterns of Mn_3O_4/CeO_2 NCs and Fe_3O_4/CeO_2 NCs.....65

Figure 2.11 TEM images of Mn_3O_4/CeO_2 and Fe_3O_4/CeO_2 NCs.....66

Figure 2.12 Characterizations of nanoparticle monolayers prepared by the Langmuir-Blodget (LB).....70

Figure 2.13 CO oxidation for the Co_3O_4-CeO_2 NCs. CO oxidation results

.....71

Figure 2.14 CO oxidation results for the CoCe catalysts in a fixed bed reactor.....72

Figure 2.15 CO chemisorption measurement to determine the amount of Co_3O_4 sites.....73

Figure 2.16 TEM images of the spent catalysts after CO oxidation.....74

Figure 2.17 TOF values of Mn_3O_4-CeO_2 NCs for CO oxidation in the temperature range of 533–573 K.....75

Figure 2.18 *in situ* XRD for the Co_3O_4-CeO_2 NCs.....80

Figure 2.19 *In situ* XRD patterns of Co_3O_4-CeO_2 NCs in the temperature range of 323–773 K (25K increments) under 5% CO.....81

Figure 2.20 *In situ* XRD patterns of Mn_3O_4-CeO_2 NCs under 5% CO....82

Figure 2.21 *In situ* XRD patterns of Fe_3O_4-CeO_2 NCs under 5% CO.....83

Figure 2.22 Oxidation state changes of the Co_3O_4-CeO_2 NCs observed from XANES and NAP-XPS analyses in different reaction environments 87

Figure 2.23 *In situ* Co K-edge XANES results obtained in a reducing environment.....89

Figure 2.24 *In situ* Co K-edge XANES profiles.....90

Figure 2.25 Near ambient pressure X-ray photoelectron spectroscopy (NAP-XPS) Ce 3*d* spectra in CO environment at different temperatures.91

Figure 2.26 NAP-XPS Co 2*p* spectra in CO environment at different temperatures.....92

Figure 2.27 Raman spectra of Co_3O_4-CeO_2 NCs with the different CeO_2

coverage 93

Figure 2.28 Co_3O_4 NCs overcoated by CeO_2 layers 94

Figure 2.29 Hot electron detection at the Co_3O_4-CeO_2 interface 97

Figure 2.30 SEM images of the assembled Co_3O_4-CeO_2 NCs 98

Figure 2.31 I-V characteristics of Co_3O_4-CeO_2 NCs loaded an Au/TiO_2 Schottky nanodiode 99

Figure 3.1 Models for DFT calculation 118

Figure 3.2 TEM images of Co_3O_4 and Mn_3O_4 nanocubes 126

Figure 3.3 Synthesis of facet-defined Co_3O_4@$Co_yMn_{1-y}O_x$ core-shell nanocubes with composition gradient 127

Figure 3.4 . Procedures for atomic position picking 129

Figure 3.5 GPA analysis of $Co_{0.5}Mn_{0.5}$ nanocubes 131

Figure 3.6 Electron microscoping characterization of Co_3O_4@Mn_3O_4 nanocubes 132

Figure 3.7 EDS line scan of $Co_{0.5}Mn_{0.5}$ nanocubes 133

Figure 3.8 Surface Mn/Co control in facet-defined and strain-free spinel $Co_yMn_{1-y}O_x$ oxide surface 134

Figure 3.9 TEM images, EFTEM images, and size distribution of Co_3O_4@$Co_yMn_{1-y}O_x$ nanocubes 136

Figure 3.10 Ensemble characterization of Co_3O_4@$Co_yMn_{1-y}O_x$ nanocubes 137

Figure 3.11 TEM and EFTEM images of Mn_3O_4@$Co_yMn_{1-y}O_x$ nanocubes 138

Figure 3.12 Ensemble characterization of $Mn_3O_4@Co_yMn_{1-y}O_x$ nanocubes 139

Figure 3.13 EELS line scan of Mn $L_{2,3}$-edge and Co $L_{2,3}$-edge spectra of $Mn_3O_4@Co_{0.5}Mn_{0.5}$ nanocubes 140

Figure 3.14 Cation distribution on the facet-defined and strain-free spinel $Co_yMn_{1-y}O_x$ oxide surface 144

Figure 3.15 EELS line scan of the $Co_{0.25}Mn_{0.75}$ and $Co_{0.75}Mn_{0.25}$ nanocube 146

Figure 3.16 XPS spectra of $Co_3O_4@Co_yMn_{1-y}O_x$ nanocubes 147

Figure 3.17 XANES spectra of $Co_3O_4@Co_yMn_{1-y}O_x$ nanocubes 148

Figure 3.18 XPS spectra of $Mn_3O_4@Co_yMn_{1-y}O_x$ nanocubes 149

Figure 3.19 EXAFS spectra of $Co_3O_4@Co_yMn_{1-y}O_x$ and $Mn_3O_4@Co_yMn_{1-y}O_x$ nanocubes 150

Figure 3.20 ligand removal of nanocatalysts 154

Figure 3.21 Electrochemical analyses of $Co_3O_4@Co_yMn_{1-y}O_x$ nanocubes in 1 M KOH electrolyte 155

Figure 3.22 The correlation of Mn-redox potential and Mn valence state of $Co_3O_4@Co_yMn_{1-y}O_x$ nanocubes 156

Figure 3.23 CV curves of Co_3O_4, Mn_3O_4, and $Mn_3O_4@Co_yMn_{1-y}O_x$ nanocubes 157

Figure 3.24 ORR polarization curves of $Mn_3O_4@Co_yMn_{1-y}O_x$ nanocubes 158

Figure 3.25 ORR half-wave potentials and ORR mass activity at 0.9 V (vs.

RHE) of Co_3O_4@$Co_yMn_{1-y}O_x$ and Mn_3O_4@$Co_yMn_{1-y}O_x$ nanocubes 159

Figure 3.26 CV and ORR of $Co_{0.5}Mn_{0.5}$ electrocatalyst before and after 15 hours of chronoamperometry (CA) stability test.....160

Figure 3.27 Chronoamperometry measurements of Co_3O_4, Mn_3O_4, Co_3O_4@$Co_yMn_{1-y}O_x$ nanocubes, and Pt/C 161

Figure 3.28 TEM images and EFTEM mapping images of nanocubes after the reaction 162

Figure 3.29 XPS spectra of Co_3O_4@$Co_yMn_{1-y}O_x$ and Mn_3O_4@$Co_yMn_{1-y}O_x$ nanocubes after the reaction 164

Figure 3.30 DFT calculations to understand the origin of ORR activity trend 168

Chapter 1. Review for recent advances in the synthesis of heterostructured oxide nanomaterials and their application on catalysis

1.1. Introduction

Last few decades, inorganic nanocrystals, which are crystalline inorganic materials with nanometer-scale size, have been intensely studied due to their novel characteristics distinct from bulk materials (e.g. large surface to volume ratio, different optical properties from quantum confinement effect, and unique surface structures, Fig. 1.1). The advancement in characterization tools including transmittance electron microscopy (TEM) enables the development of nanomaterials with different sizes, shapes, crystallinity, and dispersion which have unique functionalities.[1] Semiconductors,[2] noble metals,[3] oxides,[4] perovskites,[5] chalcogenides,[6] phosphides,[7] and carbon-based materials[8] have been synthesized uniformly in nanoscale for various applications.

Among them, transition metal oxide nanomaterials have gotten attention from various fields of technology because of their multifunctionality with abundance in earth's crust. The composition, crystallographic structure, and electronic structure of metal oxide nanomaterials have been controlled by synthetic methods based on solid-state processes, chemical vapor deposition,

and chemical solution synthetic route.[9,10] Thanks to the advances in synthesis, uniform-sized oxide nanocrystals have been synthesized in large scale. For example, ultra-large-scale synthesis of spinel Fe_3O_4 nanocrystals in spherical shape was conducted in the colloidal solution with the chemical decomposition of iron oleate complex at high temperature (Fig. 1.2).[11] In addition, the morphologies of the uniformly synthesized oxide nanocrystals, whose exposing facets determine their functionalities such as catalytic activity, are adjusted from several syntheses.[12]

However, monometallic oxides themselves have the finite potential for diverse applications because of their limited controllability. Multimetallic oxide materials can further modify their properties by combining several distinct materials in one domain. The chemical and physical properties of multimetallic oxides follow their composition and degree of mixing.[13] Therefore, to use multimetallic nanomaterials in various fields of science and technology, noble synthetic approaches for multimetallic oxide nanocrystals are needed to tune their surface structure, shape, and size for tuning their electronic, optical, and magnetic properties.[14] For instance, single-crystalline nickel-rich alloyed spinel oxides of Co, Mn, and Ni with reversible planar gliding and microcracking are controlled in nanoscale as cathode material for Li-ion batteries (Fig. 1.3).[15]

Heterostructured oxide nanocrystals (HONs), which combine two or more materials with the discrete interface, are important multimetallic nanocrystals in scientific society because of the unique microstructures

formed near the interface. Because different electronic and crystallographic natures of two materials affect each other, new microstructures such as strained phase, cation vacancies, or oxygen vacancies which make HONs have distinct properties from original monometallic oxides are formed at the interface (Fig. 1.4).[16] For example, when two materials are epitaxially combined in one nanocrystal, lattice strain due to the lattice mismatch between two adjacent materials affects the surface atomic arrangement of the nanocrystal.[17] If the deposited material has a bigger lattice constant than the template one, the tensile strain will be exerted on the material, otherwise, compressive strain will be exerted. If the strain is too high, plastic deformation would occur to form defect structures including dislocation and stacking fault. Also, the charge transfer between two materials generates electron-deficient and electron-rich counterparts. For instance, at the interface of Co_3O_4 and Mn_3O_4, because the Co cations are prone to accept electrons from neighboring Mn cations, the oxidation state of electron-deficient Mn_3O_4 increases at the interface.[18] Likewise, fine-tuning the interface of HONs can give us noble properties that cannot be observed from the monometallic oxide nanomaterials.

Because of the unique interfacial structures of HONs, their enhanced optical, magnetic, and electronic properties are utilized for various applications such as optoelectronic devices, battery cathodes, and biomedical applications.[19,20] Among many applications, HONs are intensively studied as nanocatalysts due to their wide tunability by

controlling their interfacial structure, composition, and morphologies.[21] Because the majority of catalytic reactions occur at the surface of nanomaterials, the surface engineering of HONs is significant. The different atomic arrangement depending on the surface structure affects the adsorption of substrate and detachment of product during the catalytic reactions. Controlling the exposing facet of the HONs (e. g. (100), (110), and (111)), manipulation of surface strain, and generating surface defects are common techniques that are utilized for tuning the surface structure of HONs.[22] By synthesizing functional HONs suitable for each reaction, they could catalyze electrocatalytic, organic, and photocatalytic reactions.[23]

In this review, the synthetic method for heterostructured oxide nanocrystals will be presented. In addition, the catalytic applications of synthesized nanocrystals for electrocatalytic reactions, conventional gas-phase reactions, and photocatalytic reactions will be included.

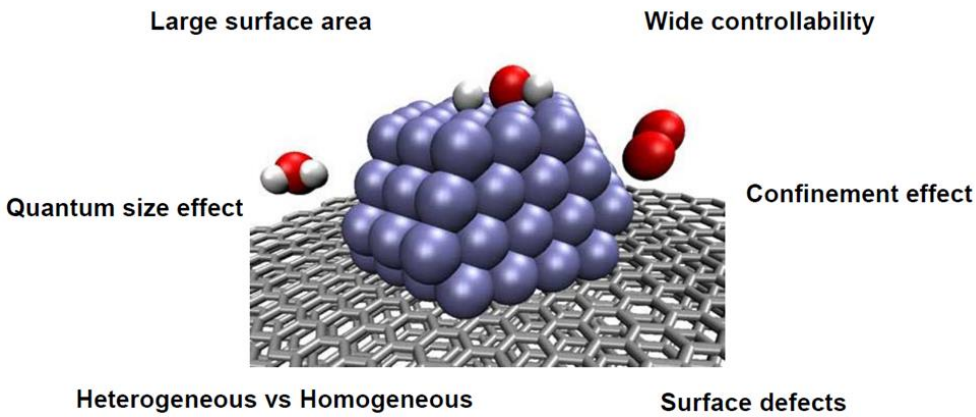

Figure 1.1 Inorganic nanomaterials and their unique properties for catalysis.

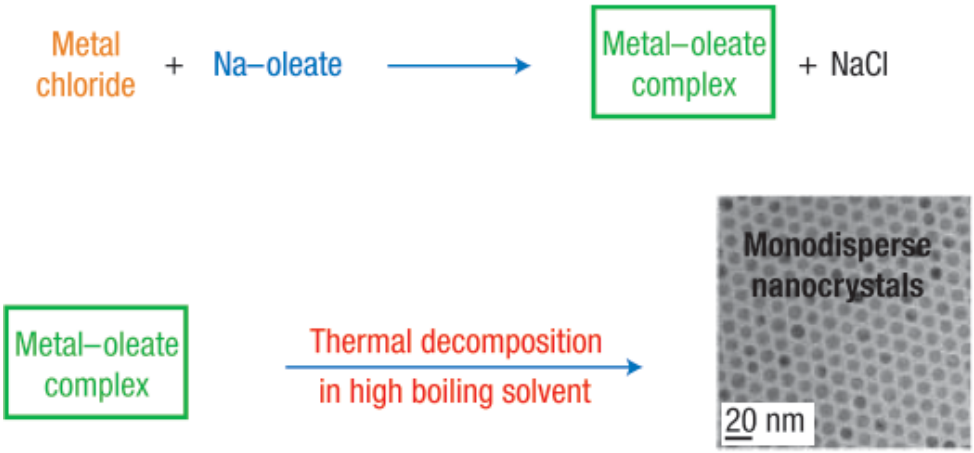

Figure 1.2 Synthesis of uniform-sized Fe_3O_4 nanocrystals using "heat-up" method which decomposing iron oleate precursor (from Ref. [11] Park, J.; An, K.; Hwang, Y.; Park, J.-G.; Noh, H.-J.; Kim, J.-Y.; Park, J.-H.; Hwang, N.-M.; Hyeon, T. *Nat. Mater.* **2004**, *3*, 891.)

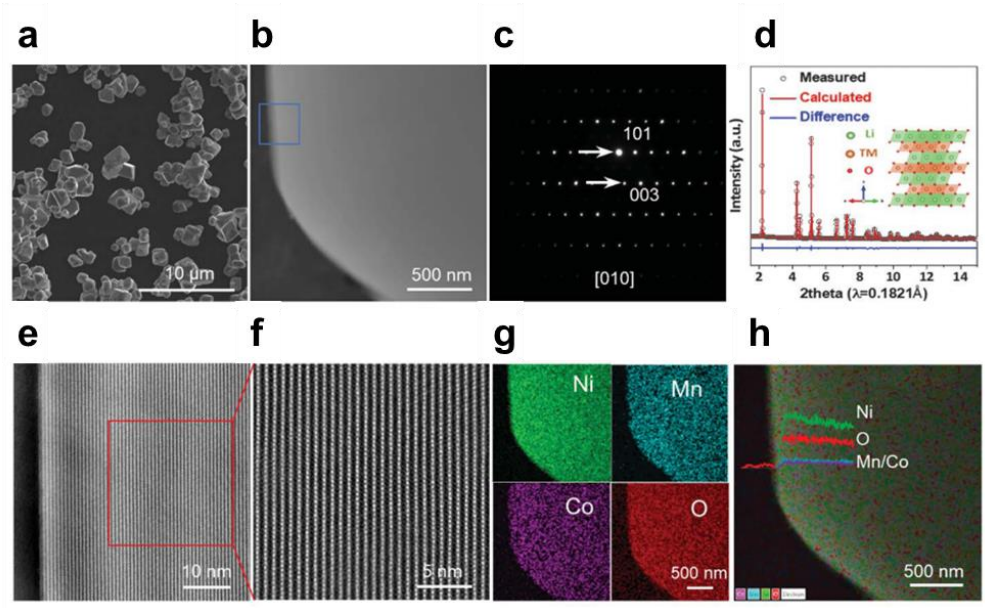

Figure 1.3 Multimetallic oxide nanomaterials for cathode material of Li-ion battery. (a-h) Electron microscopic studies show Co, Mn, Ni, and O are well mixed as one crystallographic phase. (from ref. [15] Bi, Y.; Tao, J.; Wu, Y.; Li, L.; Xu, Y.; Hu, E.; Wu, B.; Hu, J.; Wang, C.; Zhang, J.-G.; Qi, Y.; Xiao, J. *Science* **2020**, *370*, 1313.)

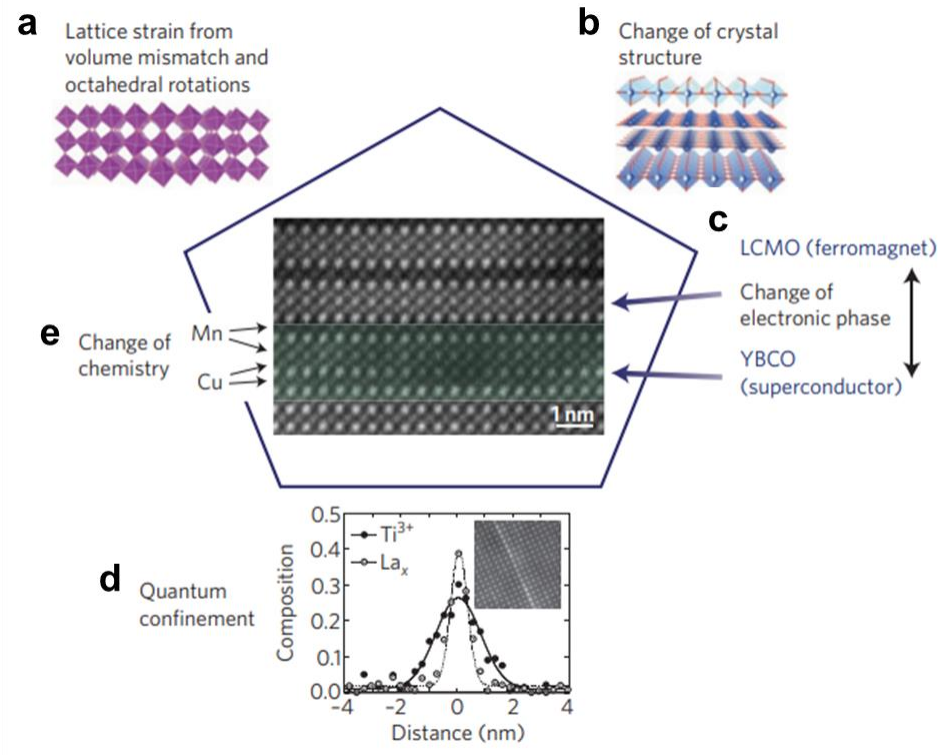

Figure 1.4 Oxide-oxide interface formation and their modified properties. (a) Elastic strain from rotations and mismatch. (b) Change in the crystal structure. (c) Change of electronic phase. (d) Charge confinement. (e) Change of valence state and chemical bonding. (from ref. [16] Chakhalian, J.; Millis, A. J.; Rondinelli J. *Nat. Mater.* **2012**, *11*, 92.)

1.2. Synthesis of heterostructured oxide nanocrystals

HONs have been synthesized through traditional synthesis following high-temperature solid-state method. In the last two decades, diverse low-temperature synthetic routes have been elaborated to produce oxide nanocrystals as template for HONs with different shapes and sizes. Colloidal synthesis of nanocrystals was utilized for finely tuned oxide nanocrystals in bottom-up synthesis.[24-27] Three different mechanisms are presented to explain the colloidal synthesis of uniform-sized nanoparticles: (i) classical nucleation and growth (LaMer plot), (ii) confined structure for nanoparticle synthesis, and (iii) a sol–gel process. In classical nucleation and growth, metal precursor, surfactant, and other reagents are dissolved in the same solution for the formation of well-dispersed nanocrystals. The process of monomer accumulation, burst nucleation, and diffusion-controlled growth intrigued by heating the solution is presented in the LaMer plot (Fig. 1.5a). The nuclei are formed when the monomer concentration surpasses the critical supersaturation lever. Then, diffusion-controlled growth occurs to form uniform-sized nanoparticles.

$$\frac{dr}{dt} = \frac{2\gamma D V_m^2 C_{flat}^0}{rRT}\left(\frac{1}{r^*} - \frac{1}{r}\right) \quad \text{..... (eq. 1)}$$

According to equation 1, diffusion-controlled growth invokes faster growth of smaller nanoparticles, resulting in uniformly synthesized nanoparticles. During the hot-injection and heat-up synthesis, surfactants in the solution

help diffusion-controlled growth of small nanoparticles to form uniformly sized oxide nanoparticles in large scale (Fig. 1.5b-d). Confined structures, reverse micelle as a representative, can act as a framework to synthesize uniform-sized nanoparticles (Fig. 1.5e). The reverse micelles formed by mixing organic solvents, long-chain surfactants, and water limit the particle size by making nanoreactors inside the small droplet. By controlling the water/surfactant ratio, the size and morphology of oxide nanoparticles could be controlled. The sol-gel process, polymerizing metal precursors to form metal-oxygen-metal bonds, can also be utilized to synthesize oxide nanocrystals (Fig. 1.5f). Various oxide materials can rapidly be synthesized from the sol-gel process, but unwanted gelation can result in nonuniform nanocrystals. Long-chain metal precursors are used to preventing the unwanted gelation process to produce uniform oxide nanocrystals. The resulting oxide nanocrystals from the colloidal synthesis are very uniform in their size, morphology, and structure, so these methods guarantee a finely tuned nanocrystal model for the study of catalysis.

The uniform nanocrystals can be used as templates to give us elaborately designed HONs.[28-32] Monometallic oxide nanocrystals which are synthesized with diverse morphologies, sizes, phases, and symmetries due to the advances in colloidal synthesis provide a well-defined template for synthesizing various HONs. Because heterogeneous nucleation can induce the formation of an additional oxide material at the surface of the template oxide nanoparticles with lower energy barriers, it enables the synthesis of

various HONs easily (Fig. 1.6).[32] Nuclei formation on the surface of the template nanocrystals during heterogeneous nucleation exhibit different energetical behaviors compared to that of homogeneous nucleation.

$$\Delta G_{hom}(r) = 4\pi r^2\gamma + \frac{4}{3\pi r^3 \Delta G_v} \quad \text{(eq. 2)}$$

$$\Delta G_{het} = \frac{8\pi\gamma^3 V_m^2}{3\left[RT\ln\left(\frac{a}{a_0}\right)\right]^2} \times h(m,x) \quad \text{(eq. 3)}$$

According to equations 2 and 3, the nucleus becomes more stable than the homogeneous one, resulting in a lower energy barrier for nucleation. Therefore, the synthesis of heterogenous nanocrystals can be conducted at a lower temperature with the relatively milder conditions. The contact angle for the nucleation also affects the heterogeneous nucleation of oxides by influencing not only thermodynamics (Gibbs free energy) but also kinetics (nucleation probability). By controlling these factors, the size and binding behavior of secondary oxides are determined. Using the reverse micelle techniques and sol-gel chemistry which are used in the synthesis of monometallic oxide nanocrystals, HONs were synthesized through heterogeneous nucleation and growth.

Oh *et. al.* reported the growth of Mn_3O_4 grains on the surface of the well-defined Co_3O_4 nanocubes in reverse micelle solution (Fig. 1.7a).[33] The epitaxial growth of Mn_3O_4 due to the similar crystallographic structure and lattice distance between the two materials makes the growth direction of

Mn_3O_4 is determined by the surface structure of the Co_3O_4 template. The Mn_3O_4 grains are grown only in <001> direction on 6 facets of Co_3O_4 template nanocubes, inducing grain boundary formation at the corner. Because Mn_3O_4 has tetragonal symmetry, the geometric misfit at the corner grain boundary results in a new type of defect which is called disclination. The Mn_3O_4 unit cell at the corner suffers elastic distortion which is confirmed by advanced transmittance electron microscopy (TEM) studies.

Though two materials do not have the same crystallographic structure, the epitaxial growth occurs during the formation of HONs. Fig. 1.7b shows epitaxial growth of Mn_3O_4 on CeO_2 nanopolyhedra though the two materials do not have the same crystallographic phase.[34] However, to reduce the mismatch at the interface, a relatively large surface strain (~13%) is mechanically induced on the surface Mn_3O_4. The highly strained Mn_3O_4 surface has lots of oxygen vacancy sites, which act as a highly catalytic antioxidant that can protect tissue-resident stem cells from irradiation-induced ROS damage.

Not only epitaxial growth, but non-epitaxial growth of oxide material on the template is possible when two materials have completely mismatched crystallographic structures. Heterogeneous nucleation of additional oxide also can occur without epitaxial growth. Amorphous SiO_2 could be deposited on several spinel oxides for biomedical and catalytic applications. Sol-gel chemistry which involves the polymerization of SiO_2 governs the

overall morphology, thickness, and porosity of SiO_2 attached to the template nanomaterials.[35,36] Silicon precursors with long-chain ligand (e. g. tetraethyl-ortho-silicate, TEOS) are used to maintain the uniformity of the HONs. Because of the different crystallographic structures of SiO_2 and template oxides, preventing homogeneous nucleation of SiO_2 by fine-tuning of reaction conditions is crucial to synthesizing HONs. The synergistic effect of oxide composites by forming a new nanointerface is beneficial for various catalytic reactions, biomedical imaging, therapeutic diagnosis, and drug delivery system.[37]

Non-colloidal routes to synthesize HONs are also possible to generate active HONs in large scale. Because colloidal synthesis requires a solution process with multiple components, scale-up of the synthesis is difficult. Several solid-state chemistries can be applied to develop novel synthetic procedures for HONs. For example, consequent synthesis of the template and secondary oxide nanomaterials by mixing precursors in basic conditions with high pressure and temperature gives HONs in large scale.[38] Also, electrodeposition of additional oxide to template oxide can generate finely-tuned HONs for electrochemical energy storage devices.[39] However, the synthesis of uniform-sized HONs is difficult with those methods.

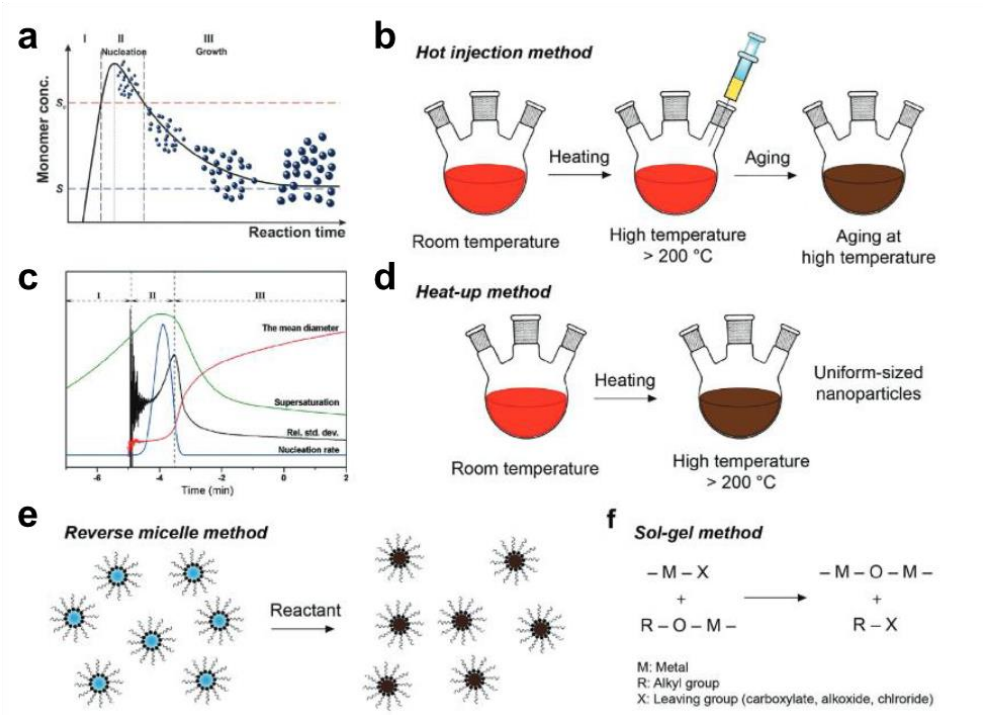

Figure 1.5 Colloidal synthesis of oxide nanocrystals. (a) LaMer plot explaining the formation mechanism of nanoparticles with uniform sizes. (b) Schematic illustration of the hot injection method. (c) A simulation which shows burst nucleation and separated growth during the formation process of oxide nanoparticles using the heat-up method. (d) Schematic illustration of the heat-up method. (e) Schematic illustration of the reverse micelle method. f) Mechanism of the sol–gel process. (from ref. [24] Kwon, H. J.; Shin, K.; Soh, M.; Chang, H.; Kim, J.; Lee, J.; Ko, G.; Kim, B. H.; Kim, D.; Hyeon, T. *Adv. Mater.* **2018**, *30*, 1704290.)

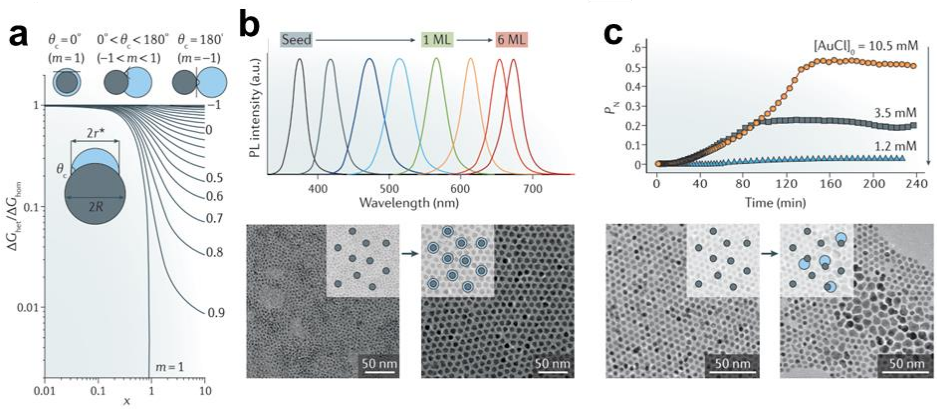

Figure 1.6 Energetics and nucleation probability of heterogeneous nucleation. (a) The behavior of Gibbs free energy during heterogeneous nucleation process. (b) Temporal changes of photoluminescence spectra and their TEM images of ZnSe-CdSe core-shell nanoparticles during shell formation. (c) Nucleation probability as a function of reaction time for $CoPt_3$-Au nanodumbbells synthesized with different concentrations of the gold precursor. (from ref. [32] Lee, J.; Yang, J.; Kwon, S. G.; Hyeon, T. *Nat. Rev. Mater.* **2016**, *1*, 1-16.)

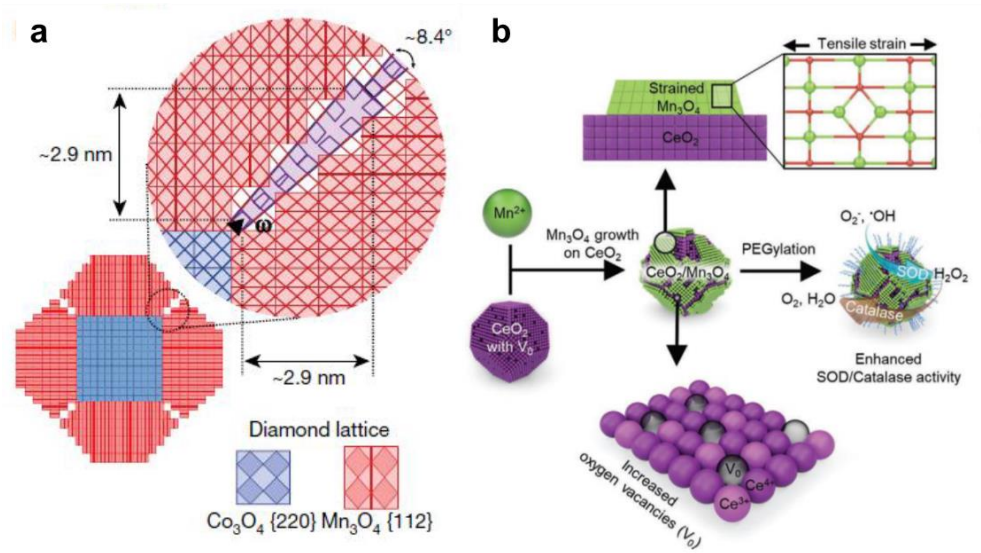

Figure 1.7 Synthesis of heterostructured oxide nanocrystals with epitaxial growth. (a) Synthesis of Co_3O_4/Mn_3O_4 heterostructure. Co_3O_4 and Mn_3O_4 are epitaxially combined with misfits at corner grain boundaries. (from ref. [33] Oh, M. H.; Cho, M. G.; Chung, D. Y.; Inchul Park, I.; Kwon, Y. P.; Ophus, C.; Dokyoon Kim, D.; Kim, M. G.; Jeong, B.; Gu, X. W.; Jo, J.; J. M.; Hong, J.; Sara McMains, S.; Kang, K.; Yung-Eun Sung, Y.-E.; Alivisatos, A. P.; Hyeon, T. *Nature* **2020**, *577*, 359.) (b) Synthesis of CeO_2/Mn_3O_4 heterostructure. Mn_3O_4 at the surface is epitaxially grown enduring high strain. (from ref. [34] Han, S. I.; Lee, S.-W Cho, M. G.; Yoo, J. M.; Oh, M. H.; Jeong, B.; Kim, D.; Park, O. K.; Kim, J.; Namkoong, E.; Jo, J.; Lee, N.; Lim, C.; Soh, M.; Sung, Y.-E.; Yoo, J.; Park, K.; Hyeon, T. *Adv. Mater.* **2020**, *32*, 2001566.)

1.3. Application of heterostructured oxide nanocrystals for catalytic applications.

The controllable structure, composition, valence, and morphology of HONs have made them suitable as catalysts in various reactions by fine control of their interface and surface structure. Electrocatalytic reactions (oxygen reduction reaction (ORR), oxygen evolution reaction (OER), hydrogen evolution reaction (HER), methanol oxidation reaction, and electrocatalytic CO_2 reduction), industrial gas-phase reactions (NO_x reduction, CO oxidation, CO_2 reduction, dry reforming, and steam reforming), organic reactions (C-C coupling, and alcohol oxidation), and photocatalytic reactions are facilitated by catalysts using HONs.[40-42]

1.3.1. electrocatalytic reactions

Among many reactions, electrocatalytic ORR and OER with spinel oxide catalysts are captivating research topics. They act as the key steps in the energy conversion process such as fuel cells, metal−air batteries, and water splitting, but the high expense of platinum group metal (PGM) catalyst hinders its industrialization. Earth-abundant oxide nanomaterials can be good candidates to substitute PGM catalyst but oxide itself has limited activity due to its low conductivity and weaker interaction with substrate molecules. Therefore, enhancement in catalytic activity and conductivity

should be achieved through material engineering including synthesis of alloy or heterostructured nanomaterials that have active microstructure at the interface. In ORR, spinel oxide materials, especially Co-Mn based oxide materials are known as efficient catalysts in alkaline conditions. Their composition, phase, electronic structure, and coordination are studied to find the best Co-Mn catalyst for ORR. In these catalysts, Mn in the octahedral site acts as a main active site due to its optimal orbital overlap with oxygen *p* orbitals during the reaction (Fig. 1.8a).[43] The electronic structure can be modified by introducing Co in the unit cell because electron transfer between Co and Mn makes octahedral Mn cation have optimum e_g occupancy for the ORR. The phase of Co-Mn spinel oxide also affects the overall ORR activity by exposing different atomic structures on the surface (Fig. 1.8b).[44,45] When the nanocrystals have a cubic phase, their activity is higher than the tetragonal phase. Heterostructures combining Co_3O_4 and Mn_3O_4 in one nanocrystal show high activity toward alkaline ORR. Whether the Co_3O_4 or Mn_3O_4 is on the surface affects the catalytic activity because of the different roles of Co and Mn for ORR (Fig. 1.8c).[46,47] The Mn acts as the main active site for ORR reaction, but Co can co-catalyze the ORR reaction by activating H_2O molecules during the reaction. Therefore, exposing both Co and Mn at the surface helps to maximize catalytic activity. Controlling the ratio between the Mn/Co is also crucial for the ORR activity of Co-Mn based HONs because the electronic structure of the active site at the surface can be tuned.

HONs are also scrutinized as active OER catalysts in alkaline conditions. In the OER condition, electrochemically motivated surface reconstruction alters surface structures of the oxide nanomaterials under anodic potential, resulting in the activated or deactivated catalyst for the reaction. Various oxide including spinel oxides, perovskite oxides, rock salt oxides, and some other oxides undergoes surface reconstruction, so controlling the surface structure of HONs are important for developing an active OER catalyst.[48-49] FeOOH/CeO_2 nanotube structure was synthesized on nickel foam with electrodeposition and showed high activity and excellent stability toward OER due to the strong electronic interaction between the CeO_2 and FeOOH. Active FeOOH is replenished by the underneath CeO_2 and the electronic interaction enhanced the OER activity (Fig. 1.9a).[50]

Spinel-type oxides are the most intensively studied oxide material for OER catalysts.[51-53] In alkaline media, earth-abundant spinel oxides have good stability and high activity toward OER comparable to state-of-art noble metal catalysts (e. g. IrO_2 and RuO_2). The cations in octahedral sites are known as active sites for the reaction, so their e_g electrons should be optimized to synthesize active OER catalyst (Fig. 1.9b).[54] The surface reconstruction of Co/Fe/Ni-based spinel oxide generates active oxyhydroxide during the reaction, which further increases the activity (Fig. 1.9c,d).[55-57] During the reconstruction, cations in tetrahedral sites are oxidized to 3+ cations to form active oxyhydroxide at the surface. Heterostructures can further enhance the activity of spinel oxide as OER

catalysts. Hu et. al. reported highly active core–shell Mn_3O_4@$Mn_xCo_{3-x}O_4$ nanostructures with abundant edge sites via a template-mediated synthesis for OER (Fig. 1.10a).[58] By constructing heterostructure, the edge sites of $Co_xMn_{3-x}O_4$ shells where OH^- can intensively bind by forming unsaturated coordination are generated. The heterostructure of Co_3O_4 and CeO_2 nanocomposites are also reported as active OER even in acidic conditions (Fig. 1.10b).[59,60] CeO_2 grains attached to Co_3O_4 can modify the redox properties of Co_3O_4 and enhances its intrinsic OER activity. Because CeO_2 changes the local binding environment of Co_3O_4 nanocrystals, Co^{3+} can be easily oxidized to Co^{4+} species, which is catalytically more active, without the surface reconstruction process. The abundance of Ce^{3+} at the CeO_2 layer is strong evidence for the electron transfer from Co_3O_4 to CeO_2. The heterostructures of oxides and metals are also found to be highly active for OER catalysts. Ag/Co3O4[61], NiCo/NiCoO2[62], and Pt/LiCoO2 [63] are reported as highly active OER catalysts due to the interfacial effect of HONs.

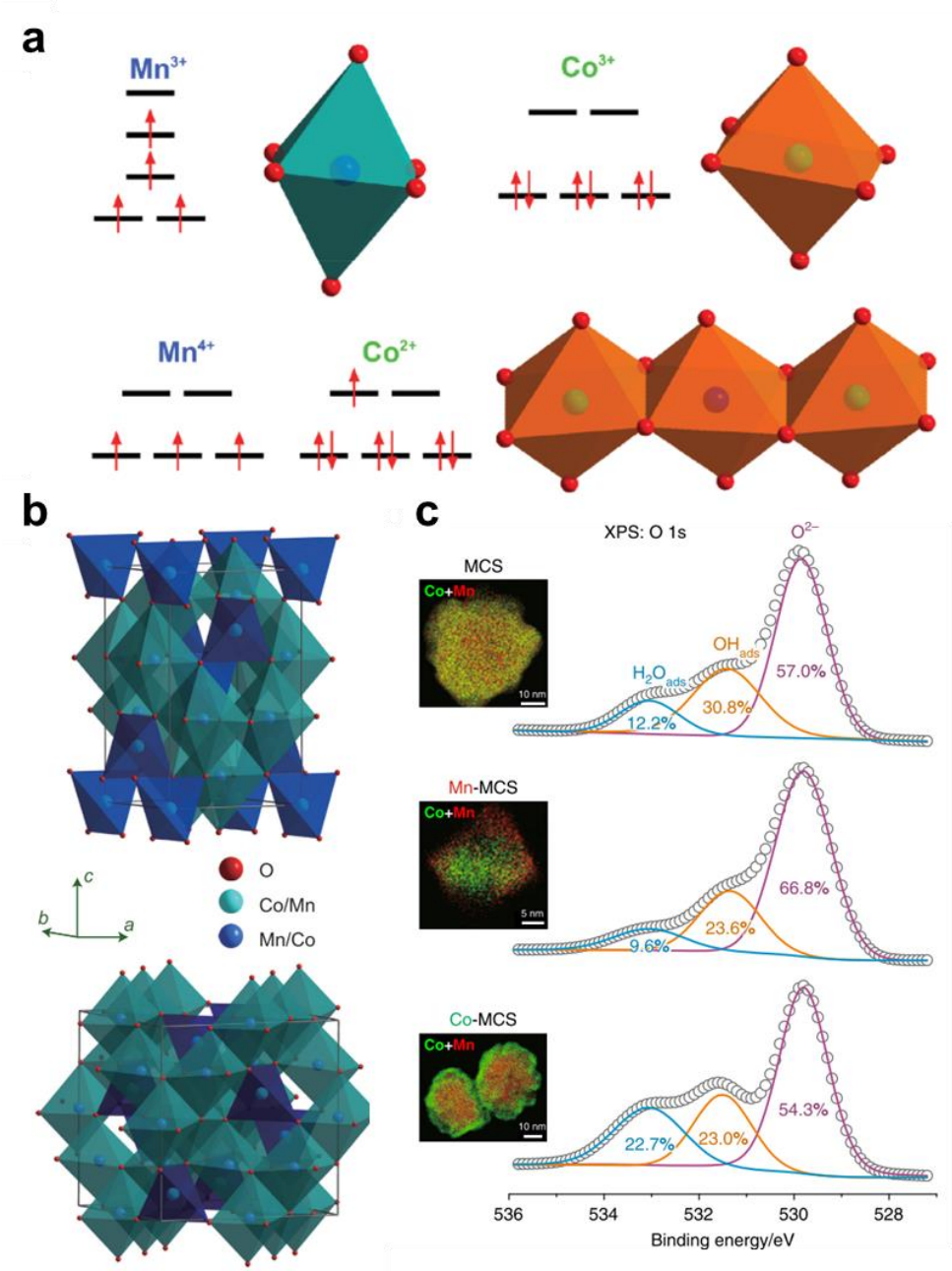

Figure 1.8 Oxygen reduction reaction with Co_3O_4/Mn_3O_4 based nanomaterials. (a) Electron transfer from Mn to Co between octahedral sites. Optimum occupation of e_g orbitals is achieved for the best activity. (from ref. [43] Zhou, Y.; Sun, S.; Xi, S.; Duan, Y.; Sritharan, T.; Du, Y.; Xu, Z. J. *Adv.*

Mater. **2018**, *30*, 1705407.) (b) The phase-dependent activity of Co_3O_4/Mn_3O_4 nanomaterials. Cubic spinel oxides have higher activity than tetragonal ones. (from ref. [44] Cheng, F.; Shen, J.; Peng, B.; Pan, Y.; Tao, Z.; Chen, J. *Nat. Chem.* **2011**, *3*, 79.) (c) Core-shell type Co_3O_4/Mn_3O_4 nanomaterials for the oxygen reduction reaction. Because Co act as cocatalyst, both Mn and Co should be exposed. (from ref. [47] Wang, Y.; Yang, Y.; Jia, S.; Wang, X.; Lyu, K.; Peng, Y.; Zheng, H.; Wei, X.; Ren, H.; Xiao, L.; Wang, J.; Muller, D. A. Abruña, H. D.; Hwang, B. J.; Lu, J.; Zhuang, L *Nat. Commun.* **2019**, *10*, 1-8.)

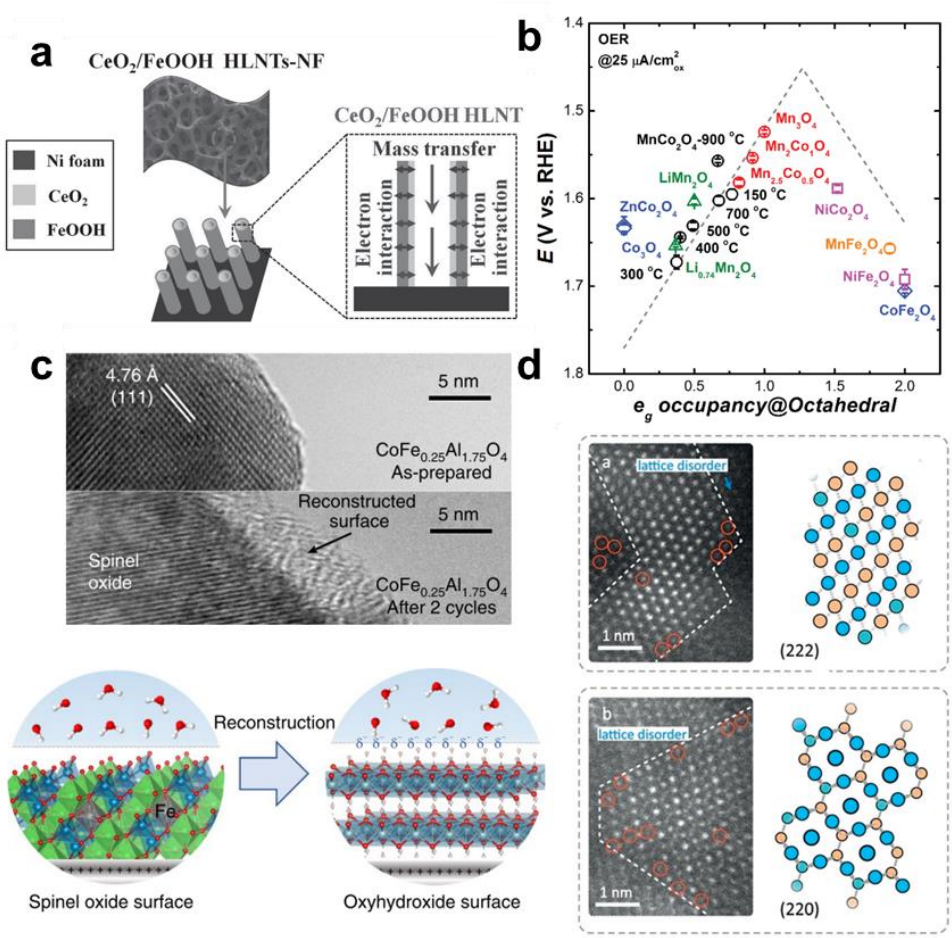

Figure 1.9 Oxygen evolution reaction at the oxide nanomaterials. (a) CeO_2/FeOOH heterostructure for efficient OER catalyst. (from ref. [50] Feng, J.-X.; Ye, S.-H.; Xu, H.; Tong, Y-X.; Li, G.-R. *Adv. Mater.* **2016**, *28*, 4698.) (b) Spinel oxide catalysts for OER. Their e_g occupancy shows a volcano-like plot toward OER activity. (from ref. [54] Wei, C.; Feng, Z.; Scherer, G. G.; Barber, J.; Shao-Horn, Y.; Xu, Z. J. *Adv. Mater.* **2017**, *29*, 1606800.) (c) Surface reconstruction of spinel $CoFe_xAl_{2-x}O_4$ catalyst during OER. The formation of the active oxyhydroxide layer is facilitated by Fe addition. (from ref. [55] Wu, T.; Sun, S.; Song, J.; Xi, S.; Du, Y.; Chen, B.;

Sasangka, W. A.; Liao, H.; Gan, C. L.; Scherer, G. G.; Zeng, L.; Wang, H.; Li, H.; Grimaud, A.; Xu, Z. J. *Nat. Catal.* **2019**, *2*, 763.) (d) Direct electron microscopic observation of surface reconstruction of spinel oxide during OER. (from ref. [57] Wang, X.-T.; Ouyang, T.; Wang, L.; Zhong, J.-H.; Liu, Z.-Q. *Angew. Chem. Int. Ed*, **2020**, *132*, 6554.)

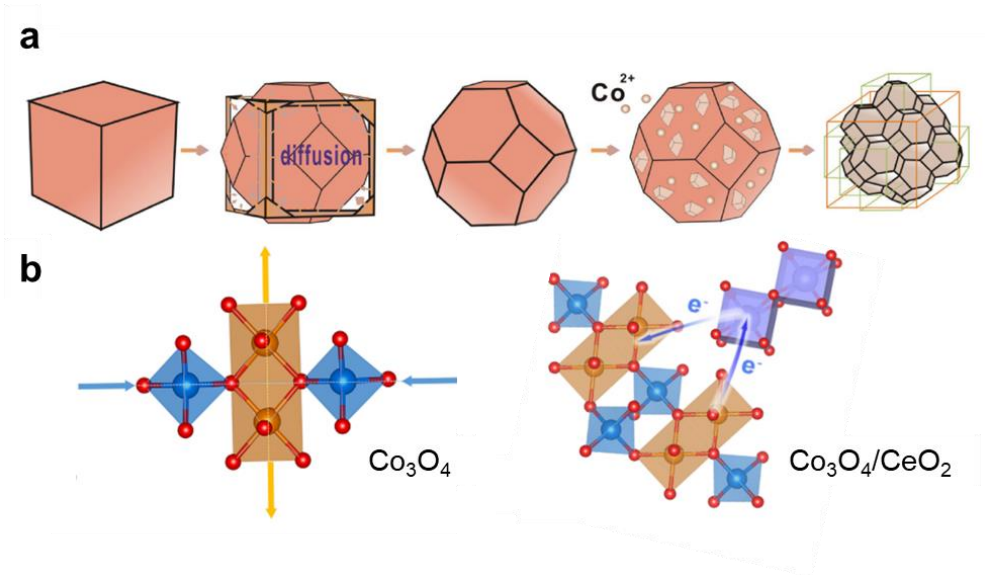

Figure 1.10 Oxygen evolution reaction with heterostructured oxide nanomaterials. (a) OER catalyst composed of $Co_3O_4/Mn_xCo_{3-x}O_4$ core-shell nanocrystal. (from ref. [58] Hu, C.; Zhang, L.; Zhao, Z. J.; Luo, J.; Shi, J.; Huang, Z.; Gong, J. *Adv. Mater.* **2017**, *29*, 1701820.) (b) Active OER catalyst using charge transfer between Co_3O_4 and CeO_2 at the Co_3O_4/CeO_2 heterostructures. (from ref. [59] Huang, J.; Sheng, H.; Ross, R. D.; Han, J.; Wang, X.; Song, B.; Jin, S. *Nat. Commun.* **2021**, *12*, 1-8.)

1.3.2. industrial gas phase reactions

Oxide materials are known as good support materials for various gas-phase reactions, where PGM metals act as active catalysts. The charge transfer through the interface, modification of oxide structure at the interfacial perimeter, stability enhancement, and strong metal-support interaction occurs at the interface of metal and oxide during the reactions (Fig. 1.11).[64] To utilize these interfacial effect for the development of active catalysts, several metal-oxide composites were exploited for various gas-phase reactions.[65,66] However, due to the high expense of PGM metals, the oxide materials were used as active catalysts for CO oxidation, methane combustion, and CO_2 hydrogenation. Spinel oxide, especially Co_3O_4 and Mn_3O_4 are reported as active catalysts that can substitute conventional platinum catalysts for CO oxidation (Fig. 1.12a).[67] CeO_2, SiO_2, and TiO_2 were introduced to the spinel oxide system as support material to increase the activity of the catalysts. HONs combining spinel oxides and support oxides (e. g. Co_3O_4/CeO_2[68-70], Mn_3O_4/SiO_2[37], Mn_3O_4/CeO_2, Co_3O_4/TiO_2, and $Co_3O_4/CeO_2/TiO_2$) exhibited high activity toward CO oxidation, which is comparable to noble-metal-based catalysts (Fig. 1.12b-d). The charge transfer at the interface of support and spinel oxides affects the catalytic activity of spinel oxides. For instance, in Co_3O_4/CeO_2 system, the high oxygen storage capacity of CeO_2 improves the oxidation ability of Co_3O_4 nanocrystals by replenishing oxygens that participate in the CO oxidation

reaction. The maximization of the interface between Co_3O_4/CeO_2 with a high surface area gave good activity toward CO oxidation. HONs also can catalyze various reactions including water gas shift reaction[71], methanol synthesis from CO_2[72], methane conversion[73], formaldehyde oxidation[74], and soot oxidation.[75]

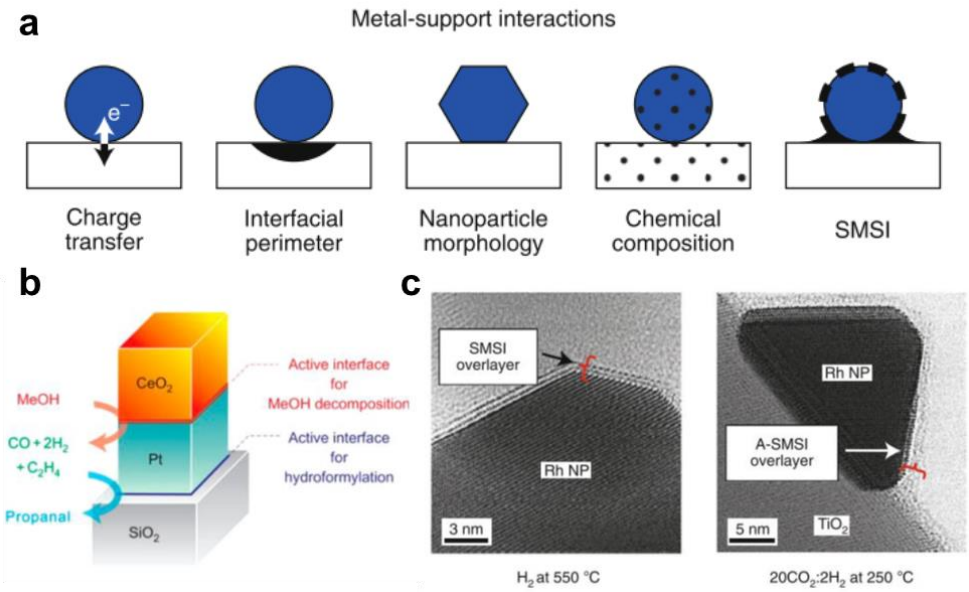

Figure 1.11 Effect of interface structure on catalysis. (a) Various interfacial interactions between metal catalysts and oxide supports. (from ref. [64] van Deelen, T. W.; Mejía, C. H.; de Jong, K. P. *Nat. Catal.* **2019**, *2*, 955.) (b) Dual interface formation for tandem reaction. (from ref. [65] Yamada, Y.; Tsung, C. K.; Huang, W.; Huo, Z.; Habas, S. E.; Soejima, T.; Aliaga, C. E.; Somorjai, G. A.; Yang, P. *Nat. Chem.* **2011**, *3*, 372.) (c) Adsorbate-mediated strong metal-support interaction between Rh nanoparticle and TiO_2 support. (from ref. [66] Matsubu, J. C.; Zhang, S.; Derita, L.; Marinkovic, N. S.; Chen, J. G.; Graham, G. W.; Pan, X.; Christopher, P. *Nat. Chem.* **2017**, *9*, 120.)

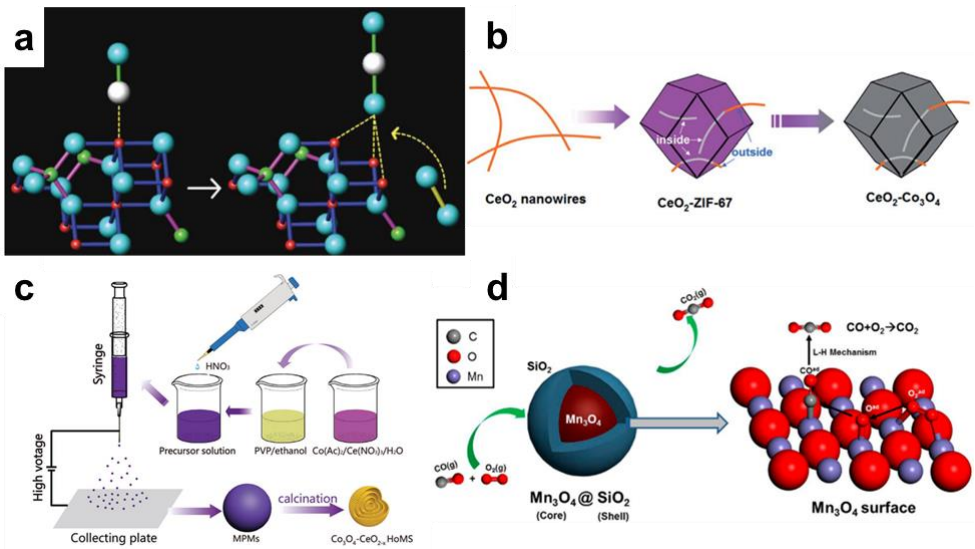

Figure 1.12 Heterostructured oxide nanocrystals for CO oxidation. (a) Co_3O_4 (110) facet is an active site for catalytic CO oxidation reaction. (from ref. [67] Xie, X.; Li, Y.; Liu, Z.-Q.; Haruta, M.; Shen, W. *Nature* **2009**, *458*, 746.) (b) MOF- driven Co_3O_4/CeO_2 nanocomposite for CO oxidation. (from ref. [68] Gu, L.; Ma, X.; Yu, R.; Zhang, Q.; Song, S.; Wang, H.; Wang, D.; Qi, J.; Mao, D. *Adv. Funct. Mater.* **2019**, 1806588.) (c) Co_3O_4/ CeO_2 hollow mesosphere structure for CO oxidation (from ref. [69] Feng, J.; Zhang, H.; Wang, X.; Wang, Z.; Song, S.; Zhao, S.; Zhang, Y. *Chem. Sci.* **2016**, *7*,1109.) (d) Mn_3O_4/SiO_2 core-shell nanoparticles for CO oxidation. (from ref. [37] Xu, J.; Deng, Y.-Q. Zhang, X.-M.; Luo, Y.; Mao, W.; Yang, X.-J. Ouyang, L.; Tian, P.; Han, Y.-F. *ACS Catal.* **2014**, *4*, 4106.)

1.3.3 photocatalytic reactions

Photocatalytic reactions suggest promising solutions for future energy conversion and storage. HONs can be used as catalysts for photocatalytic reactions. For instance, light-driven oxidation of water has been studied for the development of the solar water splitting process. In those catalysts, oxide materials (e. g. TiO_2, $BiVO_4$, ZnO, In_2O_3, and CeO_2) which have large band-gap energy that can absorb light are used as photocatalysts (Fig. 1.13a).[76-78] Electrons are excited to the conduction band by absorbing light which has higher energy than the direct wide band-gap energy of the semiconductor oxide nanomaterials and the excited electrons catalyze the reactions. When active oxides for the reaction are conjugated to semiconductor oxide nanomaterials, the electrons generated from the light-driven excitation move to the active oxides, and the electrons participate in the reaction at the surface of the active oxides. Liu et. al. reported water oxidation on TiO_2/Cu_2O core/ultra-thin shell nanorods (Fig. 1.13b).[79] The strong interaction between TiO_2 and Cu_2O during the reaction makes the HON highly active by the redox reaction between in situ generated Ti^{3+} and Cu^{2+}. The valence band and conduction band of the Cu_2O respectively get the holes in the valence band and the excited electrons in the conduction band of TiO_2 because TiO_2 and Cu_2O respectively act as the photosensitizer and cocatalyst. The band structure of HON catalysts can be adjusted by making heterojunction between two semiconductor oxide nanomaterials.[80]

The use of bare TiO_2 results in a large bandgap which limits the absorption of whole solar energy and severe recombination of photoinduced charges. Forming heterojunction with In_2O_3 solved these problems in the Pt@TiO_2@In_2O_3@MnO_x mesoporous hollow nanosphere system (Fig. 1.13c).[81] The separated charges move in the opposite directions to respectively catalyze oxidation and reduction reactions at the opposite surfaces. The Heterostructure guarantees efficient charge separation and light absorption for photocatalysts.

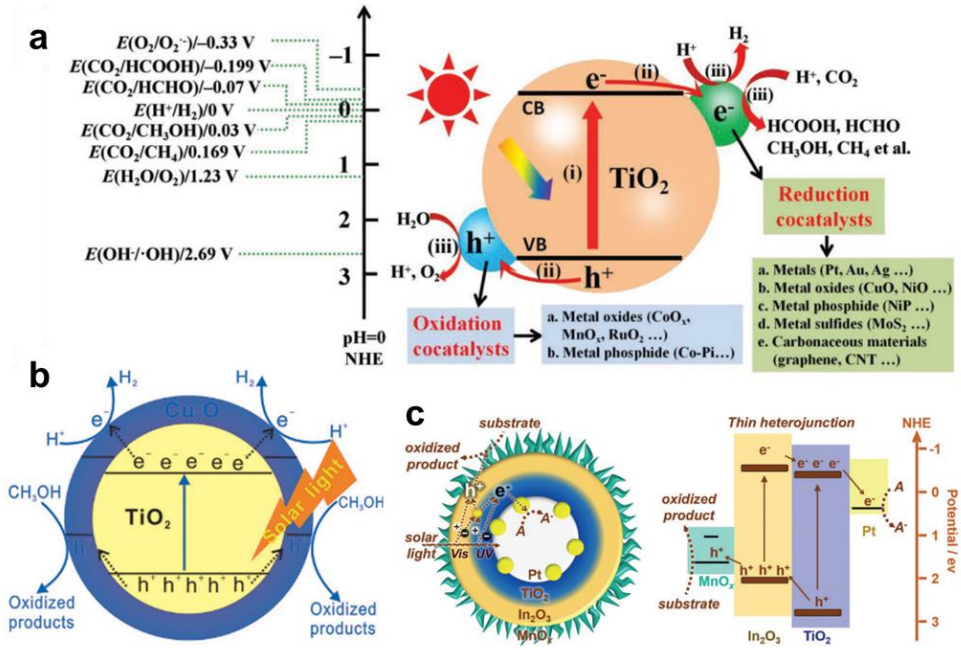

Figure 1.13 Heterostructured oxide nanomaterials for photocatalytic reactions. (a) TiO_2 based heterostructured materials for photocatalytic reactions. TiO_2 absorbs light and generates photoinduced charges. (from ref. [78] Meng, A.; Zhang, L.; Cheng, B.; Yu, J. *Adv. Mater.* **2019**, *31*, 1807660.) (b) TiO_2/Cu_2O core-shell nanoparticles for efficient solar-driven oxidation reactions. (from ref. [79] Liu, Y.; Zhang, B.; Luo, L.; Chen, X.; Wang, Z.; Wu, E.; Su, D.; Huang, W, *Angew. Chem. Int. Ed.* **2015**, *54*,15260.) (c) $Pt/TiO_2/In_2O_3/MnO_2$ heterostructures for dual photocatalyst. (from ref. [81] Li, A.; Chang, X.; Huang, Z.; Li, C.; Wei, Y.; Zhang, L.; Wang, T.; Gong, J. *Angew. Chem. Int. Ed.* **2016**, *55*, 13734.)

1.4. Dissertation overview

Earth-abundant oxides have been regarded as good substituents for expensive noble metals for various catalytic reactions, but their intrinsic activities are relatively low. To improve their properties, heterogeneous oxide nanocrystals which can be generated by merging several oxides in one domain have been synthesized through heterogeneous nucleation during the colloidal synthesis process. The interfacial structure formed in the heterogeneous oxide nanocrystals affects the catalytic activity of various reactions including electrocatalytic reactions, industrial gas-phase reactions, organic reactions, and photocatalytic reactions. This dissertation demonstrates the synthesis of heterostructured oxide nanocrystals for the study of the catalytic mechanisms of CO oxidation and electrocatalytic oxygen reduction reaction using interface-controlled Co_3O_4/CeO_2 and facet-defined $Co_3O_4/Co_yMn_{1-y}O_x$ respectively.

Firstly, to investigate the role of the interface in the activity of catalytic oxidation, a controlled CeO_2 layer is deposited on Co_3O_4, Mn_3O_4, and Fe_3O_4 nanocubes (NCs). Strikingly, Co_3O_4 NCs with CeO_2 layers presented a 12-times higher CO oxidation activity than the pure Co_3O_4 NCs. From various in situ characterization, the role of the deposited CeO_2 to prevent the reduction of Co_3O_4 by supplying oxygen is revealed. Because of the versatile change in the oxidation state from the maximized interface formation, the highest CO oxidation rate is achieved even under O_2-

deficient conditions when three facets of Co_3O_4 nanocubes are covered by CeO_2 layers. By analyzing the oxide-oxide interface, the Mars−van Krevelen mechanism which explains oxidation reaction on the oxide surface is proven with Co_3O_4−CeO_2 interfaces. By comparing the activity trend and hot electron flow which are observed for H_2 oxidation reactions using catalytic nanodiodes, charge transfer at the interface is revealed as the origin of the activity enhancement.

Secondly, facet-defined Co−Mn spinel oxide surfaces enclosed by (001) are generated on Co_3O_4 nanocube templates using epitaxial growth with different atomic compositions. To minimize the strain effect on catalytic activity, composition gradient synthesis is introduced to relieve the surface strain layer by layer. On these synthesized nanocrystals, both experimental and calculational oxygen reduction reaction (ORR) activity showed a volcano-like trend according to the Mn/Co ratios because of an optimized charge transfer from octahedral-Mn to adjacent Co. The best catalyst, which has a 1:1 ratio of Mn/Co, shows both excellent ORR activity (0.894 V vs RHE in 1 M KOH) and stability (2% activity loss against chronoamperometry). By fixing the facet- and strain-related factors, a well-defined platform for exploring composition−structure−activity relationships in electrocatalytic processes is established.

1.5. Reference

[1] Yin, Y.; Alivisatos, A. P. *Nautre* **2005**, *437*, 664.

[2] Ning, C.-Z.; Dou, L.; Yang, P. *Nat. Rev. Mater.* **2017**, *2*, 1.

[3] Zhang, L.; Xie, Z.; Gong, J. *Chem. Soc. Rev.* **2016**, *45*, 3916.

[4] Lignier, P.; Bellabarba, R.; Tooze, R. P. *Chem. Soc. Rev.* **2012**, *41*, 1708.

[5] Peng, L.; Dutta, S. K.; Mondal, D.; Hudait, B.; Shyamal, S.; Xie, R.; Mahadevan, P.; Pradhan, N.; *J. Am. Chem. Soc.* **2019**, *141*, 16160.

[6] Trizio, L. D.; Manna, L. *Chem. Rev.* **2016**, *116*, 10852.

[7] Carenco, S.; Portehault, D.; Boissière, C.; Mézailles, N.; Sanchez, C. *Chem. Rev.* **2013**, *113*, 7981.

[8] Voiry, D.; Yang, J.; Kupferberg, J.; Fullon, R.; Lee, C.; Jeong, H. Y.; Shin, H. S.; Chhowalla, M. *Science* **2016**, *353*, 1430.

[9] Ma, C.; Wang, Z. L. *Adv. Mater.* **2005**, *17*, 2635.

[10] Chang, H.-Y.; Chen, H.-I. *J. Cryst. Growth* **2005**, *283*, 457.

[11] Park, J.; An, K.; Hwang, Y.; Park, J.-G.; Noh, H.-J.; Kim, J.-Y.; Park, J.-H.; Hwang, N.-M.; Hyeon, T. *Nat. Mater.* **2004**, *3*, 891.

[12] Hua, A.; Cao, T.; Gu, X.-K.; Lu, J.; Jiang, Z.; Pan, X.; Luo, L.; Li, W.-X.; Huang, W. *Angew. Chem. Int. Ed.* **2014**, *53*, 4856.

[13] Sathya, A.; Guardia, P.; Brescia, R.; Silvestri, N.; Pugliese, G.; Nitti, S.; Manna, L.; Pellegrino, T. *Chem. Mater.* **2016**, *28*, 1769.

[14] Sarkar, A.; Wang, Q.; Schiele, A.; Chellali, M. R.; Bhattacharya, S. S.; Wang, D.; Brezesinski, T.; Hahn,H.; Velasco, L.; Breitung, B. *Adv. Mater.*

2019, *31*, 1806236.

[15] Bi, Y.; Tao, J.; Wu, Y.; Li, L.; Xu, Y.; Hu, E.; Wu, B.; Hu, J.; Wang, C.; Zhang, J.-G.; Qi, Y.; Xiao, J. *Science* **2020**, *370*, 1313.

[16] Chakhalian, J.; Millis, A. J.; Rondinelli J. *Nat. Mater.* **2012**, *11*, 92.

[17] Ghosh, R.; Paria, C. S. *Chem. Rev.* **2012**, *112*, 2373.

[18] Vila, E.; Rojas, R. M.; Martin de Vidales, J. L.; Garcia-Martinez, O. *Chem. Mater.* **1996**, *8*, 1078.

[19] Pan, H.; Shao, Y.; Yan, P.; Cheng, Y.; Han, K. S.; Nie, Z.; Wang, C.; Yang, J.; Li, X.; Bhattacharya, P.; Mueller, K. T.; Liu J. *Nat. Energy* **2016**, *1*, 16039.

[20] Soh, M.; Kang, D.-W.; Jeong, H.-G.; Kim, D.; Kim, D. Y.; Yang, W.; Song, C.; Baik, S.; Choi, I.-Y.; Ki, S. K.; Kwon, H. J.; Kim, T.; Kim, C. K.; Lee, S.-H.; Hyeon, T. *Angew. Chem. Int. Ed.* **2017**, *56*,11399.

[21] Chen, H.; Jie, K.; Jafta C. J.; Yang, Z.; Yao, S.; Liu, M.; Zhang, Z.; Liu, J.; Chi, M.; Fu J.; Dai, S. *Appl. Catal. B* **2020**, *276*, 119155.

[22] Zhao, J.; Chen, B.; Wang, F. *Adv. Mater.* **2020**, *32*, 2004142.

[23] Gawande, M. B.; Goswami, A.; Asefa, T.; Guo, H.; Biradar, A. V.; Peng, D.-L.; Zboril, R. Varma, R. S. *Chem. Soc. Rev.* **2015**, *44*, 7540.

[24] Kwon, H. J.; Shin, K.; Soh, M.; Chang, H.; Kim, J.; Lee, J.; Ko, G.; Kim, B. H.; Kim, D.; Hyeon, T. *Adv. Mater.* **2018**, *30*, 1704290.

[25] Pang, X.; Zhao, L.; Han, W.; Xin, X.; Lin, Z. *Nat. Nanotech.* **2013**, *8*, 426.

[26] Kovalenko, M. V.; Scheele, M.; Talapin, D. V. *Science*, **2009**, *324*, 1417.

[27] Cooper, S. R.; Candler, R. O.; Cosby, A. G.; Johnson, D. W.; Jensen, K. M. Ø.; Hutchison, J. E. *ACS Nano* **2020**, *14*, 5480.

[28] Loiudice, A.; Strach, M.; Saris, S.; Chernyshov, D.; Buonsanti, R. *J. Am. Chem. Soc.* **2019**, *141*, 8254.

[29] Song, Q.; Zhang, Z. J. *J. Am. Chem. Soc.* **2012**, *134*, 10182.

[30] Chai, Y.; Feng Feng, F.; Li, Q.; Yu, C.; Feng, X.; Lu, P.; Yu, X.; Ge, M.; Wang, X.; Yao, L. *J. Am. Chem. Soc.* **2019**, *141*, 3366.

[31] Jansons, A. W.; Hutchison, J. E. *ACS Nano* **2016**, *10*, 6942.

[32] Lee, J.; Yang, J.; Kwon, S. G.; Hyeon, T. *Nat. Rev. Mater.* **2016**, *1*, 1-16.

[33] Oh, M. H.; Cho, M. G.; Chung, D. Y.; Inchul Park, I.; Kwon, Y. P.; Ophus, C.; Dokyoon Kim, D.; Kim, M. G.; Jeong, B.; Gu, X. W.; Jo, J.; J. M.; Hong, J.; Sara McMains, S.; Kang, K.; Yung-Eun Sung, Y.-E.; Alivisatos, A. P.; Hyeon, T. *Nature* **2020**, *577*, 359.

[34] Han, S. I.; Lee, S.-W Cho, M. G.; Yoo, J. M.; Oh, M. H.; Jeong, B.; Kim, D.; Park, O. K.; Kim, J.; Namkoong, E.; Jo, J.; Lee, N.; Lim, C.; Soh, M.; Sung, Y.-E.; Yoo, J.; Park, K.; Hyeon, T. *Adv. Mater.* **2020**, *32*, 2001566.

[35] Ding, H. L.; Zhang, Y. X.; Wang, S.; Xu, J. M.; Xu, S. C.; Li, G. H. *Chem. Mater.* **2012**, *24*, 4572.

[36] Li, X.; Zhou, L.; Wei, Y.; El-Toni, A. M.; Zhang, F.; Zhao, D. *J. Am. Chem. Soc.* **2014**, *136*, 15086.

[37] Xu, J.; Deng, Y.-Q. Zhang, X.-M.; Luo, Y.; Mao, W.; Yang, X.-J. Ouyang, L.; Tian, P.; Han, Y.-F. *ACS Catal.* **2014**, *4*, 4106.

[38] Wang, W.; Jiao, T.; Zhang, Q.; Luo, X.; Hu, J.; Chen.Y.; Peng, Q.; Yanc

X.; Li, B. *RSC Adv.* **2015**, *5*, 56279.

[39] Xia, X.; Tu, J.; Zhang, Y.; Wang,X.; Gu, C.; Zhao, X.-b.; Fan, H. J.; *ACS Nano* **2012**, *6*, 5531.

[40] Peng, S.; Gong, F.; Li, L.; Yu, D.; Ji, D.; Zhang, T.; Hu, Z.; Zhang, Z.; Chou, S.; Du, Y.; Ramakrishna, S. *J. Am. Chem. Soc.* **2018**, *140*, 13644.

[41] Montini, T.; Melchionna, M.; Monai, M.; Fornasiero, P. *Chem. Rev.* **2016**, *116*, 5987.

[42] Chen, X.; Mao S. S. *Chem. Rev.* **2007**, *107*, 2891.

[43] Zhou, Y.; Sun, S.; Xi, S.; Duan, Y.; Sritharan, T.; Du, Y.; Xu, Z. J. *Adv. Mater.* **2018**, *30*, 1705407.

[44] Cheng, F.; Shen, J.; Peng, B.; Pan, Y.; Tao, Z.; Chen, J. *Nat. Chem.* **2011**, *3*, 79.

[45] Li, C.; Han, X.; Cheng, F.; Hu, Y.; Chen, C.; Chen, J. *Nat. Commun.* **2015**, *6*, 1-8.

[46] Yanga, Y.; Xionga, Y.; Holtz, M. E.; Feng, X.; Zeng, R.; Chen, G.; DiSalvo, F. J.; Muller, D. A.; Abruña, H. D. *Proc. Natl. Acad. Sci. U.S.A.* **2019**, *116*, 24425.

[47] Wang, Y.; Yang, Y.; Jia, S.; Wang, X.; Lyu, K.; Peng, Y.; Zheng, H.; Wei, X.; Ren, H.; Xiao, L.; Wang, J.; Muller, D. A. Abruña, H. D.; Hwang, B. J.; Lu, J.; Zhuang, L *Nat. Commun.* **2019**, *10*, 1-8.

[48] Zhang, W.; Wang, F.; McCann, S. D.; Wang, D.; Chen, P.; Stah, S. S.; Liu, G.; *Science* **2016**, *353*, 1014.

[49] Wang, J.; Kim, S.-J.; Liu, J.; Gao, Y.; Choi, S.; Han, J.; Shin, H.; Jo, S.;

Kim, J.; Ciucci, F.; Kim, H.; Li, Q.; Yang, W.; Long, X.; Yang, S.; Cho, S.-P.; Chae, K. H.; Kim, M. G.; Kim, H.; Lim, J. *Nat. Catal.* **2021**, *4*, 212.

[50] Feng, J.-X.; Ye, S.-H.; Xu, H.; Tong, Y-X.; Li, G.-R. *Adv. Mater.* **2016**, *28*, 4698.

[51] Li, H.; Sun, S.; Xi, S.; Chen, Y.; Wang, T.; Du, Y.; Sherburne, M.; Ager, J. W.; Fisher, A. C.; Xu, Z. J.; *Chem. Mater.* **2018**, *30*, 6839.

[52] Sun, S.; Sun, Y.; Zhou, Y.; Xi, S.; Ren, X.; Huang, B.; Liao, H.; Wang, L. P.; Du, Y.; Xu, Z. J. *Angew. Chem. Int. Ed.* **2019**, *131*,6103.

[53] Lu, X.; Li, M.; Peng, Y.; Xi, X.; Li, M.; Chen, Q.; Dong, A. *J. Am. Chem. Soc.* **2021**, *143*, 16925.

[54] Wei, C.; Feng, Z.; Scherer, G. G.; Barber, J.; Shao-Horn, Y.; Xu, Z. J. *Adv. Mater.* **2017**, *29*, 1606800.

[55] Wu, T.; Sun, S.; Song, J.; Xi, S.; Du, Y.; Chen, B.; Sasangka, W. A.; Liao, H.; Gan, C. L.; Scherer, G. G.; Zeng, L.; Wang, H.; Li, H.; Grimaud, A.; Xu, Z. J. *Nat. Catal.* **2019**, *2*, 763.

[56] Bergmann, A.; Jones, T. E.; Martinez Moreno, E.; Teschner, D.; Chernev, P.; Gliech, M.; Reier, T.; Dau, H.; Strasser, P. *Nat. Catal.* **2018**, *1*, 711.

[57] Wang, X.-T.; Ouyang, T.; Wang, L.; Zhong, J.-H.; Liu, Z.-Q. *Angew. Chem. Int. Ed*, **2020**, *132*, 6554.

[58] Hu, C.; Zhang, L.; Zhao, Z. J.; Luo, J.; Shi, J.; Huang, Z.; Gong, J. *Adv. Mater.* **2017**, *29*, 1701820.

[59] Huang, J.; Sheng, H.; Ross, R. D.; Han, J.; Wang, X.; Song, B.; Jin, S.

Nat. Commun. **2021**, *12*, 1-8.

[60] Liu, Y.; Ma, C.; Zhang, Q.; Wang, W.; Pan, P.; Gu, L.; Xu, D.; Bao, J.; Dai, Z. *Adv. Mater.* **2019**, *31*, 1900062.

[61] Yu, M.; Moon, G. h.; Castillo, R. G.; DeBeer, S.; Weidenthaler, C.; Tüysüz, H, *Angew. Chem. Int. Ed.* **2020**, *59*, 16544.

[62] Xu, H.; Shi, Z. X.; Tong, Y. X.; Li, G. R. *Adv. Mater.* **2018**, *30*, 1705442.

[63] Zheng, X.; Cui, P.; Qian, Y.; Zhao, G.; Zheng, X.; Xu, X.; Cheng, Z.; Liu, Y.; Dou, S. X.; Sun, W. *Angew. Chem. Int. Ed.* **2020**, *132*, 14641.

[64] van Deelen, T. W.; Mejía, C. H.; de Jong, K. P. *Nat. Catal.* **2019**, *2*, 955.

[65] Yamada, Y.; Tsung, C. K.; Huang, W.; Huo, Z.; Habas, S. E.; Soejima, T.; Aliaga, C. E.; Somorjai, G. A.; Yang, P. *Nat. Chem.* **2011**, *3*, 372.

[66] Matsubu, J. C.; Zhang, S.; Derita, L.; Marinkovic, N. S.; Chen, J. G.; Graham, G. W.; Pan, X.; Christopher, P. *Nat. Chem.* **2017**, *9*, 120.

[67] Xie, X.; Li, Y,; Liu, Z.-Q.; Haruta, M.; Shen, W. *Nature* **2009**, *458*, 746.

[68] Gu, L.; Ma, X.; Yu, R.; Zhang, Q.; Song, S.; Wang, H.; Wang, D.; Qi, J.; Mao, D. *Adv. Funct. Mater.* **2019**, 1806588.

[69] Feng, J.; Zhang, H.; Wang, X.; Wang, Z.; Song, S.; Zhao, S.; Zhang, Y. *Chem. Sci.* **2016**, *7*,1109.

[70] Tang, C. Wei.; Kuo, M.C.; Lin, C. J.; Wang, C. B.; Chien, S. H. *Catal. Today* **2008**, *131*, 520.

[71] Park, J. B.; Graciani, J.; Evans, J.; Stacchiola, D.; Senanayake, S. D.; Barrio, L.; Liu, P.; Sanz, J. F.; Hrbek, J.; Rodriguez, J. A. *J. Am. Chem. Soc.*

2010, *132*, 356

[72] Gao, P.; Nazeeruddin, M. K.; Saliba, M.; Leijtens, T.; Abate, A.; Snaith, H.; Fung, R. C. M.; Kamat, P. V.; Lyczko, K.; Lundberg, D.; Eriksson, L.; Kowalewska, E.; Lim, J.; Teuscher, J.; Park, T.; Snaith, H. J. *Science* **2014**, *345*, 546.

[73] Zuo, Z.; Ramírez, P. J.; Senanayake, S. D.; Liu, P.; Rodriguez, J. A. *J. Am. Chem. Soc.* **2016**, *138*, 13810.

[74] Quiroz, J.; Giraudon, J. M.; Gervasini, A.; Dujardin, C.; Lancelot, C.; Trentesaux, M.; Lamonier, J. F. *ACS Catal.* **2015**, *5*, 2260.

[75] Zhao, M.; Deng, J.; Liu, J.; Li, Y.; Liu, J.; Duan, Z.; Xiong, J.; Zhao, Z.; Wei, Y.; Song, W.; Sun, Y. *ACS Catal.* **2019**, *9*, 7548.

[76] Mclaren, A.; Valdes-Solis, T.; Li, G.; Tsang, S. C. *J. Am. Chem. Soc.* **2009**, *131*, 12540.

[77] Pan, Y. X.; You, Y.; Xin, S.; Li, Y.; Fu, G.; Cui, Z.; Men, Y. L.; Cao, F. F.; Yu, S. H.; Goodenough, J. B. *J. Am. Chem. Soc.* **2017**, *139*, 4123.

[78] Meng, A.; Zhang, L.; Cheng, B.; Yu, J. *Adv. Mater.* **2019**, *31*, 1807660.

[79] Liu, Y.; Zhang, B.; Luo, L.; Chen, X.; Wang, Z.; Wu, E.; Su, D.; Huang, W, *Angew. Chem. Int. Ed.* **2015**, *54*,15260.

[80] Liu, L.; Ji, Z.; Zou, W.; Gu, X.; Deng, Y.; Gao, F.; Tang, C.; Dong, L. *ACS Catal.* **2013**, *3*, 2052.

[81] Li, A.; Chang, X.; Huang, Z.; Li, C.; Wei, Y.; Zhang, L.; Wang, T.; Gong, J. *Angew. Chem. Int. Ed.* **2016**, *55*, 13734.

Chapter 2. Revealing Charge Transfer at the Interface of Spinel Oxide and Ceria during CO Oxidation

2.1. Introduction

The interfacial effect is an important factor in improving the catalytic performances of heterogeneous catalysts, which usually consist of noble metal nanoparticles (NPs) supported on oxides.[1–4] In particular, charge transfer at the interface of the supported catalysts is significant for understanding the reaction mechanisms.[5–7] When noble metals (Pt, Au, and Pd) are supported on various reducible oxides (TiO_2, CeO_2, NiO, and Co_3O_4), the catalytic activity has been enhanced through charge transfer at the interface.[8–10] Among many oxides, CeO_2, which can reversibly reduce Ce^{4+} ions to Ce^{3+} ions at the interface with metals, is excellent oxide support that shows a high oxygen storage capacity and the facile formation of oxygen vacancies.[11,12] CO oxidation has been intensely studied as a model reaction to scrutinize the interfacial effects.[13,14] CeO_2 plays an essential role in improving the CO oxidation reactivity by delivering oxygen at the interface because CO is more strongly adsorbed to noble metals than O_2, especially under oxygen-deficient conditions.[15,16] However, when a spinel oxide is used as the main active material instead of a noble metal, the

complexity in the electronic structure at the oxide-oxide interface hinders the characterization of the origin for the enhancement in reactivity.

Spinel oxides such as Co_3O_4 and Mn_3O_4 are not only good supports for noble metal catalysts that increase the CO oxidation rate, but also excellent catalysts for CO oxidation even in the absence of noble metals.[17–19] Xie et al. reported that high activities in the low-temperature CO oxidation reaction are achieved on Co_3O_4 nanorods because of the abundant exposure of active Co^{3+} sites on {110} planes.[18] Co_3O_4-catalyzed CO oxidation follows a common Mars–van Krevelen (MvK) mechanism whereby oxygen vacancies are refilled by gaseous oxygen while CO molecules react with the surface lattice oxygen atoms coordinated to the Co^{3+} cations.[20–23] The active oxide species experience dynamic changes in their structures and surface states depending on the temperature and relative ratio of the CO and O_2 gases during CO oxidation. Thus, tracking the change in oxidation state at the catalyst surface or at the metal-oxide interface is important. Lukashuk et al. reported that the reduction temperature of Co_3O_4 in Co_3O_4-CeO_2 catalysts is increased by the attachment of CeO_2.[24] The addition of CeO_2 to Co_3O_4 enhances preferential CO oxidation activity, demonstrating that the interaction of the two metal oxides at the interface preserves the Co_3O_4 oxidation state. However, in many studies, a lack of well-organized interfacial structures regarding the size, shape, and crystallinity of the catalyst makes precise characterization of the interface properties difficult.

In this work, to analyze the interfacial effects in the catalytic oxidation, heterostructured spinel oxide (Co_3O_4, Mn_3O_4, and Fe_3O_4) nanocubes (NCs) coated by controlled CeO_2 layers were designed. A selective deposition protocol to fabricate CeO_2-deposited spinel NCs with 1, 3, and 6 facets of CeO_2 (MCe-1F, MCe-3F, and MCe-6F NCs for spinel oxide) are elaborated. To examine the acquired heterostructured oxide NCs, near ambient pressure X-ray photoelectron spectroscopy (NAP-XPS), X-ray diffraction (XRD), and X-ray absorption spectroscopy (XAS) were introduced under catalytically relevant CO oxidation conditions.[25,26] An improvement in the CO oxidation rate was observed compared to the intrinsic CO oxidation activity of spinel oxide NCs with well-defined (100) facets. The chemical changes at the interface coming from the deposition of a CeO_2 surface layer on the oxide core affected the overall reactivity of the oxide catalyst. H_2 oxidation was also carried out on catalytic nanodiodes by measuring the chemicurrent to investigate charge transfer at the interface.

2.2. MATERIALS AND METHODS

2.2.1. Chemicals

Cobalt(II) perchlorate hexahydrate ($Co(ClO_4)_2$), manganese acetate tetrahydrate ($Mn(Ac)_2$, 98%), iron acetylacetonate ($Fe(acac)_3$, 97%), cerium(III) nitrate hexahydrate ($Ce(NO_3)_3$, 99%), oleylamine (technical grade, 70%), oleic acid (technical grade, 90%), decanoic acid (98%), formic acid (reagent grade, ≥95%), benzyl ether (98%) and 1-octanol (anhydrous, ≥99.0%) were purchased from Sigma-Aldrich. *O*-Xylene (≥98.5%) was obtained from Junsei Chemicals Co., Ltd. All chemicals were used as received without any further purification.

2.2.2. Synthesis of Spinel Oxide NCs

The Co_3O_4 NCs were synthesized according to the reported method.[27] A mixture of $Co(ClO_4)_2$ (0.37 g) and oleylamine (2.7 g) in 1-octanol (15 mL) was heated to 393 K in air. Distilled water (0.7 mL) was injected during heating before the temperature reached 393 K, and then the reaction mixture was maintained at 393 K for 2 h. Similarly, the Mn_3O_4 NCs were synthesized using a mixture of $Mn(Ac)_2$ (0.25 g), oleylamine (1.4 g), and oleic acid (0.28 g) in *o*-xylene (15 mL) after the thermal reaction at 363 K for 1.5 h.[28] The Fe_3O_4 NCs were synthesized using $Fe(acac)_2$ (0.36 g), decanoic acid (0.69 g), and benzyl ether (10 mL) after the reaction at 663 K for 30 min.[31] After cooling, excess acetone and ethanol were added to the reaction solution, then the resulting spinel oxide NCs were retrieved by

centrifugation.

2.2.3. Selective Deposition of CeO_2 on the Oxide NCs

The as-synthesized oxide NCs (0.080 g for Co_3O_4, 0.076 g for Mn_3O_4, and 0.078 g for Fe_3O_4) were dispersed in an organic/aqueous suspension consisting of oleylamine, formic acid, and *o*-xylene (15 mL). The suspension was heated to 363 K and held at this temperature for 1.5 h. Upon reaching 363 K, a cerium(III) nitrate solution (1 M, 1 mL) was injected into the solution. After the reaction, excess ethanol was poured into the solution and the resulting oxide-CeO_2 NCs were collected by centrifugation. The coverage of CeO_2 on the oxide NCs was controlled using different ratios of oleylamine and formic acid. For example, when 5 mmol of oleylamine and 4.5 mmol of formic acid were used during preparation of the Co_3O_4 NCs, CoCe-1F was produced. Similarly, CoCe-3F and CoCe-6F were produced using 2.5 mmol of oleylamine with 2.25 and 1.6 mmol of formic acid, respectively.

2.2.4. Preparation of the Monolayer Films using the Langmuir-Blodgett Technique

A monolayer of oleylamine-capped Co_3O_4/CeO_2 NCs was obtained using a Langmuir-Blodgett trough (Nima Technology, M611). A solution (50 μL) containing 10 $mg \cdot mL^{-1}$ of the colloidal NCs dispersed in chloroform was dropped onto the water surface of the LB bath. After 30 min, chloroform was evaporated and the suspended NCs were compressed until the surface pressure reached 40 $mN \cdot m^{-1}$. After holding for 30 min, the resulting LB film

was transferred onto a Si wafer. Prior to the catalytic measurements, the oleylamine surfactant on the surface of NCs was removed by UV-ozone treatment. Two types of Hg lamps emitting 185 and 254 nm photons were irradiated onto the NC films for 2 h to induce photodecomposition of the surfactant by ozone without damaging the nanoparticle core.

2.2.5. Catalytic CO Oxidation

CO oxidation was performed in a batch reactor using the deposited monolayer NP catalysts. After placing the catalyst on the plate heater, the chamber with an internal volume of 1 L was evacuated to 1×10^{-8} Torr using rotary and turbomolecular pumps sequentially. Subsequently, 70 Torr of CO and 70 Torr of O_2 balanced with Ar (620 Torr) were sequentially charged. After stabilizing at the reaction temperature for 30 min, the reactants and products were continuously circulated using a circulating pump at a rate of 5.5 $L \cdot min^{-1}$ and analyzed by gas chromatography (YL-6500) with thermal conductivity detection (TCD) using a Carboxen 1000 column (Supelco). The CO conversion was evaluated in the temperature range of 453–493 K, and the TOF was determined as the number of moles of produced CO_2 per mole of catalyst. The conversion rate was limited to <20% to maintain the reaction in the kinetically controlled regime. The TOF was calculated based on the turnover number (TON), which is the value of produced CO_2 molecules per Co active surface site per second as shown in the following equation:

$$TOF = \frac{TON}{\text{reaction time}} = \frac{\text{CO conversion} \times \frac{P_{CO}V}{RT} \times N_A}{\text{Co active surface site} \times \text{reaction time}}$$

The Co active surface site was determined based on the geometric dispersion of the Co_3O_4/CeO_2 NCs, which was measured by SEM observations of NC monolayer coverage on the Si substrate, and the number of sites was measured by CO chemisorption.

2.2.6. Characterization

TEM observations were performed using a JEM-2100F (JEOL) instrument with an acceleration voltage of 200 kV. HAADF-STEM and the corresponding EDS mapping observations were conducted using a dual spherical aberration-corrected TEM (Titan G2 60-300, FEI) with an acceleration voltage of 200 kV and a JEM-ARM200F operated at 200 kV (Cold Field Emission Type, JEOL) in the National Center for Inter-university Research Facilities at Seoul National University. For image recording and processing including Fourier filtering, digital micrograph software (GMS3.2, Gatan) was used. TGA was performed using a Q-5000 IR (TA Instrument). Powder XRD patterns were obtained using a Rigaku D/max 2500 diffractometer (Rigaku, Japan) equipped with a rotating anode and a Cu K Kα radiation source (λ = 0.15418 nm). XPS analysis was performed under Kα radiation using an Al Kα X-ray radiation source (Escalab 250Xi instrument, ThermoFisher, USA). The spectrum was obtained under 3×10^{-8} mbar of pressure. Raman spectra were recorded using A LabRAM HR Evolution (Horiba, equipped with laser excitation at

532 nm, carried out at the Research Institute of Advanced Materials (RIAM) at Seoul National University (SNU)). CO chemisorption experiments were performed by pulse injection using a BELCAT II instrument to evaluate the number of active sites in the NCs catalyst. To remove the organic surfactants from the NCs, the catalyst (50 mg) was pretreated at 573 K for 1 h under 20% O_2/He (50 mL·min^{-1}) and then cooled to 193 K. A CO pulse was injected into the cell under a flow of He. The operating conditions include the CO content in the pulse (5%), the total flow rate balanced with He (50 mL·min^{-1}), the pulse size (0.4 mL), and the time interval between pulses (4 min).

2.2.7. *In Situ* XRD, XAS, and NAP-XPS

In situ XRD experiments were carried out using a SmartLab (Rigaku) X-ray diffractometer equipped with a D/teX Ultra 250 detector using Cu Kα radiation. The NP catalyst on the substrate was placed in a Kanthal (FeCrAl) filament cavity and pretreated under a 20% O_2/He flow (50 mL·min^{-1}) at 573 K for 1 h to remove the surfactants. The measurements were carried out under a reducing environment with a flow of 5% CO/He (50 mL·min^{-1}) in the temperature range from 323 to 773 K (step size = 0.05°, 25 K intervals, 2θ range = 20–80°). XAS measurements for the Co K-edge and Ce L_3-edge were performed at beamline 7D of the Pohang Accelerator Laboratory (PAL). XAS data were processed using the ATHENA program of the IFEFFIT package.[48] *In situ* XANES measurements were performed in the transmittance detection mode at beamline 6D of the PAL. The catalyst was

placed in a gas flow cell consisting of a polyimide tube placed between penetrable beryllium windows. During the measurement, the reducing environment was maintained as a 5% CO/He flow (30 mL·min^{-1}) throughout the cell up to 673 K. As the oxidizing environment, additional O_2 (5%) was applied. XAS data were obtained after stabilization at the desired temperature for 30 min, and the measurement was repeated three times for accuracy. NAP-XPS was carried out in the Korea Basic Science Institute (KBSI). The system was manufactured by SPECS GmbH and consisted of a PHOIBOS 150 NAP analyzer, an X-ray monochromator with a Microfocus 500 Al Kα X-ray source (*hν* = 1486.74 eV), and an *in situ* gas reaction cell (DeviSim). The spectrum was obtained under 1 mbar CO. The binding energies of the obtained Ce 3*d* were corrected based on the position of the Ce^{4+} component (917.4 eV). The spectra were fitted with the Shirley background using a Voigt function with CasaXPS software. All spectra are presented without further manipulations.

2.2.8. Catalytic H_2 Oxidation on a Nanodiode

A thin layer of TiO_2 (250 nm thickness) was deposited on a SiO_2 wafer using a patterned aluminum shadow mask (4 × 6 mm^2) by electron beam evaporation. After the deposition of TiO_2, the Ti film was annealed under air at 653 K for 2 h to control the Fermi level. The electrode was fabricated by the deposition of 50 nm Ti and 150 nm Au layers through a second shadow mask (5 × 5 mm^2) by electron beam evaporation. Subsequently, a 10-nm-thick Au film was deposited through a third patterned shadow mask (2 × 1

mm^2). A monolayer of Co_3O_4-CeO_2 NCs was deposited on the nanodiode using the LB technique as described above. The H_2 oxidation reaction was performed in the same reactor as the CO oxidation experiments. Reactant gases consisting of 15 Torr of H_2 and 745 Torr of O_2 were charged into the chamber. The reaction was monitored at 313–363 K and 313–403 K, respectively, to determine the TOF and chemicurrent density.

2.3. Results and Discussions

2.3.1 Spinel Oxide NCs with Controlled CeO_2 Layers by Selective Deposition

As an active species for oxidation catalysts, uniform spinel oxide NCs exposing defined (100) facets including Co_3O_4, Mn_3O_4, and Fe_3O_4 were synthesized according to the previously reported methods.[27–29] We performed a controlled deposition of CeO_2 by oxidizing the Ce^{3+} precursor in a suspension of the spinel oxide NCs to produce CeO_2-deposited spinel oxide NCs. This selective deposition method was applied by varying the reaction parameters, including the pH and surfactant concentration (Fig. 2.1a). Initially, CeO_2 clusters of sub-nanometer size were formed as building blocks, which were then attached to the NC corners where long-chain ligands were loosely packed.[30] Finally, CeO_2-oriented aggregation took place from the corner to the surface.[31,32] The produced CeO_2-deposited spinel oxide NCs with 1, 3, and 6 facets of the CeO_2 layer are denoted as MCe-1F, MCe-3F, and MCe-6F NCs, respectively (M = Co, Mn, Fe). High-angle annular dark-field scanning transmission electron microscopy (HAADF-STEM) and corresponding energy dispersive X-ray spectroscopy (EDS) mapping images confirm the presence of Co_3O_4 and Co_3O_4-CeO_2 NCs (Fig. 2.1b–e). The as-synthesized Co_3O_4 NCs consisting of only (100) facets have an average edge length of 11 nm. They show the typical {100}, {110}, and {311} Bragg reflections of spinel Co_3O_4 in a fast Fourier

transform (FFT) pattern taken along the <001> zone axis in the electron microscopy image (Fig. 2.1b,f). For CoCe-1F, the polycrystalline CeO_2 layers cover only one plane of the NCs (Fig. 2.1 and Fig. 2.2f), whereas CoCe-3F and CoCe-6F present relatively flat CeO_2 layers (ca. 2 nm thick) covering 3 and 6 facets of the NCs, respectively (Fig. 2.1d,e and Fig. 2.2g,h). In the low-magnification 2D TEM images, 22.5, 52.4, and 99.2% of the sides in the square Co_3O_4 are covered with CeO_2 in the cases of CoCe-1F, CoCe-3F, and CoCe-6F, respectively (Fig. 2.2e-k). EDS and energy-filtered TEM images demonstrate the controlled deposition of CeO_2 shells (insets of Fig. 2.1b–e and Fig. 2.2a-d). The Ce M edge electron energy loss spectroscopy (EELS) line scan along the center of CoCe-6F demonstrates that CeO_2 was deposited not only on the edge sites but also on the plane surfaces (Fig. 2.1i). The deposited CeO_2 layer consists of small aggregated clusters (~3 nm) with distinct grain boundaries, demonstrating that aggregation-based growth took place (Fig. 2.2l,m).[33] The FFT of the CoCe-6F HAADF-STEM image taken along the Co_3O_4 <001> zone axis (Fig. 2.1f,g) shows the discontinuous ring pattern of CeO_2 {111}. Different coverages of the ensemble NCs were also confirmed by thermogravimetric analysis (TGA) where the temperature of the weight loss, which is attributed to the organic capping molecules present on the NCs, is dependent on the degree of CeO_2 coverage. More specifically, with an increased CeO_2 coverage, the weight loss began at lower temperatures due to the weaker surface binding of organic molecules to the CeO_2 surface compared to that

of Co_3O_4 (Fig. 2.3). These weight loss results agree with the trend observed in the TEM results. An examination of the high-magnification STEM (Fig. 2.1h), XRD (Fig 2.4), and extended X-ray absorption fine structure (EXAFS, Fig.2.5) images also shows that there is no epitaxial deposition of CeO_2 on the Co_3O_4 (100).[34] Consequently, we reveal that the non-epitaxially grown CeO_2 layer present on Co_3O_4 does not alter either the crystallographic feature or the oxidation state of the Co_3O_4 NCs.

To investigate the synthetic mechanism of the selective deposition of CeO_2, we controlled two main factors, namely the pH and the surfactant concentration. At the high pH obtained using low concentrations of formic acid, the sol-gel reaction of CeO_2 was promoted to obtain a high rate of CeO_2 cluster formation and corner nucleation on the densely charged Co_3O_4 surface.[35–37] As the pH increases from 5.9 to 6.8, the CeO_2 coverage increases from half to full cover with a higher deposition rate, leading to multi-corner deposition and a higher coverage (Fig. 2.6). High surfactant concentrations (0.3 M) produced uniform Co_3O_4 NCs that maintain a low CeO_2 coverage without forming undeposited NCs (Fig. 2.7). The reaction parameters including pH and surfactant concentration are critical to manipulate the corner nucleation and selective deposition of the CeO_2 layer (Fig, 2.8). In addition to Co_3O_4, the selective deposition of CeO_2 is generally applied to similar spinel oxide NCs such as Mn_3O_4 and Fe_3O_4. The as-synthesized Mn_3O_4 and Fe_3O_4 NCs have edge lengths of ~15 nm (Fig. 2.9a,e). The FFT patterns of Mn_3O_4 and Fe_3O_4 taken along the <001> zone

axis show the typical Bragg reflections of {200} and {220} of Mn_3O_4 (Fig. 2.10a), and the {220} and {400} reflections of Fe_3O_4 (Fig. 2.10b), respectively. In the HAADF-STEM and corresponding EDS mapping images, CeO_2 layers were found to be deposited on the 1, 3, and 6 facets of the Mn_3O_4 NCs and the Fe_3O_4 NCs (Fig. 2.9). Their low-magnification TEM images are presented in Fig 2.11. The overall results demonstrate that the current selective deposition protocol provides a general method to prepare various heterostructured oxide NPs with finely tuned interfaces. To the best of our knowledge, the present work is the first to report on the generation of spinel oxide NCs with a different number of facets covered by CeO_2 layers in a controlled manner.

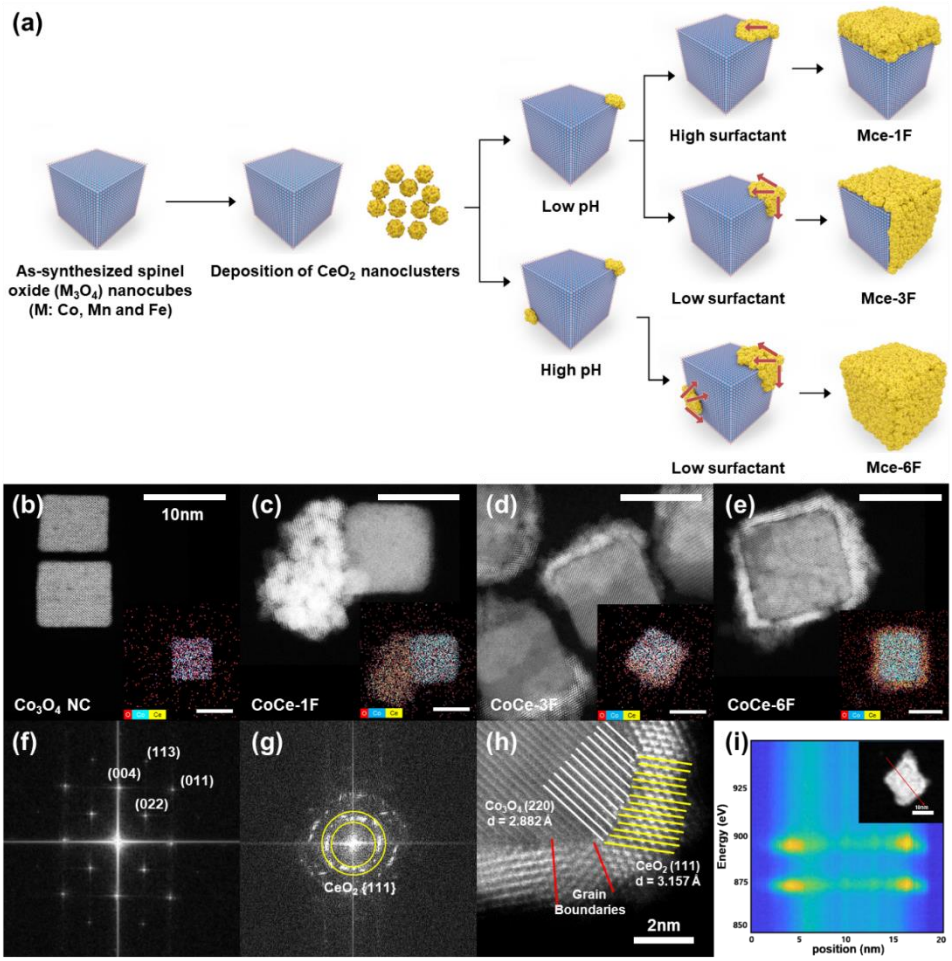

Figure 2.1. Synthesis and characterization of the Co_3O_4-CeO_2 NCs. (a) Schematic illustration of the preparation of CeO_2-deposited spinel oxide NCs with a controlled layer of CeO_2. (b–e) HAADF-STEM images and EDS mappings (inset) of Co_3O_4 NCs with 1, 3, and 6 facets covered by CeO_2: (b) Co_3O_4, (c) CoCe-1F, (d) CoCe-3F, and (e) CoCe-6F. Scale bars represent 10 nm. FFT patterns of (f) Co_3O_4 and (g) CoCe-6F taken along the <100> direction of Co_3O_4. (h) High resolution HAADF-STEM image of CoCe-6F. (i) Line scan EELS spectrum of CoCe-6F along the particle center (Inset: the scan direction).

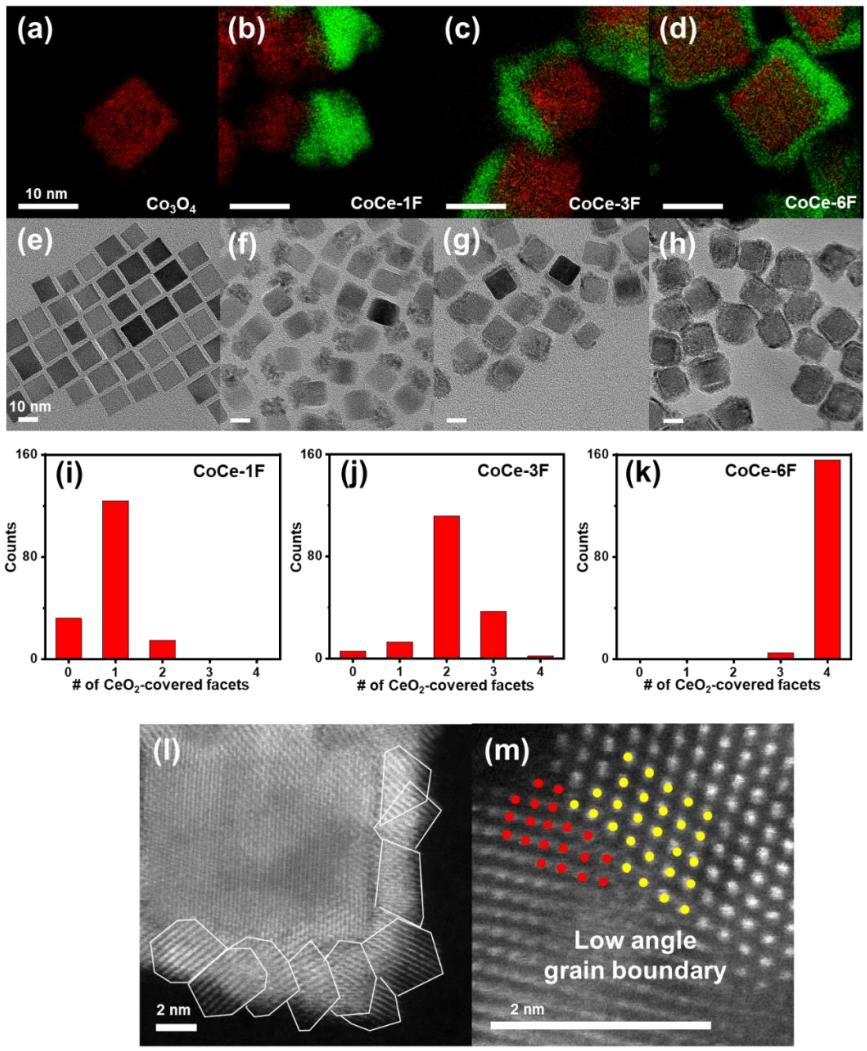

Figure 2.2. Detailed electron microscopy images of the Co_3O_4/CeO_2 NCs. (a–d) Energy-filtered transmittance electron microscopy (EF-TEM) mapping and (e–h) the corresponding TEM images of (a, e) the Co_3O_4 NCs, (b, f) CoCe-1F, (c, g) CoCe-3F, and (d, h) CoCe-6F. (i–k) Histograms of the number of CeO_2-covered facets as determined by TEM images for (i) CoCe-1F, (j) CoCe-3F, and (k) CoCe-6F. (l) Multi-domains of the CeO_2 layers of CoCe-6F observed by HAADF-STEM imaging. (m) HR-TEM image of a grain boundary created between two adjacent CeO_2 domains.

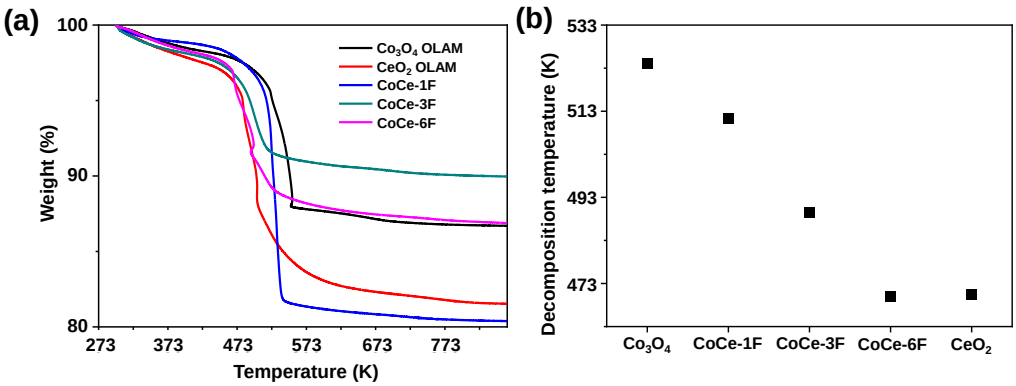

Figure 2.3. (a) TGA curves, and (b) the corresponding decomposition temperatures of the organic surfactants on the Co_3O_4-CeO_2 NCs with different CeO_2 coverages.

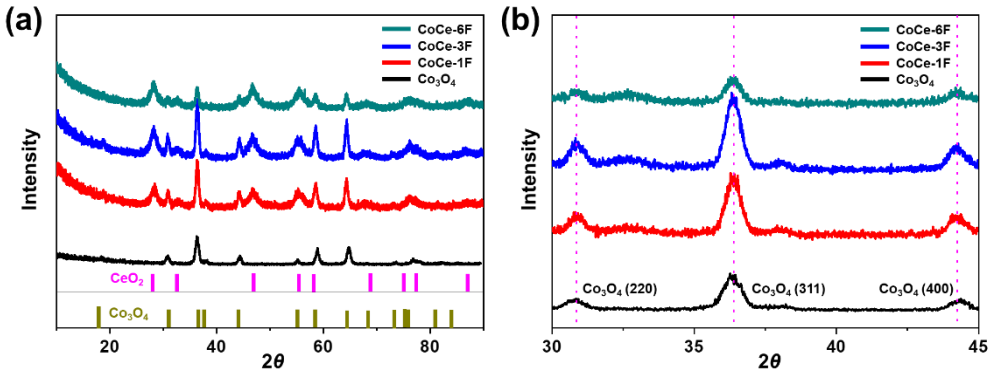

Figure 2.4. Powder X-ray diffraction (XRD) patterns of Co_3O_4-CeO_2 NCs with different CeO_2 coverages. (a) XRD patterns of Co_3O_4/CeO_2 NCs. Both Co_3O_4 (JCPDS #42-1467) and CeO_2 (JCPDS #81-0792) are confirmed in Co_3O_4/CeO_2 NCs. (b) The enlarged XRD peaks from 30 to 45°. The peak shift is negligible regardless of the CeO_2 coverage.

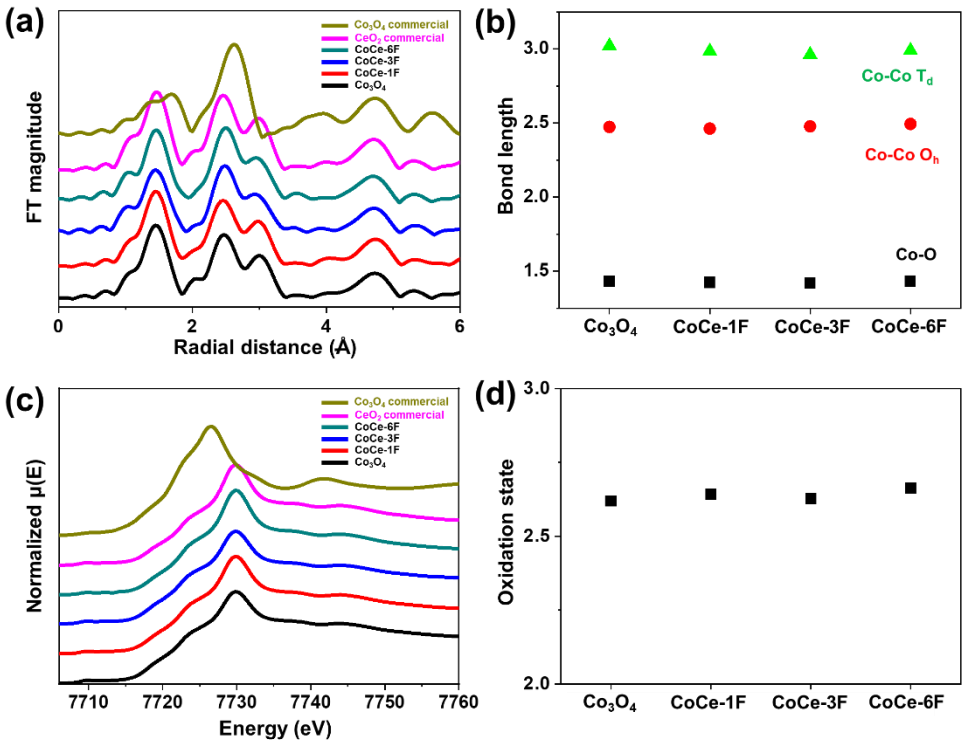

Figure 2.5. X-ray absorption spectroscopy (XAS) of Co_3O_4-CeO_2 NCs with different CeO_2 coverages. (a) k^2-weighted Fourier-transform extended X-ray absorption fine structure (EXAFS) spectra at Co K-edge. (b) A bond length of Co_3O_4-CeO_2 NCs determined from a. Change in bond length of Co_3O_4 originated from the CeO_2 deposition is negligible. (c) Co K-edge X-ray absorption near edge spectra (XANES) of Co_3O_4-CeO_2 NCs. (d) Oxidation state of cobalt calculated by linear combination fitting. A small change in the oxidation state of Co_3O_4 from the CeO_2 deposition is observed (less than 2%).

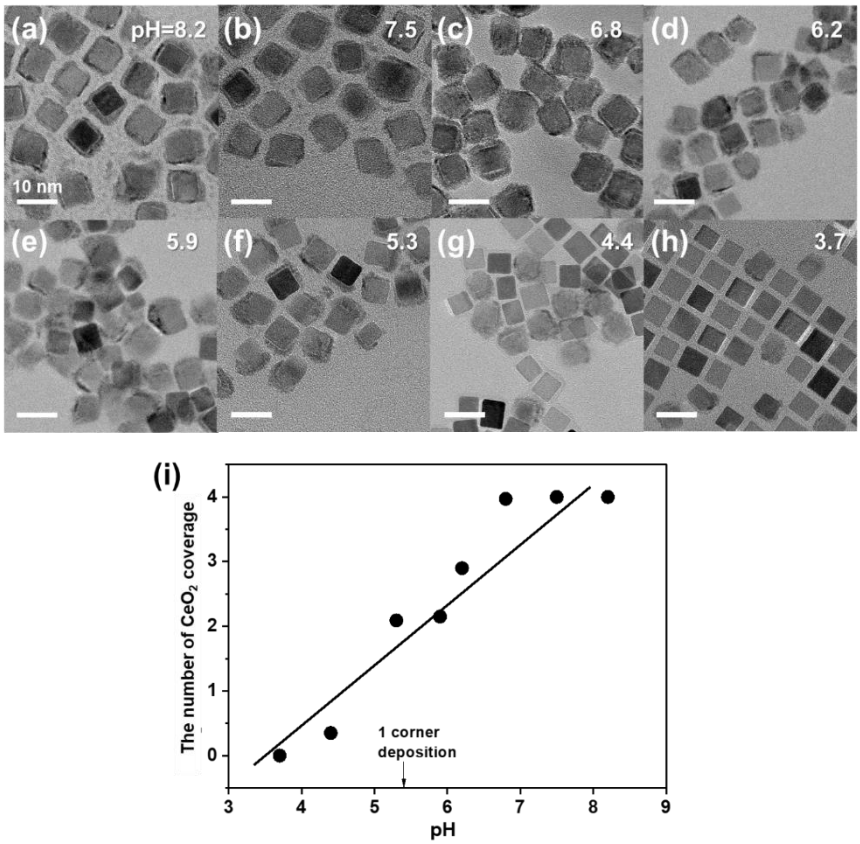

Figure 2.6. TEM images of Co_3O_4-CeO_2 NCs generated by the coverage control according to the pH. Co_3O_4-CeO_2 NCs were synthesized at different pH: (a) 8.2, (b) 7.5, (c) 6.8, (d) 6.2, (e) 5.9, (f) 5.3, (g) 4.4, and (h) 3.7. As the pH increases, the coverage increases. For example, Co_3O_4-CeO_2 NCs are half covered at pH 5.3, while Co_3O_4-CeO_2 NCs are completely covered at pH 6. (I) A plot of pH dependent CeO_2 coverage.

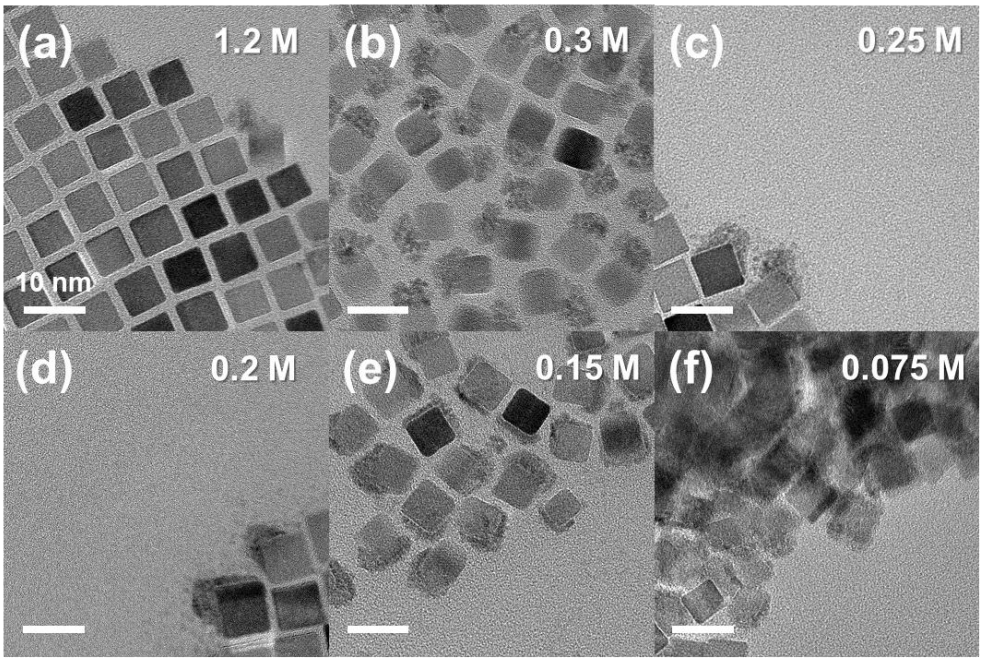

Figure 2.7. TEM images of Co_3O_4-CeO_2 NCs generated by coverage control according to surfactant concentration. Co_3O_4-CeO_2 NCs were synthesized at different surfactant concentrations: (a) 1.2, (b) 0.3, (c) 0.25, (d) 0.2, (e) 0.15, and (f) 0.075 M.

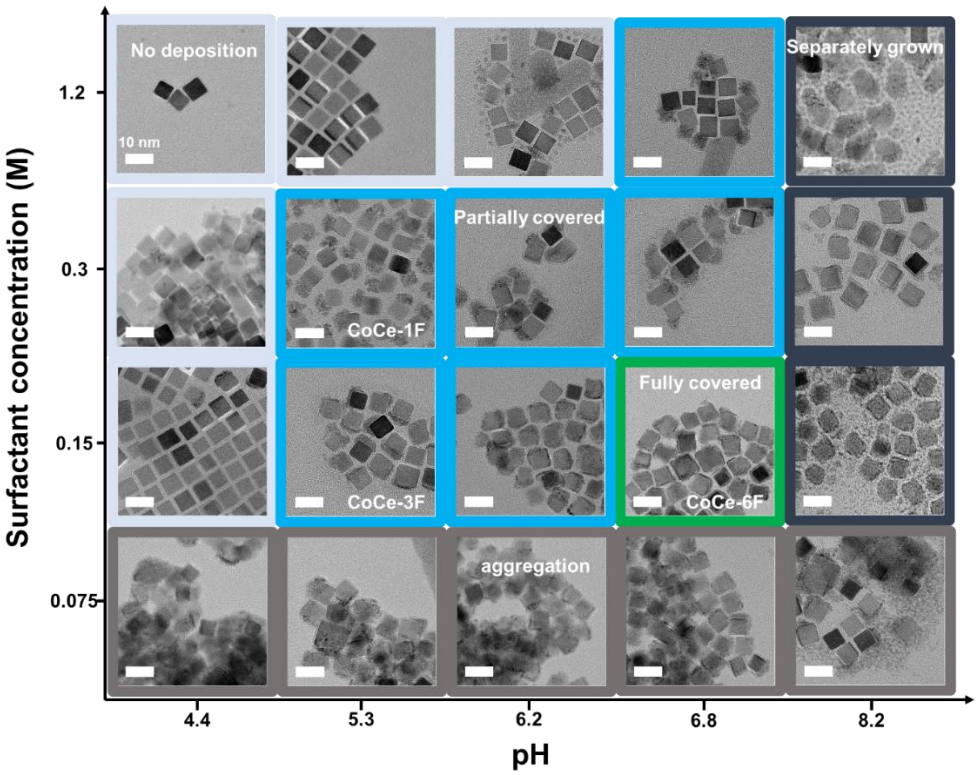

Figure 2.8. TEM images of various Co_3O_4-CeO_2 NCs controlled by pH and surfactant concentration.

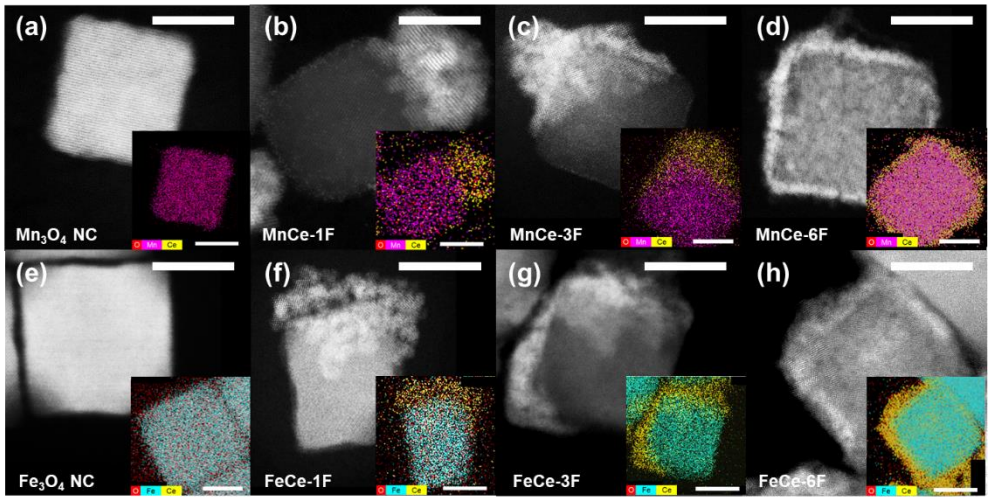

Figure 2.9. Structural characterization of the Mn_3O_4-CeO_2 NCs and the Fe_3O_4-CeO_2 NCs. (a-h) HAADF-STEM images and EDS mappings (inset) of Mn_3O_4 and Fe_3O_4 NCs covered with 1, 3, and 6 facets of CeO_2: (a) Mn_3O_4, (b) MnCe-1F, (c) MnCe-3F, (d) MnCe-6F, (e) Fe_3O_4, (f) FeCe-1F, (g) FeCe-3F, and (h) FeCe-6F. Scale bars represent 10 nm.

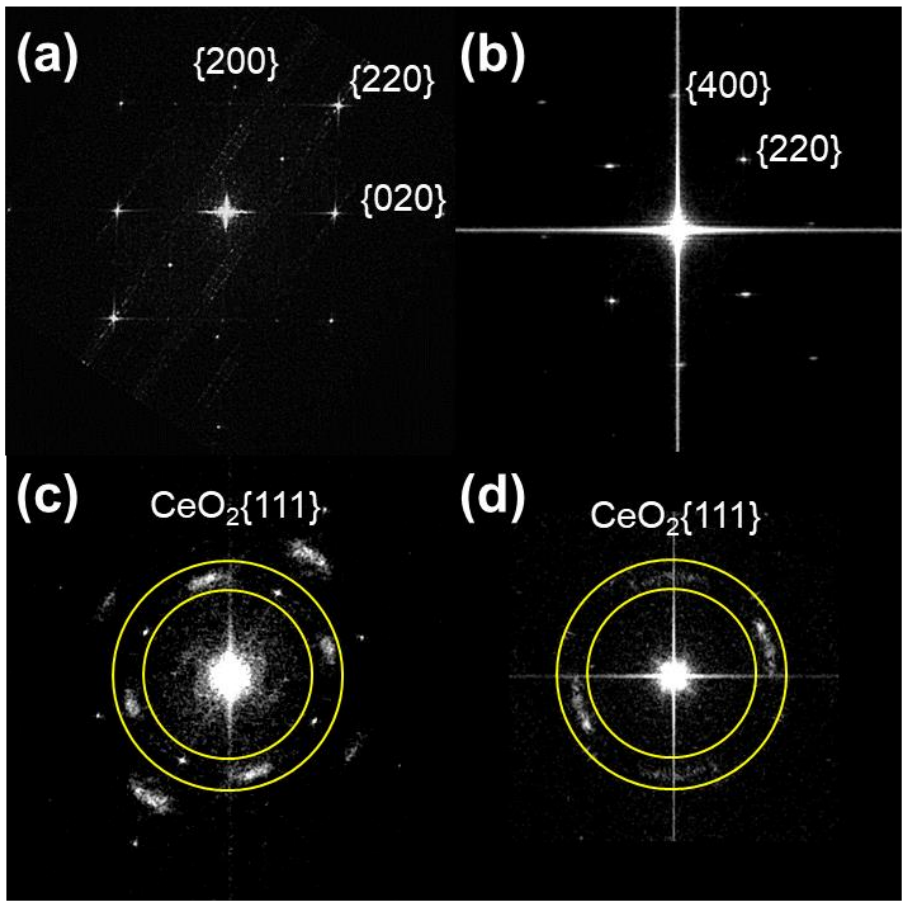

Figure 2.10. Fast Fourier Transform (FFT) patterns of Mn_3O_4/CeO_2 NCs and Fe_3O_4/CeO_2 NCs. (a) FFT pattern of Mn_3O_4 NCs taken along the Mn_3O_4 <001> zone axis. (b) FFT pattern of Fe_3O_4 NCs taken along the Fe_3O_4 <001> zone axis. (c) FFT pattern of MnCe-6F taken along the Mn_3O_4 <001> zone axis. (d) FFT pattern of FeCe-6F taken along the Fe_3O_4 <001> zone axis. The FFT of MCe-6F has discontinuous ring patterns of CeO_2.

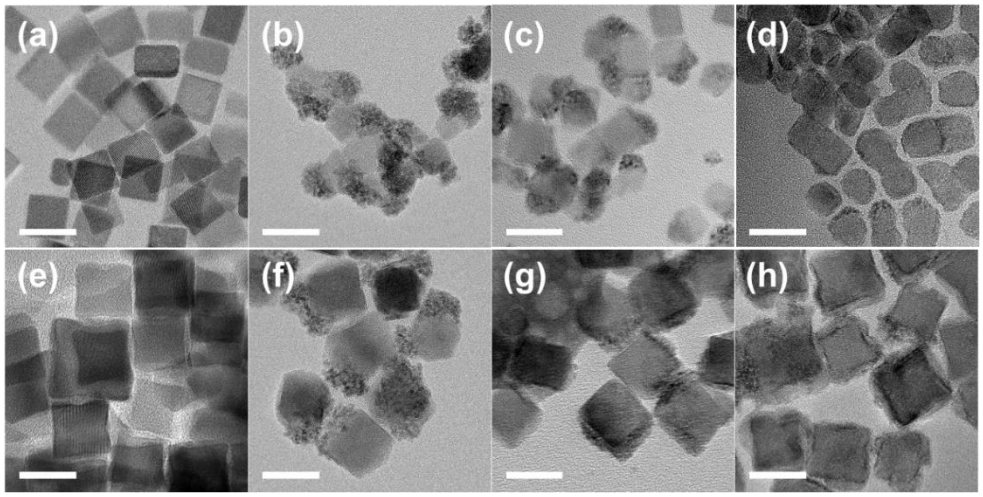

Figure 2.11. TEM images of Mn_3O_4/CeO_2 and Fe_3O_4/CeO_2 NCs. (a) Mn_3O_4 NCs, (b) MnCe-1F, (c) MnCe-3F, (d) MnCe-6F, (e) Fe_3O_4 NCs, (f) FeCe-1F, (g) FeCe-3F, and (h) FeCe-6F. Scale bars are 20 nm.

2.3.2. Catalytic CO Oxidation

CO oxidation was carried out as a model reaction to investigate the interfacial effect on the catalytic performance of the heterostructured oxide NCs. For this reaction, colloidal spinel oxide-CeO_2 NCs were deposited on a silicon substrate to prepare a NP monolayer (Fig. 2.12a).[38] To remove the organic surfactants attached to the NPs, UV-ozone treatment was conducted (Fig. 2.12b).[39] The CO oxidation results obtained for the Co_3O_4-CeO_2 NCs, including the turnover frequency (TOF), Arrhenius plot, and activation energy in the temperature range of 453–493 K, are shown in Fig. 2.13a and 2.13b and in Table 2.1, respectively. As indicated, the TOF values of the Co_3O_4-CeO_2 NCs were significantly improved at all temperatures compared to the pristine Co_3O_4 NC without CeO_2 deposition. In particular, the TOF of CoCe-3F was found to be 17.95 s^{-1} at 493 K, which is significantly higher than that of Co_3O_4 NCs (i.e., 1.54 s^{-1}). The activation energy derived from the Arrhenius plots reveals that CoCe-3F has a lower activation energy than the pristine Co_3O_4, demonstrating the interfacial effect generated by the deposition of CeO_2 on Co_3O_4 (Fig 2.13b). In addition, CoCe-3F exhibits a superior CO oxidation performance to CoCe-6F. The same trend was also found when CO oxidation was carried out using a series of Co_3O_4-CeO_2 NC catalysts in a fixed bed reactor (Fig. 2.14). This unexpected result suggests that while the additional CeO_2 layer enhances the activity of the active Co_3O_4 sites in the case of CoCe-3F, the excessive coating of CeO_2 in CoCe-6F blocks the surface of the core Co_3O_4, thereby reducing its catalytic

activity. CO chemisorption experiments indicate that CoCe-6F has a smaller area of CO uptake than CoCe-3F, because the exposed Co_3O_4 surface is smaller in the case of CoCe-6F (Fig. 2.15). After the reaction, the original morphologies of Co_3O_4, CoCe-1F, CoCe-3F, and CoCe-6F NCs were retained without any aggregation (Fig. 2.16).

CO oxidation was further investigated under various reaction environments with different proportions of CO and O_2. As the CO/O_2 ratio increased from 0.4 to 6.0, the maximum TOF was obtained at a CO/O_2 ratio of 1.0 for CoCe-3F and CoCe-6F and at a CO/O_2 ratio of 2.5 for Co_3O_4 NCs and CoCe-1F (Fig. 2.13c). The TOF was substantially suppressed at a CO/O_2 ratio of 6.0 for all of the Co_3O_4-CeO_2 NC catalysts. These results show that the supply of dissociated oxygen atoms is insufficient for an extremely high CO concentration at a CO/O_2 ratio of 6.0, which leads to a decrease in the CO oxidation rate.[40,41] In contrast, under O_2-deficient conditions, the TOF of CoCe-3F did not drop significantly, unlike those of CoCe-1F and CoCe-6F. This was attributed to the fact that oxygen is more effectively transferred from CeO_2 at the interface in the case of CoCe-3F than in the cases of CoCe-1F and CoCe-6F. For the same amount of Co_3O_4, the exposed active Co_3O_4-CeO_2 interface was maximized at CoCe-3F, achieving the highest CO oxidation rate due to the high oxygen storage capacity and the facile formation of oxygen vacancies in the case of CeO_2. The same trend was observed for Mn_3O_4-CeO_2 NCs. Although less reactive than Co_3O_4, Mn_3O_4 also exhibits an intrinsic reactivity for CO oxidation.[22]

The reaction temperature range for Mn_3O_4-CeO_2 NCs is relatively higher than that of Co_3O_4-CeO_2 (i.e., 533–573 K), but the calculated TOF values follow the same order: MnCe-3F > MnCe-6F > MnCe-1F > Mn_3O_4 NCs (Fig. 2.17). This result is consistent with the previous report that the CO oxidation activity of Mn_3O_4 increases when CeO_2 is added to the Mn_3O_4 catalyst.[42] Because of the poor intrinsic CO oxidation activity of Fe_3O_4, the interfacial effect was not observed in the Fe_3O_4-CeO_2 NCs. Detailed TOF values for Mn_3O_4-CeO_2 are provided in Table 2.2.

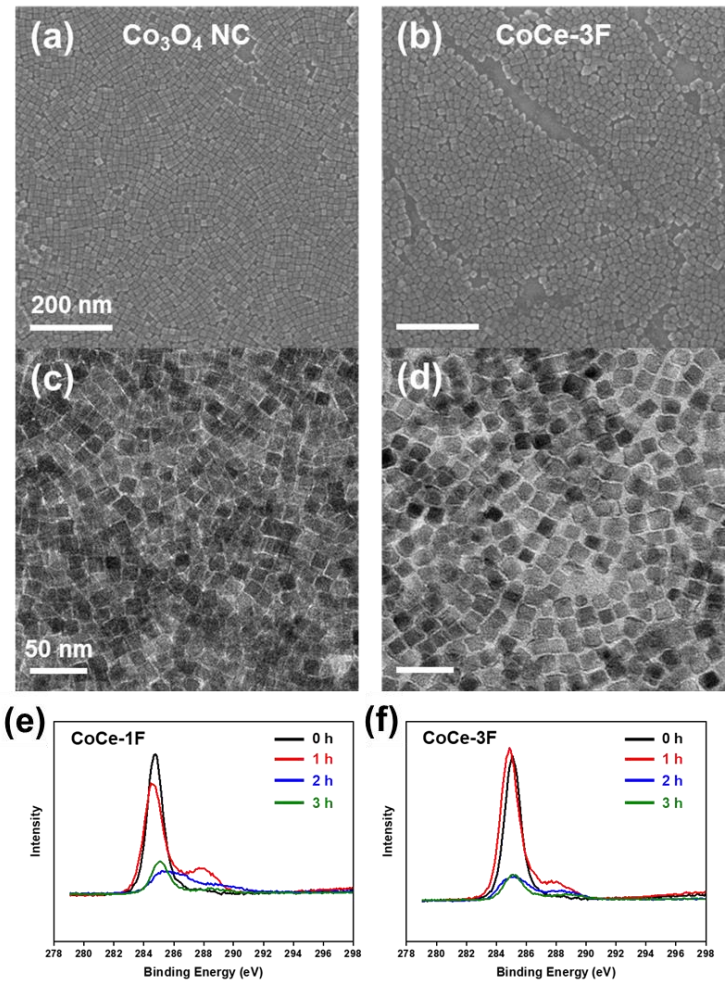

Figure 2.12. Characterizations of nanoparticle monolayers prepared by the Langmuir-Blodget (LB). (a, b) Scanning electron microscopy (SEM) and (c, d) Transmittance electron microscopy (TEM) images of (a, c) Co_3O_4 and (b, d) CoCe-3F NCs. (e,f) X-ray photoelectron spectrum (XPS) of NCs after the removal of surfactants. XPS of C 1*s* spectra of (e) CoCe-1F and (f) CoCe-3F NCs after UV-ozone treatment at different times (0, 1, 2, and 3 h). Removal of carbon species confirms the removal of oleylamine surfactant on the nanoparticle surface. XPS results demonstrate that the 2 hours of UV-ozone treatment time is sufficient to completely remove the surfactant.

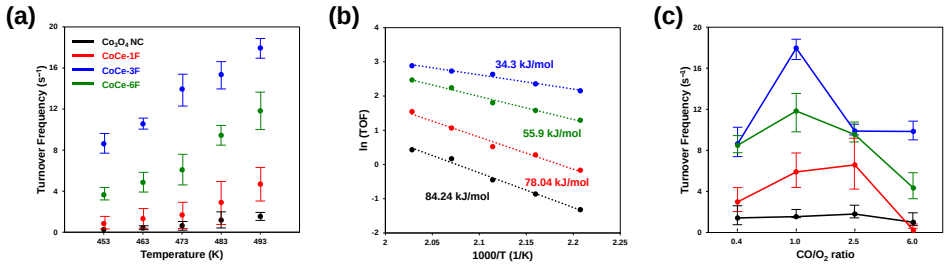

Figure 2.13. CO oxidation for the Co_3O_4-CeO_2 NCs. CO oxidation results: (a) TOFs at the temperature range of 453–493 K with a CO/O_2 ratio of 1.0, (b) Arrhenius plots and the calculated activation energies. (c) TOFs for reactions with different CO/O_2 ratios.

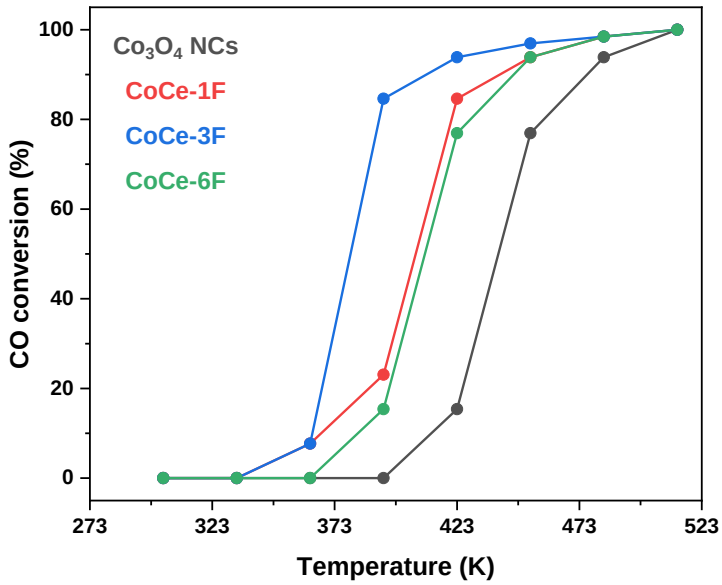

Figure 2.14. CO oxidation results for the CoCe catalysts in a fixed bed reactor. The reaction was carried out using 20 mg of catalyst mixed with 100 mg quartz powder (to avoid mass and heat transfer limitations). Prior to carrying out any measurements, the catalyst was pretreated at 573 K under 20% O_2 with an Ar flow for 1 h to remove any organic capping molecules. CO oxidation was performed with a feed stream consisting of 2% CO and 2% O_2, balanced with Ar (total flow rate = 50 mL min^{-1}, heating rate = 5 K min^{-1}).

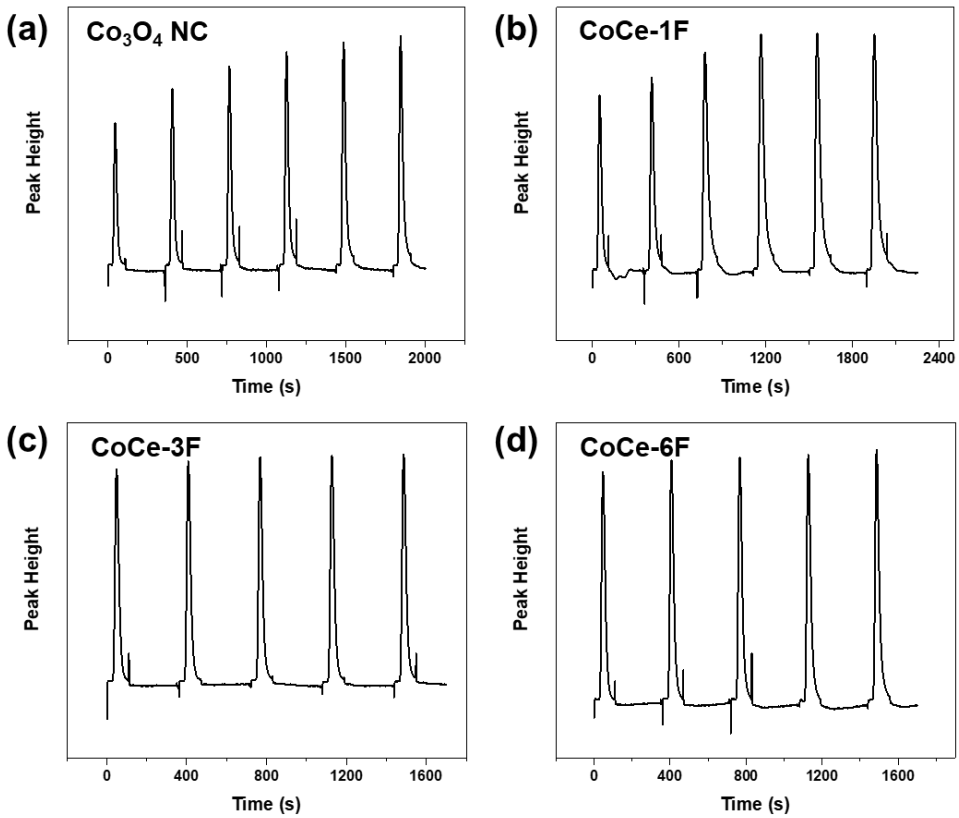

Figure 2.15. CO chemisorption measurement to determine the amount of Co_3O_4 sites. Time-dependent CO uptakes of (a) Co_3O_4, (b) CoCe-1F, (c) CoCe-3F, and (d) CoCe-6F NCs. The calculated areas of the CO uptake are 28701, 10383, 3208, and 1952, respectively. The ratio of CO adsorption to Co atom was estimated as 1:1 by assuming that CO was adsorbed on top of a Co metal atom. A negligible amount of CO (642; 2% of pristine Co_3O_4) was adsorbed to CeO_2.

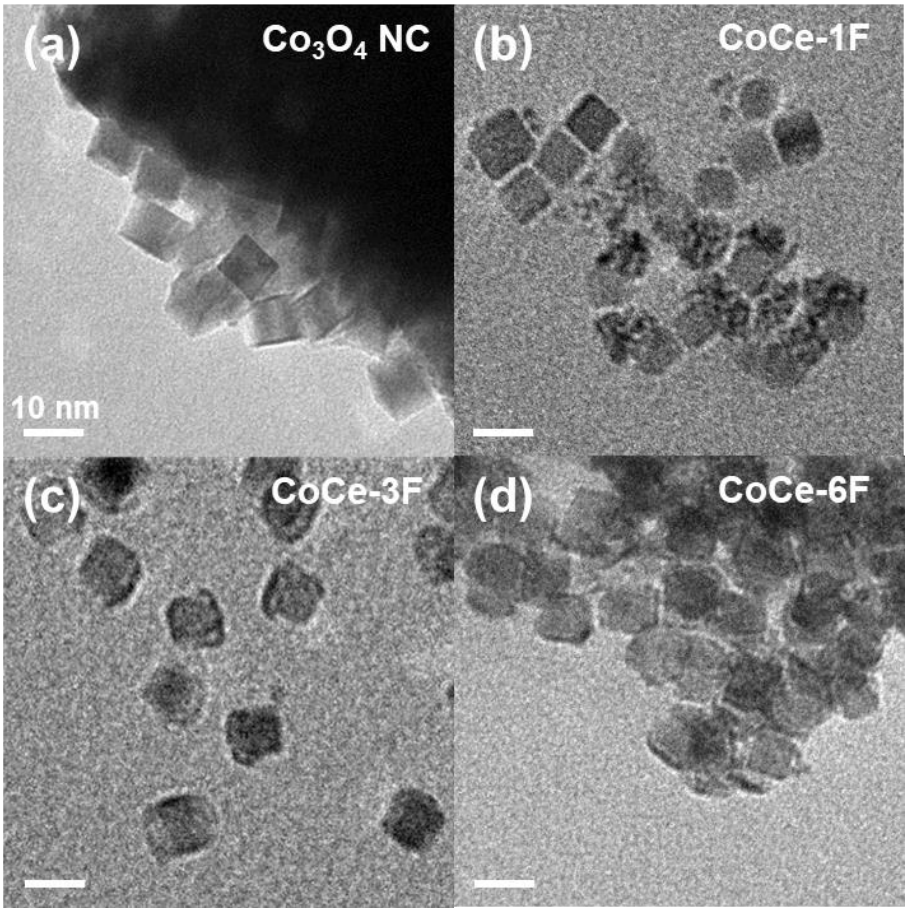

Figure 2.16. TEM images of the spent catalysts after CO oxidation. (a) Co_3O_4, (b) CoCe-1F, (c) CoCe-3F, and (d) CoCe-6F NCs. The original structure of NCs is maintained after the reaction.

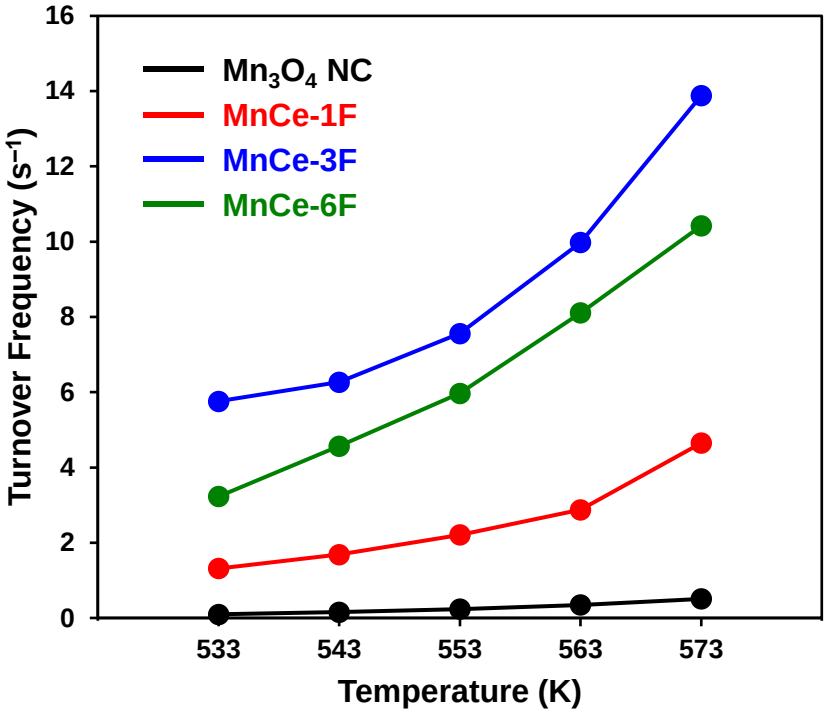

Figure 2.17. TOF values of Mn_3O_4-CeO_2 NCs for CO oxidation in the temperature range of 533–573 K.

Table 2.1. Calculated TOFs of Co_3O_4-CeO_2 NCs at different CO oxidation conditions.

	TOF (s^{-1}) by temperature (K)				
Catalyst	**453**	**463**	**473**	**483**	**493**
Co_3O_4 cube	0.27	0.42	0.64	1.18	1.54
CoCe-1F	0.84	1.33	1.69	2.91	5.90
CoCe-3F	8.62	10.56	13.95	15.36	17.95
CoCe-6F	3.65	4.86	6.08	9.44	11.83

	ln (TOF) by 1000/T (1/K)				
Catalyst	**2.05**	**2.1**	**2.15**	**2.2**	**2.25**
Co_3O_4 cube	0.43	0.17	-0.45	-0.86	-1.32
CoCe-1F	1.55	1.07	0.52	0.28	-0.17
CoCe-3F	2.89	2.73	2.64	2.36	2.15
CoCe-6F	2.47	2.24	1.80	1.58	1.30

	TOF (s^{-1}) by gas composition ratio of CO/O_2			
Catalyst	**0.4**	**1.0**	**2.5**	**6.0**
Co_3O_4 cube	1.41	1.54	1.80	0.99
CoCe-1F	2.98	5.90	6.58	0.20
CoCe-3F	8.60	17.95	9.88	9.84
CoCe-6F	8.49	11.83	9.53	4.33

Table 2.2. Calculated TOFs of Mn_3O_4-CeO_2 NCs in CO oxidation.

Catalyst	TOF (s^{-1}) by temperature (K)				
	533	543	553	563	573
Mn_3O_4 cube	0.10	0.16	0.24	0.35	0.51
MnCe-1F	1.32	1.69	2.21	2.88	4.65
MnCe-3F	5.76	6.27	7.56	9.98	13.88
MnCe-6F	3.23	4.57	5.97	8.11	10.42

2.3.3. Changes in the Crystal Structure under Different Reaction Conditions

The crystal structure and oxidation state of the heterostructured oxide NCs were investigated under various reaction conditions. The crystal structures of the spinel oxide NCs with and without the CeO_2 layer were identified by *in situ* XRD as the temperature was increased up to 773 K in a reducing environment. Fig. 2.18a–c show the results for the phase transformation of the Co_3O_4 NCs and CoCe-6F as observed using XRD measurements (see Fig. 2.19 for details). The fully oxidized catalyst treated with 20% O_2/He was exposed to the reducing conditions with a flow of 5% CO/He (50 mL·min^{-1}) in the temperature range of 323–773 K. The pristine Co_3O_4 NCs were found to exhibit a typical spinel structure up to 473 K, while the CoO phase appears at temperatures higher than 473 K and persists up to 573 K. When the temperature exceeds 573 K, the CoO peak intensity gradually decreases, and a metallic Co peak is clearly observed. When the CeO_2 layer is attached to the Co_3O_4 NCs, the spinel Co_3O_4 pattern is clearly observed by XRD, while no clear CeO_2 peak was observed due to significant peak broadening attributed to the small grain size (Fig. 2.4). Upon increasing the temperature under the CO atmosphere, the overall reduction of the core Co_3O_4 NCs was substantially inhibited by the CeO_2 layers. CoCe-6F undergoes a phase transformation from Co_3O_4 to CoO at 473 K, but the metallic Co phase was essentially not observed up to a temperature of 773 K. In addition, the region of CoO existence was found to

grow with the growth of the CeO_2 layer from CoCe-1F to CoCe-6F (Fig. 2.18c). Based on these results, the CeO_2 layer appeared to prevent the reduction of the Co_3O_4 NCs by supplying oxygen to the Co_3O_4 at the Co_3O_4-CeO_2 interface. Likewise, the reduction of Mn_3O_4 was suppressed by the CeO_2 shell in the Mn_3O_4-CeO_2 NCs. The initial Mn_3O_4 phase was converted to the MnO phase as the temperature was increased under the CO atmosphere. The MnO phase appeared at 623 K in the pristine Mn_3O_4 NCs, but the XRD pattern of MnCe-6F NCs showed only a Mn_3O_4 phase (Fig. 2.20). Moreover, the Fe_3O_4-CeO_2 NCs maintained the Fe_3O_4 phase up to 773 K, indicating that Fe_3O_4 was barely reduced by CO alone (Fig. 2.21).

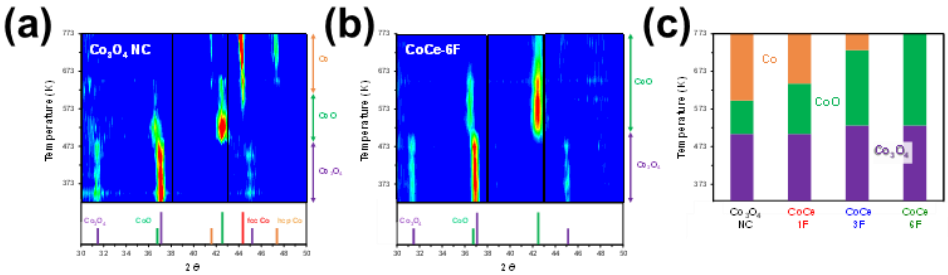

Figure 2.18. *in situ* XRD for the Co_3O_4-CeO_2 NCs. *In situ* XRD results for (a) Co_3O_4 NCs and (b) CoCe-6F in the CO environment at 323–773 K (the peak intensity increases moving from blue to red). (c) Change in the crystal phase from Co_3O_4 to CoO and Co as the reduction temperature increases during the XRD measurements. Each color represents the majority crystallographic phase at the specified temperature (violet: Co_3O_4, green: CoO, orange: Co).

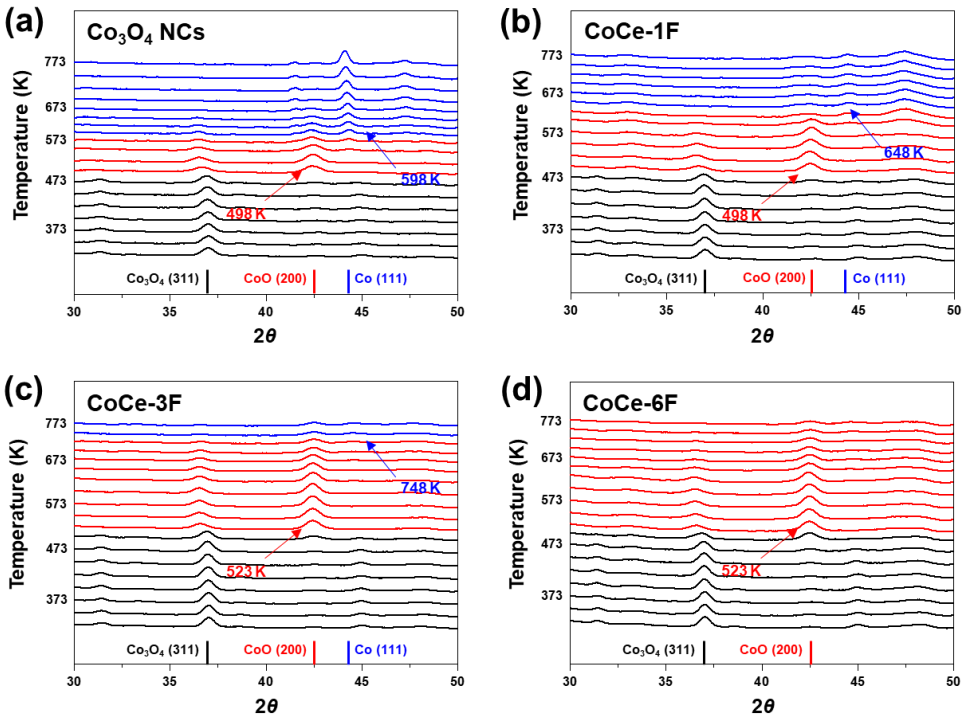

Figure 2.19. *In situ* XRD patterns of Co_3O_4-CeO_2 NCs in the temperature range of 323–773 K (25K increments) under 5% CO. (a) Co_3O_4, (b) CoCe-1F, (c) CoCe-3F, and (d) CoCe-6F. The main peaks of each cobalt phase are colored as red (Co_3O_4, JCPDS #42-1467), blue (CoO, JCPDS #43-1004), and green (Co, JCPDS #05-0727).

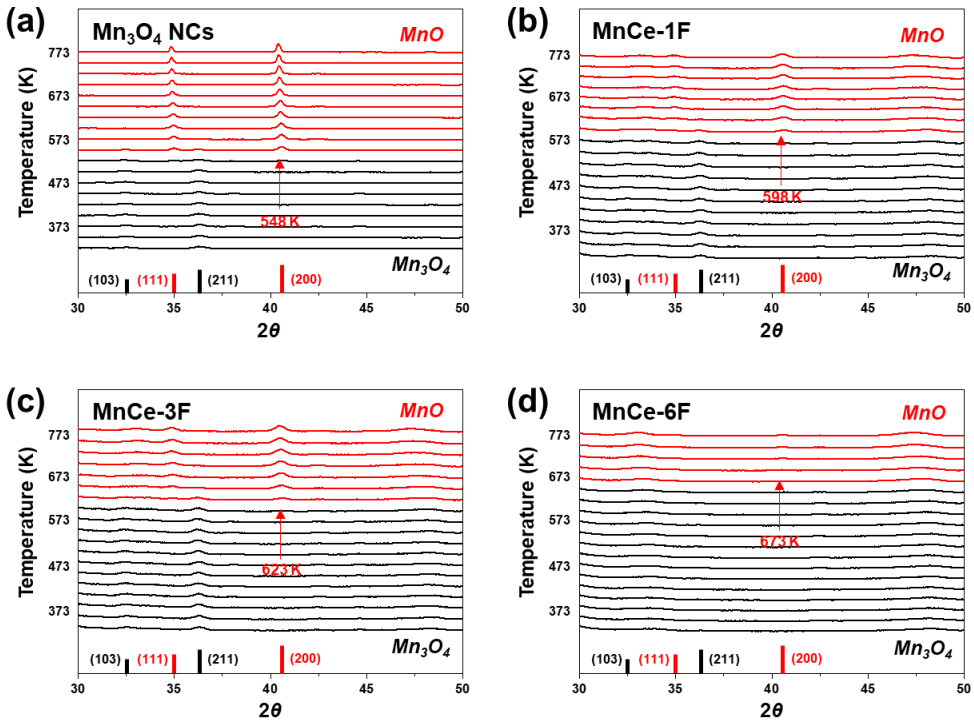

Figure 2.20. *In situ* XRD patterns of Mn_3O_4-CeO_2 NCs under 5% CO. (a) Mn_3O_4 NCs, (b) MnCe-1F, (c) MnCe-3F, and (d) MnCe-6F. Mn_3O_4 (black, JCPDS #80-0382) and MnO (red, JCPDS #07-0230).

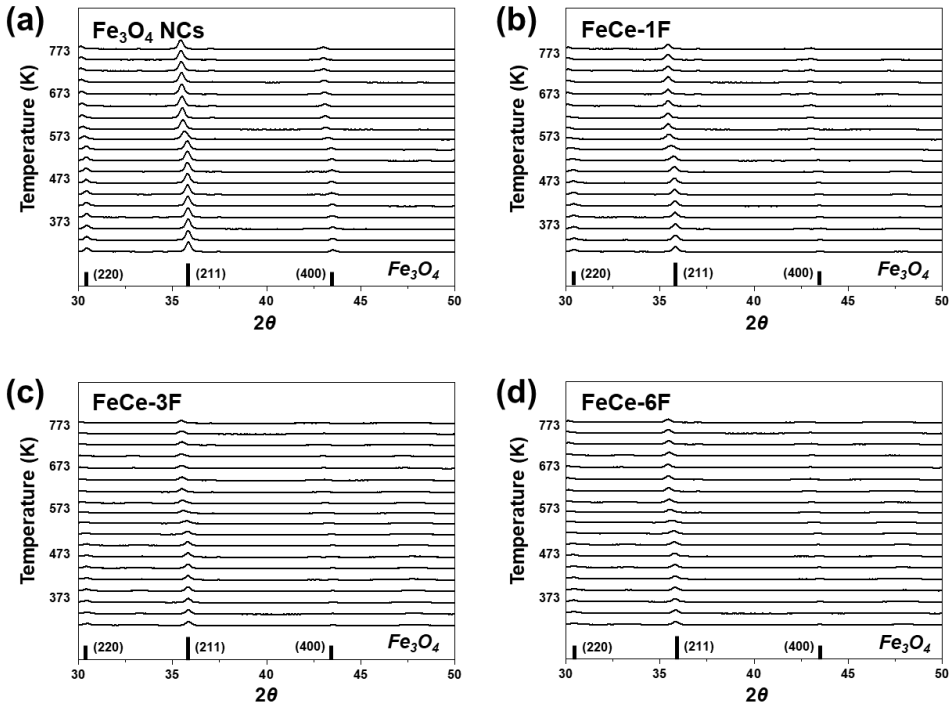

Figure 2.21. *In situ* XRD patterns of Fe_3O_4-CeO_2 NCs under 5% CO. (a) Fe_3O_4 NCs, (b) FeCe-1F, (c) FeCe-3F, and (d) FeCe-6F. Only Fe_3O_4 (JCPDS #65-3107) peaks are observed.

2.3.4. Changes in the Oxidation State under Different Reaction Environments.

An *in situ* XAS study was performed to investigate the surface properties of the Co_3O_4-CeO_2 NCs, which exhibited the most distinguishable phase change during *in situ* XRD observations in the reaction environment employed herein (Fig. 2.22a-c and 2.23). As shown in Fig. 2.22a and 2.22b, the reference peaks of Co and Co_3O_4 are clearly distinguished in the XANES profiles, where the Co_3O_4 oxidation state changes from Co^{2+}/Co^{3+} to Co^0 as the white-line intensity decreases; the energy decreases and the pre-edge peak is magnified. The *in situ* Co K-edge XANES profiles obtained after raising the temperature to 673 K under a 5% CO/He atmosphere show a significant difference in the oxidation state between the Co_3O_4 NCs and CoCe-6F. As the temperature increases in the case of the Co_3O_4 NCs, the oxidation state is easily transformed into metallic Co at 673 K. However, the oxidation state of cobalt in CoCe-6F is more robust than that of the Co_3O_4 NCs and is preserved even at high temperatures. The absorption edge shift (E_0) from the derivative as a function of the CeO_2 coverage on the Co_3O_4 NC is shown in Fig. 2.22c. Notably, *in situ* XANES results measured under the reaction conditions in which O_2 coexisted (5% CO and 5% O_2) showed no significant difference, even under high-temperature conditions (Fig. 2.24).

The Ce^{3+} ions provide the basis for the formation of oxygen vacancies on the CeO_2 surface due to the reduction of Ce^{4+} to Ce^{3+} and subsequent charge

transfer to the spinel oxide. As oxygen is supplied from the CeO_2 surface to the spinel oxide during catalytic oxidation, Ce is reduced from Ce^{4+} to Ce^{3+}. To observe the changes in the oxidation state in CeO_2, NAP-XPS measurements were carried out under 1 mbar of CO as a catalytically relevant reducing condition. Fig. 2.22d shows the Ce 3*d* spectra of CoCe-3F under oxygen deficient conditions at temperatures ranging from 373 to 673 K. As the temperature increases under CO-rich conditions, Ce is reduced from Ce^{4+} to Ce^{3+}, as confirmed by the change in the XPS peaks (highlighted with dash-lines for Ce^{3+}). In a CO oxidation environment at 473 K, the estimated proportion of Ce^{3+} ions calculated by peak deconvolution is the highest in CoCe-3F, as shown in Fig. 2.22e. In the partially covered Co_3O_4-CeO_2 NCs (CoCe-1F and CoCe-3F), Ce is more easily reduced from Ce^{4+} to Ce^{3+} compared to in the fully covered CoCe-6F (Fig. 2.25 and 26). A more obvious change in the Ce oxidation state of CoCe-3F indicates that the exposed active interface of CoCe-3F is larger than that of CoCe-6F, although the coverage of CeO_2 is higher in the case of CoCe-6F. The change in Ce^{3+} concentration as a function of temperature is summarized in Fig. 2.22f, where significant differences are highlighted at 473 and 573 K. The finding that the highest interfacial area is obtained for CoCe-3F is in good agreement with the CO oxidation results, where the highest TOF was observed for CoCe-3F. In addition, the Raman spectra show that the CeO_2 F_{2g} peak (~480 cm^{-1}) of CoCe-3F is broader and is blue-shifted relative to those of CoCe-1F and CoCe-6F, indicating the higher

oxygen vacancy content of CoCe-3F (Fig. 2.27).[43] These results show that CoCe-3F has a more optimized Co_3O_4-CeO_2 interface than CoCe-1F and CoCe-6F, which contain insufficient and excessive CeO_2 layers, respectively. Further experiments demonstrate that the Co_3O_4-CeO_2 NCs with a higher CeO_2 coverage beyond that of CoCe-6F exhibit particularly low CO oxidation activity because the active Co_3O_4 species is largely blocked (Fig. 2.28).

As the oxidation state in CeO_2 changes from Ce^{4+} to Ce^{3+}, oxygen vacancies are generated by oxygen transfer through the interface to prevent the reduction of the spinel oxide surface. This process is described well by the MvK mechanism in which the lattice oxygen participates in the catalytic reaction by transferring oxygen at the interface undergoing reversible reduction/oxidation.[44] Co_3O_4 is an active species for catalytic oxidation because Co_3O_4 NCs exhibit CO oxidation activity (Fig. 2.13a). Through the MvK mechanism, a reversible change in the oxidation state of the Co_3O_4 NCs enables oxygen migration for improved CO oxidation (Fig. 2.22g). When the spinel oxide-CeO_2 interface is created, CeO_2 further accelerates the oxygen transfer process. The high oxygen storage capacity and easy oxygen vacancy formation of CeO_2 leads to a reversible change of the Ce^{4+} ions to Ce^{3+} ions at the interface with the metal, enabling an enhancement in the oxidation reaction, even in reactant-deficient environments.

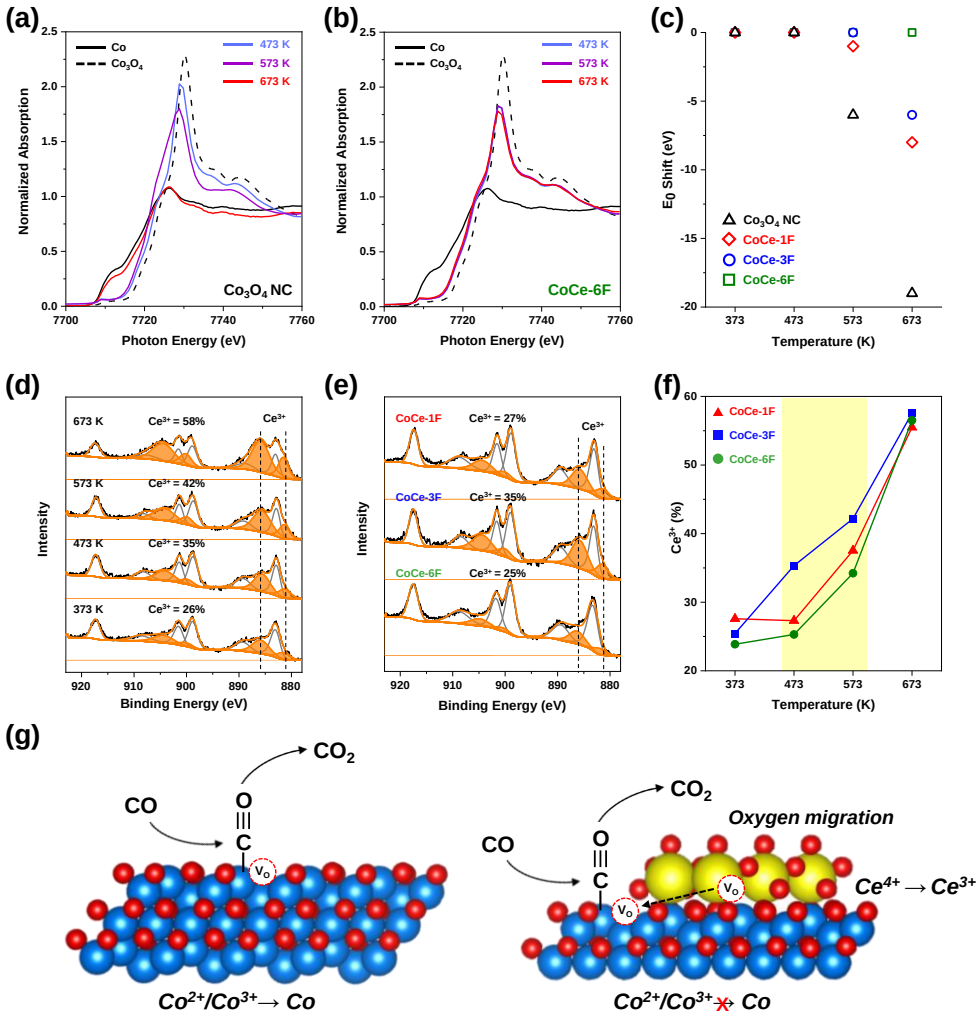

Figure 2.22. Oxidation state changes of the Co_3O_4-CeO_2 NCs observed from XANES and NAP-XPS analyses in different reaction environments. Co K-edge XANES profiles of (a) Co_3O_4 and (b) CoCe-6F NCs under a CO flow at 473, 573, and 673 K. (c) Comparison of the E_0 shift of each catalyst from the derivative. (d) Ce 3*d* NAP-XPS results for CoCe-3F in the CO environment at different temperatures. (e) Ce 3*d* NAP-XPS results for the Co_3O_4-CeO_2 NCs with a different CeO_2 coverage at 473 K. The Ce^{3+} fraction of each catalyst (orange) is calculated by peak deconvolution. (f)

Relative concentration of Ce^{3+} determined by NAP-XPS under different conditions. (g) CO oxidation governed by the Mars–van Krevelen (MvK) mechanism on Co_3O_4 and the Co_3O_4-CeO_2 NCs.

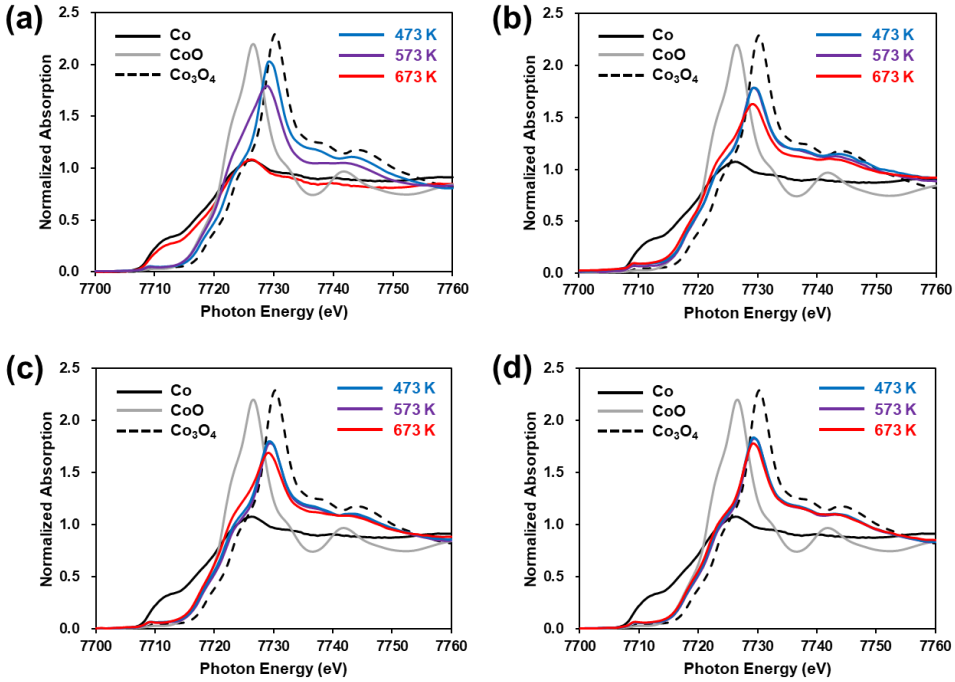

Figure 2.23. *In situ* Co K-edge XANES results obtained in a reducing environment for (a) the Co_3O_4 NCs, (b) CoCe-1F, (c) CoCe-3F, and (d) CoCe-6F under a 5% CO atmosphere (balanced with He) at 473–673 K.

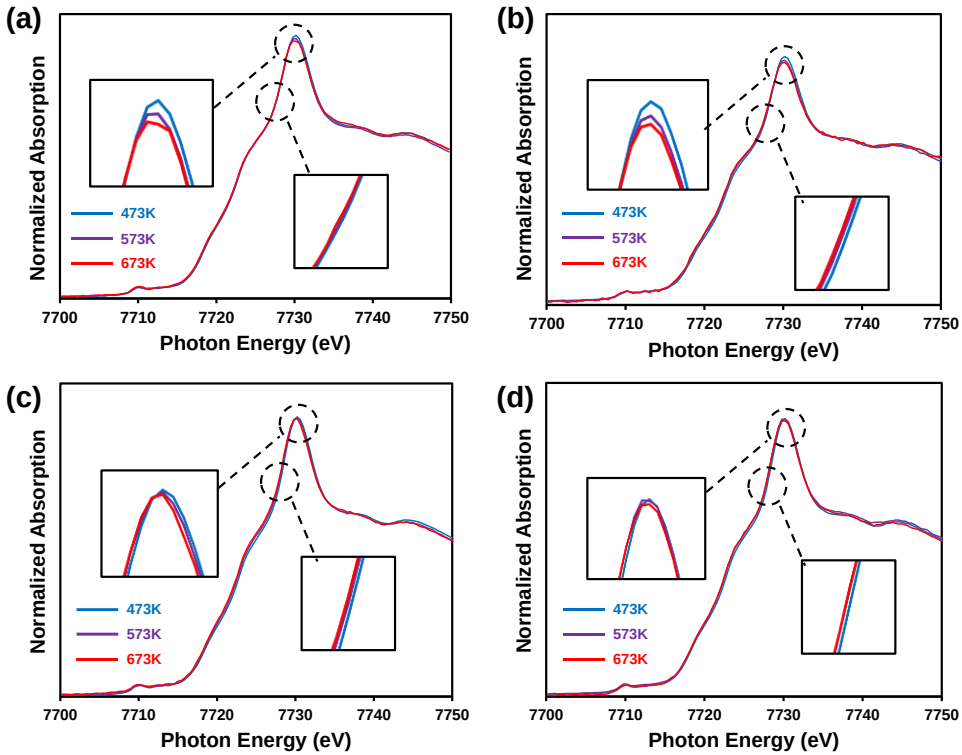

Figure 2.24. *In situ* Co K-edge XANES profiles of (a) Co_3O_4 NCs, (b) CoCe-1F, (c) CoCe-3F, and (d) CoCe-6F under a 5% CO and 5% O_2 flow from 473 to 673 K. Negligible changes are observed in the presence O_2 compared with those in CO alone.

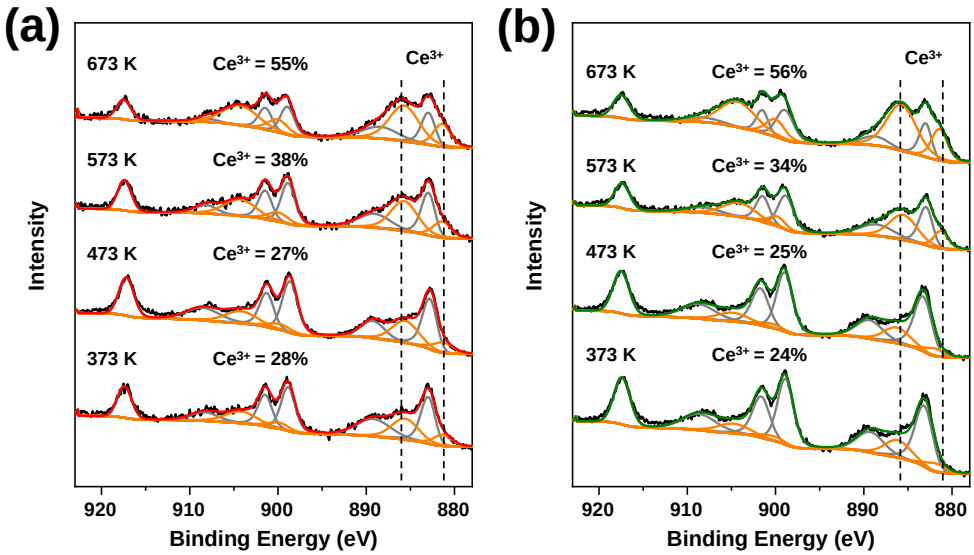

Figure 2.25. Near ambient pressure X-ray photoelectron spectroscopy (NAP-XPS) Ce 3*d* spectra in CO environment at different temperatures. (a) CoCe-1F and (b) CoCe-6F. The Ce^{3+} region by peak deconvolution is shown in orange and each Ce^{3+} ratio is presented. In all catalysts, as the temperature increases, the proportion of Ce^{3+} gradually increases.

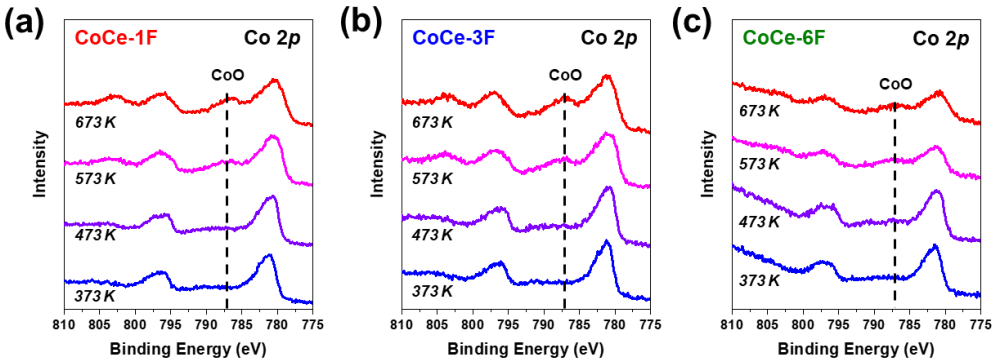

Figure 2.26. NAP-XPS Co 2*p* spectra in CO environment at different temperatures. (a) CoCe-1F, (b) CoCe-3F, and (c) CoCe-6F. As a result of *in situ* XANES, the degree of reduction of cobalt species in CoCe-1F and CoCe-3F was higher than that of CoCe-6F, demonstrating that the deposited CeO_2 prevents the reduction of Co_3O_4.

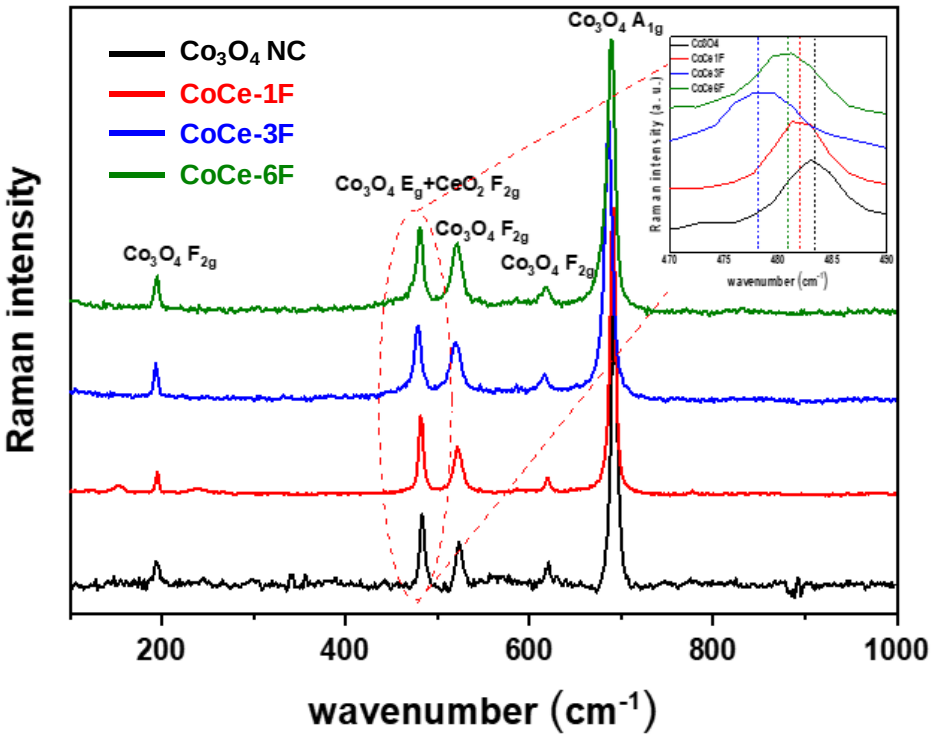

Figure 2.27. Raman spectra of Co_3O_4-CeO_2 NCs with the different CeO_2 coverage. Spectra were collected at 100–1200 cm^{-1} and highlighted at the range of 460–500 cm^{-1} (inset). The full width half maximum (FWHM) is the largest and the peak shift to lower wavenumber of CeO_2 F_{2g} symmetry peak in CoCe-3F indicates the highest formation of the oxygen vacancy.

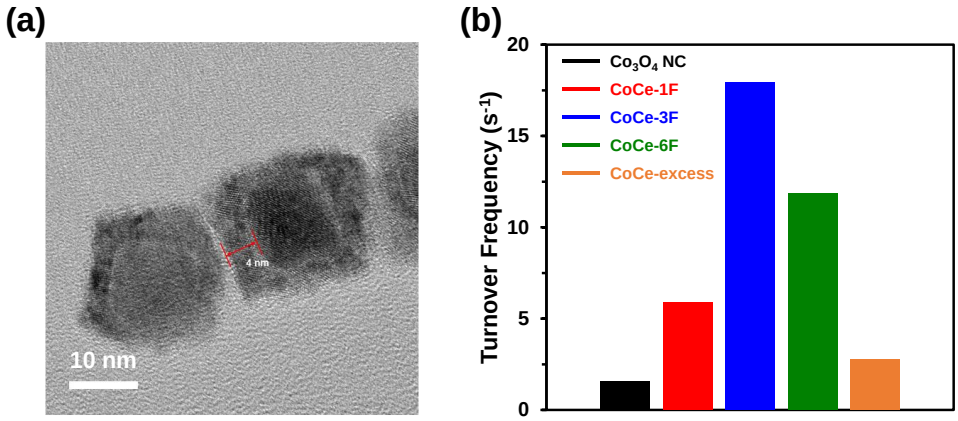

Figure 2.28. (a) TEM image of Co_3O_4 NCs overcoated by CeO_2 layers (CoCe-excess). The CoCe-excess catalyst possesses a 4-nm-thick CeO_2 shell. (b) TOFs for the CoCe catalyst series in the CO oxidation reaction with a CO/O_2 ratio of 1.0. The CoCe-excess catalyst exhibits a significantly lower TOF compared to the other Co_3O_4-CeO_2 NCs.

2.3.5. Hot Electron Detection at the Co_3O_4-CeO_2 Interface

To further confirm the occurrence of charge transfer at the interface during catalytic oxidation, the hot electron flow was measured using a catalytic nanodiode containing Co_3O_4-CeO_2 NCs as a representative example. Nonadiabatic energy dissipation at the interfaces during exothermic chemical reactions is known to result in the flow of energetic electrons of 1–3 eV, which are otherwise known as hot electrons, and are converted from chemical energy.[6,45] By correlating the amount of hot electrons generated during the catalytic reaction with TOF, the presence of charge transfer and its degree can be predicted. A scheme of the Au/TiO_2 nanodiode containing Co_3O_4-CeO_2 NCs and an energy band diagram showing the Schottky barrier are presented in Fig. 2.29a. The Co_3O_4-CeO_2 NC monolayer was deposited onto the Au/TiO_2 nanodiode, which was confirmed by SEM (Fig. 2.30), where the thickness of the Au layer (~10 nm) was lower than the electron mean free path (<15 nm).[46] The obtained current-voltage (*I*-*V*) curves of the nanodiode are shown in Fig. 2.31. The determined Schottky barrier by the fitting process was found to be 0.86–0.89 eV, indicating that the nanodiode does not significantly affect the intrinsic electronic properties. The hydrogen oxidation reaction ($H_2 + O_2 \rightarrow H_2O$) was carried out as an exothermic reaction to investigate the hot electron flow depending on the TOF of the Co_3O_4-CeO_2 NCs. Since H_2 oxidation operates at a relatively low temperature (323–403 K) compared to CO oxidation, the former is more suitable as a model reaction for hot

electron detection to rule out any thermal effect during the measurement.[6] The hot electron study based on the H_2 oxidation reaction further demonstrates that the interfacial effect is not limited to CO oxidation. Fig.2.29b shows the calculated H_2 oxidation TOF values of the Co_3O_4-CeO_2 NCs with different CeO_2 layers (313–363K). More specifically, the TOF order decreased as follows: CoCe-3F > CoCe-6F > CoCe-1F > Co_3O_4 NCs, which is identical to the trend observed for the CO oxidation results. The chemicurrent density of the nanodiode obtained at 313–403 K is shown in Fig 2.29c (inset: chemicurrent density at 313–363 K). As indicated, CoCe-3F exhibits the highest chemicurrent density resulting from the maximized charge transfer at the Co_3O_4-CeO_2 interface. The obtained TOFs and chemicurrent densities were then correlated and plotted in Fig. 2.29d. As shown, the TOF and chemicurrent density gradually increase as the CeO_2 coverage increases over the Co_3O_4 NCs. In the case of CoCe-3F, the values are maximum but subsequently decrease in the case of CoCe-6F due to the excessive coverage of the active Co_3O_4. Since the chemicurrent is proportional to the reaction rate (TOF), the chemicurrent yield represents the probability of a hot electron being present across the Schottky barrier.[47] The chemicurrent yield shown in Fig. 2.29e also demonstrates that the highest TOF of the CoCe-3F originated from the highest charge transfer at the Co_3O_4-CeO_2 interface.

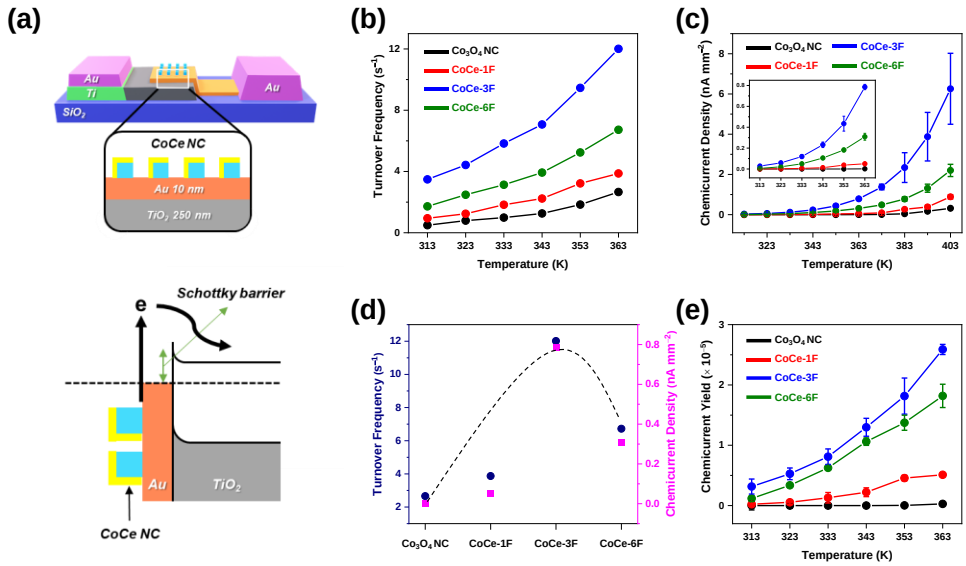

Figure 2.29. Hot electron detection at the Co_3O_4-CeO_2 interface. (a) Schematic illustration of an Au/TiO_2 nanodiode containing Co_3O_4-CeO_2 NCs and its energy band diagram. (b) TOFs for the H_2 oxidation reaction catalyzed by the Co_3O_4-CeO_2 NCs. (c) Chemicurrent density measurements at the Co_3O_4-CeO_2 interface (inset: the enlarged area at 313–363 K). (d) The relationship between the TOF and the chemicurrent depending on the type of Co_3O_4-CeO_2 interface. (e) Chemicurrent yield of the Co_3O_4-CeO_2 NCs as a function of temperature.

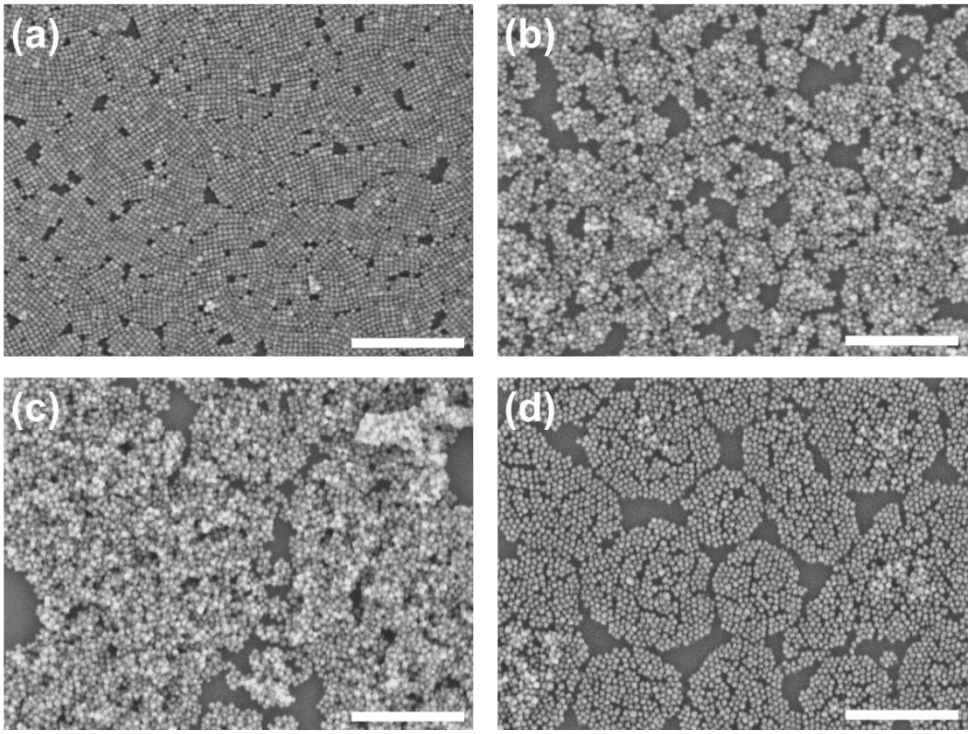

Figure 2.30. SEM images of the assembled Co_3O_4-CeO_2 NCs. (a) Co_3O_4 NCs, (b) CoCe-1F, (c) CoCe-3F, and (d) CoCe-6F. The scale bars represent 500 nm. TOFs of the H_2 oxidation were calculated based on the geometric dispersion of Co_3O_4-CeO_2 NCs.

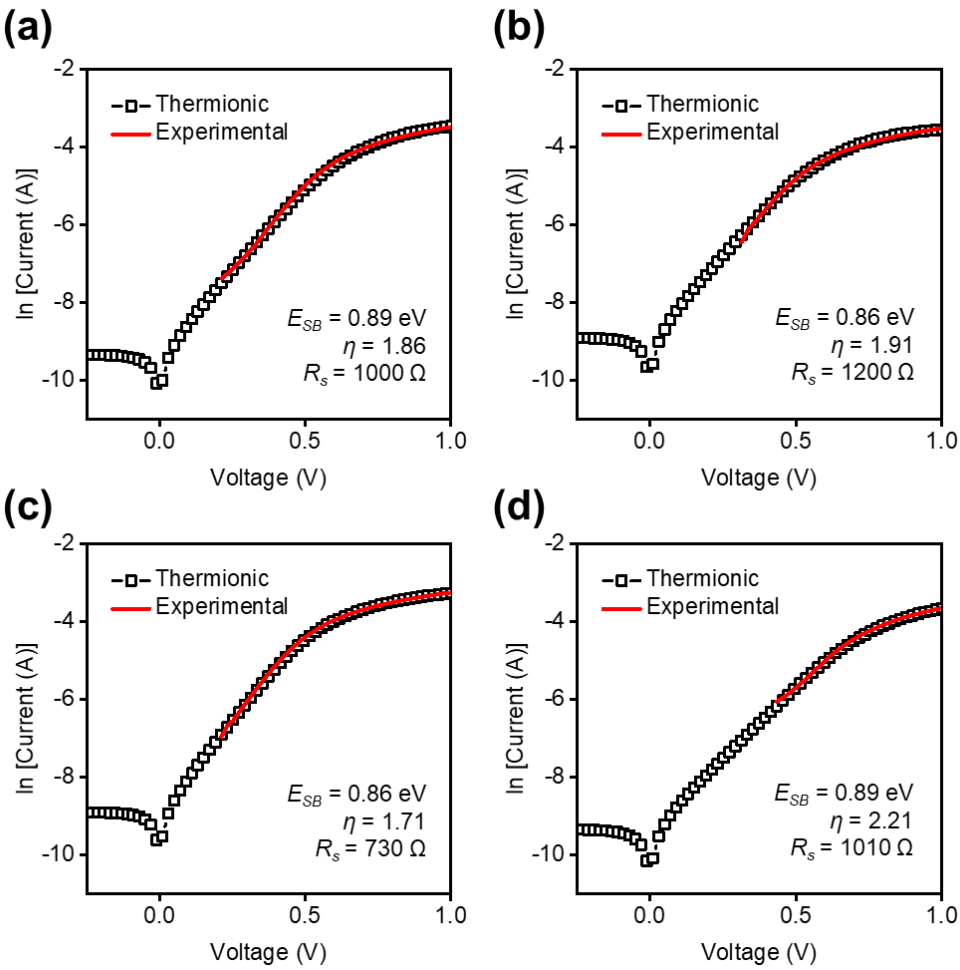

Figure 2.31. I-V characteristics of Co_3O_4-CeO_2 NCs loaded an Au/TiO_2 Schottky nanodiode. (a) Co_3O_4 NCs, (b) CoCe-1F, (c) CoCe-3F, and (d) CoCe-6F (all results were obtained under reaction gas conditions of H_2 15 Torr and O_2 745 Torr).

2.4. CONCLUSIONS

We synthesized spinel oxide NCs with controlled layers of CeO_2 by a selective deposition protocol. Co_3O_4, Mn_3O_4, and Fe_3O_4 NCs with 1, 3, and 6 facets covered by CeO_2 layers were prepared by controlling the surfactant concentration and pH. When CeO_2 was deposited on Co_3O_4 and Mn_3O_4 NCs, the TOFs achieved for the CO oxidation reaction were higher than those of the pristine NCs due to the interfacial effect. Various *in situ* characterization techniques revealed that the attached CeO_2 supplies oxygen to the Co_3O_4 surface, preventing it from being easily reduced under high-temperature reducing environments. The reduction of Ce^{4+} to Ce^{3+} and the subsequent charge transfer to Co_3O_4 were confirmed by NAP-XPS. The addition of CeO_2 layers was found to provide sufficient oxygen to the Co_3O_4 surface, resulting in a high TOF, which clearly demonstrates that the CO oxidation process occurred via the MvK mechanism. The Co_3O_4 NCs completely covered by CeO_2 (CoCe-6F) exhibited a lower TOF than that of CoCe-3F, demonstrating that the CO oxidation activity is directly related to the amount of the exposed Co_3O_4-CeO_2 interface. The same trend was observed for H_2 oxidation. Moreover, the charge transfer accelerated by the Co_3O_4-CeO_2 interface was also demonstrated by hot electron flow measurements during H_2 oxidation using a catalytic nanodiode. These in-depth studies using well-defined oxide nanostructures combined with *in situ* characterization have therefore provided insights to establishing the origin

of the activity enhancement and charge transfer at the interface.

** Parts of this chapter were published in the article, “Revealing Charge Transfer at the Interface of Spinel Oxide and Ceria during CO Oxidation.” (*ACS catalysis* **2021**, *11*, 1516-1527.)

2.5. References

[1] Somorjai, G. A., Li, Y. *Introduction of Surface Chemistry and Catalysis*, 2nd Edition; Wiley-VCH: New York, 2010.

[2] van Deelen, T.W.; Hernández Mejía, C.; de Jong, K.P. *Nat. Catal.* **2019**, *2*, 955–970.

[3] Li, Z.; Ji, S. F.; Liu, Y. W.; Cao, X.; Tian, S. B.; Chen, Y. J.; Niu, Z. G.; Li, Y. D. *Chem. Rev.* **2020**, *120*, 623–682.

[4] Xie, C. L.; Niu, Z. Q.; Kim, D.; Li, M. F.; Yang, P. D. *Chem. Rev.* **2020**, *120*, 1184–1249.

[5] Campbell, C. T. *Nat. Chem.* **2012**, *4*, 597–598.

[6] Park, J. Y.; Baker, L. R.; Somorjai, G. A. *Chem. Rev.* **2015**, *115*, 2781–2817.

[7] Karim, W.; Spreafico, C.; Kleibert, A.; Gobrecht, J.; VandeVondele, J.; Ekinci, Y.; van Bokhoven, J. A. *Nature* **2017**, *541*, 68–71.

[8] Rodriguez, J. A.; Ma, S.; Liu, P.; Hrbek, J.; Evans, J.; Perez, M. Activity of CeO_x and TiO_x *Science* **2007**, *318*, 1757–1760.

[9] Cargnello, M.; Doan-Nguyen, V. V. T.; Gordon, T. R.; Diaz, R. E.; Stach, E. A.; Gorte, R. J.; Fornasiero, P.; Murray, C. B. *Science* **2013**, *341*, 771–773.

[10] Yoon, S.; Oh, K.; Liu, F. D.; Seo, J. H.; Somorjai, G. A.; Lee, J. H.; An, K. *ACS Catal.* **2018**, *8*, 5391–5398.

[11] Montini, T.; Melchionna, M.; Monai, M.; Fornasiero, P. *Chem. Rev.*

2016, *116*, 5987–6041.

[12] Kim, H. Y.; Lee, H. M.; Henkelman, G. *J. Am. Chem. Soc.* **2012**, *134*, 1560–1570.

[13] Beniya, A.; Higashi, S. *Nat. Catal.* **2019**, *2*, 590–602.

[14] Wu, C. H.; Liu, C.; Su, D.; Xin, H. L.; Fang, H. T.; Eren, B.; Zhang, S.; Murray, C. B.; Salmeron, M. B. *Nat. Catal.* **2019**, *2*, 78–85.

[15] Carrettin, S.; Concepcion, P.; Corma, A.; Nieto, J. M. L.; Puntes, V. F. *Angew. Chem. Int. Edit.* **2004**, *43*, 2538–2540.

[16] Guzman, J.; Carrettin, S.; Corma, A. *J. Am. Chem. Soc.* **2005**, *127*, 3286–3287.

[17] An, K.; Alayoglu, S.; Musselwhite, N.; Plamthottam, S.; Melaet, G.; Lindeman, A. E.; Somorjai, G. A. *J. Am. Chem. Soc.* **2013**, *135*, 16689–16696.

[18] Xie, X. W.; Li, Y.; Liu, Z. Q.; Haruta, M.; Shen, W. J. *Nature* **2009**, *458*, 746–749.

[19] Xu, J.; Deng, Y. Q.; Zhang, X. M.; Luo, Y.; Mao, W.; Yang, X. J.; Ouyang, L.; Tian, P. F.; Han, Y. F. *ACS Catal.* **2014**, *4*, 4106–4115.

[20] Lukashuk, L.; Yigit, N.; Rameshan, R.; Kolar, E.; Teschner, D.; Havecker, M.; Knop-Gericke, A.; Schlogl, R.; Fottinger, K.; Rupprechter, G. *ACS Catal.* **2018**, *8*, 8630–8641.

[21] Jansson, J.; Palmqvist, A. E. C.; Fridell, E.; Skoglundh, M.; Osterlund, L.; Thormahlen, P.; Langer, V. *J. Catal.* **2002**, *211*, 387–397.

[22] Wang, H. F.; Kavanagh, R.; Guo, Y. L.; Guo, Y.; Lu, G. Z.; Hu, P. *J.*

Catal. **2012,** *296*, 110–119.

[23] Bae, J.; Shin, D.; Jeong, H.; Kim, B. S.; Han, J. W.; Lee, H. *ACS Catal.* **2019**, *9*, 10093–10100.

[24] Lukashuk, L.; Fottinger, K.; Kolar, E.; Rameshan, C.; Teschner, D.; Havecker, M.; Knop-Gericke, A.; Yigit, N.; Li, H.; McDermott, E.; Stoger-Pollach, M.; Rupprechter, G. *J. Catal.* **2016**, *344*, 1–15.

[25] Lundgren, E.; Zhang, C.; Merte, L. R.; Shipilin, M.; Blomberg, S.; Hejral, U.; Zhou, J. F.; Zetterberg, J.; Gustafson, J. *Acc. Chem. Res.* **2017**, *50*, 2326–2333.

[26] Voychok, D.; Guild, C. J.; Dissanayake, S.; Llorca, J.; Stavitski, E.; Liu, Z. Y.; Palomino, R. M.; Waluyo, I.; Li, Y. Y.; Frenkel, A. I.; Rodriguez, J. A.; Suib, S. L.; *J. Phys. Chem. C* **2018**, *122*, 8998–9008.

[27] Oh, M. H.; Cho, M. G.; Chung, D. Y.; Park, I.; Kwon, Y. P.; Ophus, C.; Kim, D.; Kim, M. G.; Jeong, B.; Gu, X. W.; Jo, J.; Yoo, J. M.; Hong, J.; McMains, S.; Kang, K.; Sung, Y. E.; Alivisatos, A. P.; Hyeon, T. *Nature* **2020**, *577*, 359–363.

[28] Oh, M. H.; Yu, T.; Yu, S. H.; Lim, B.; Ko, K. T.; Willinger, M. G.; Seo, D. H.; Kim, B. H.; Cho, M. G.; Park, J. H.; Kang, K.; Sung, Y. E.; Pinna, N.; Hyeon, T. *Science* **2013**, *340*, 964–968.

[29] Guardia, P.; Di Corato, R.; Lartigue, L.; Wilhelm, C.; Espinosa, A.; Garcia-Hernandez, M.; Gazeau, F.; Manna, L.; Pellegrino, T. *ACS Nano* **2012**, *6*, 3080–3091.

[30] Jia, H. L.; Du, A. X.; Zhang, H.; Yang, J. H.; Jiang, R. B.; Wang, J. F.;

Zhang, C. Y. *J. Am. Chem. Soc.* **2019**, *141*, 5083–5086.

[31] Banfield, J. F.; Welch, S. A.; Zhang, H. Z.; Ebert, T. T.; Penn, R. L. *Science* **2000**, *289*, 751–754.

[32] Zhu, G. X.; Yao, S. S.; Zha, H. L.; Liu, Z. M.; Li, Y. L.; Pan, H. H.; Tang, R. K. *Langmuir* **2016**, *32*, 8999–9004.

[33] Yang, S. W.; Gao, L. *J. Am. Chem. Soc.* **2006**, *128*, 9330–9331.

[34] Zhang, J. T.; Tang, Y.; Lee, K.; Min, O. Y. *Science* **2010**, *327*, 1634–1638.

[35] Pope, E. J. A.; Mackenzie, J. D. *J. Non-Cryst. Solids* **1986**, *87*, 185–198.

[36] Brinker, C. J.; Scherrer, G. W. *Sol-Gel Science: The physics and Chemistry of Sol-Gel Process*; Academic Press, New York, 1990.

[37] Jolivet, J. P. *Metal Oxide Chemistry and Synthesis: From Solution to Solid State*; Wiley, Chichester, U. K., 2000.

[38] Yamada, Y.; Tsung, C. K.; Huang, W.; Huo, Z. Y.; Habas, S. E.; Soejima, T.; Aliaga, C. E.; Somorjai, G. A.; Yang, P. D. *Nat. Chem.* **2011**, *3*, 372–376.

[39] Baker, L. R.; Kennedy, G.; Van Spronsen, M.; Hervier, A.; Cai, X. J.; Chen, S. Y.; Wang, L. W.; Somorjai, G. A. *J. Am. Chem. Soc.* **2012**, *134*, 14208–14216.

[40] Ha, H.; An, H.; Yoo, M.; Lee, J.; Kim, H. Y. *J. Phys. Chem. C* **2017**, *121*, 26895–26902.

[41] Ha, H.; Yoon, S.; An, K.; Kim, H. Y. *ACS Catal.* **2018**, *8*, 11491–11501.

[42] Jampaiahab, D.; Velisojuc, V. K.; Devaiahd, D.; Singhb, M.; Mayese, E. L. M.; Coylea, V. E.; Reddyc, B. M.; Bansalb, V.; Bhargava, S. K. *Appl. Surf.*

Sci. **2019**, *473*, 209–221.

[43] Lee, Y.; He, G. H.; Akey, A. J.; Si, R.; Flytzani-Stephanopoulos, M.; Herman, I. P. *J. Am. Chem. Soc.* **2011**, *133*, 12952–12955.

[44] Chen, X.; Mao, S. S. *Chem. Rev.* **2007**, *107*, 2891–2959.

[45] Park, J. Y.; Kim, S. M.; Lee, H.; Nedrygailov, I. I. *Acc. Chem. Res.* **2015**, *48*, 2475–2483.

[46] Lee, H.; Nedrygailov, I. I.; Lee, C.; Somorjai, G. A.; Park, J. Y. *Angew. Chem. Int. Edit.* **2015**, *54*, 2340–2344.

[47] Lee, H.; Lim, J.; Lee, C.; Back, S.; An, K.; Shin, J. W.; Ryoo, R.; Jung, Y.; Park, J. Y. *Nat. Commun.* **2018**, *9*, 1–8.

[48] Ravel, B.; Newville, M. *J. Synchrotron Radiat.* **2005**, *12*, 537–541.

Chapter 3. Facet-Defined Strain-Free Spinel Oxide for Oxygen Reduction

3.1. Introduction

Facet and strain engineering of nanocatalysts, which modulates surface atomic and electronic structures, can effectively control the performance by modifying both thermodynamic and kinetic parameters.[1-3] For instance, platinum-group-metal (PGM)-based nanocatalysts are designed to selectively expose specific facets (e.g. (111) and (100)),[4] and a strong correlation is established between atomic structure of each facet and catalytic activities.[5-7] However, in multimetallic nanomaterials, controlling the exposing facet with various compositions is challenging due to different surface energies of two or more distinct materials.[8,9]

The epitaxial growth on a well-defined template may allow the desired facet to be exposed dominantly.[10-12] Core-shell type nanocrystals which expose specific facets according to their template core exhibit high catalytic performance because of selective exposure of active atomic arrangement even with multimetallic surfaces.[13,14] In that, strains at the interface of heterostructure can affect the catalytic activity by altering the surface structure, with which reaction intermediates interact.[15,16] Biaxially strained surfaces due to the lattice mismatch with core materials were used for the development of several highly active PGM-based catalysts for electrocatalytic reactions.[17-19] Therefore, to observe the composition-

dependent catalytic activities in controlled environment on defined facets, the strain needs to be minimized.

Recently, several earth-abundant spinel oxides (AB_2O_4), which can substitute PGM-based materials for oxygen electrocatalysis, are epitaxially combined in core-shell nanocrystals due to their similar crystallographic structures.[20-21] The controllable structure, composition, and valence state of spinel oxides provide rich opportunities to improve functional properties through material engineering.[22-24] In particular, the role of crystal and electronic structures of Co-Mn spinel oxides in optimizing the electrocatalytic oxygen reduction reaction (ORR) activity is investigated both experimentally and computationally.[25-27] Unfortunately, the use of ill-defined surface facets of irregularly shaped spinel nanocrystals with various defects in the experiment and well-defined facets without defects in the calculations leads to severe discrepancies in their results.[26,28] Furthermore, because of the Jahn-Teller (J-T) distortion in octahedral Mn^{3+}, Co-Mn spinel oxides possess different phase-dependent properties according to Mn/Co ratio such as surface strain, atomic arrangement, and resulting catalytic activities even on the same facet.[25,27] Therefore, new strategy to minimize the effect of J-T distortion with controlling the strain on defined facet is needed for systematic analysis of composition-activity relationship.[29]

In this work, spinel Co_3O_4@$Co_yMn_{1-y}O_x$ ($x \sim 4/3$ and $0<y<1$) core-shell nanocubes exposing (001) facets are synthesized using epitaxial growth with different Mn/Co compositions at the surface. We have employed a

composition gradient design, which has been extensively used in the synthesis of highly luminescent quantum dots for display applications to reduce the strain originated defects,[30-32] to minimize the surface strain and the effect of J-T distortion during the epitaxial growth of the $Co_yMn_{1-y}O_x$ shell. The resulting (001) facet-defined oxide surface with strain-free $Co_yMn_{1-y}O_x$ shell enables us to investigate a composition-activity correlation between the Mn/Co content of the surface and model electrocatalytic ORR activity without facet and strain related factors. Furthermore, density functional theory (DFT) calculations on (001) facet of Co-Mn spinel oxides validate the accordance between calculational and experimental results by using our well-defined model nanostructures.

3.2. Experimental Section

3.2.1. Synthesis of template spinel oxide nanocubes

Co_3O_4 nanocubes were synthesized following the previous report.[21] $Co(ClO_4)_2$ (1 mmol, Sigma-Aldrich) and oleylamine (10 mmol, 70%, Sigma-Aldrich) were dissolved in 15 ml of 1-octanol (99%, Samchun chemicals). The mixture was heated to 393 K in air and 0.7 ml of distilled water was injected during the heating. Then, the reaction mixture was stirred at 393 K for 2 h. The synthesized nanocrystals were washed with ethanol/hexane and retrieved with centrifugation.

For Mn_3O_4 nanocubes, $Mn(CH_3COO)_2$ (1 mmol, 98%, Sigma-Aldrich), oleylamine (5 mmol), and oleic acid (1 mmol, 90%, Sigma-Aldrich) were mixed with 15 ml of xylenes (≥75%, Sigma-Aldrich). The mixture was heated up to 363 K and 0.8 ml of distilled water was injected at that temperature. The reaction solution was maintained at 363 K for 1.5 h. The synthesized nanocrystals were washed with ethanol/hexane and retrieved with centrifugation.

3.2.2. Synthesis of Co_3O_4@$Co_yMn_{1-y}O_x$ and Mn_3O_4@$Co_yMn_{1-y}O_x$ core-shell nanocubes

The core-shell nanocrystals were prepared using as-synthesized spinel oxide as template. For Co_3O_4@$Co_yMn_{1-y}O_x$, 80 mg of Co_3O_4 nanocubes were dispersed in the mixture 5 mmol of oleylamine, 1 mmol of HCl (35.0 ~ 37.0%, Samchun Chemicals) and 15 ml of *o*-xylene (98.5%, Junsei). The

reaction mixture was pre-heated to 333 K for 30 min and further heated to 363 K under magnetic stirring. At the temperature, 3 ml of as-prepared metal formate aqueous solution with different Mn/Co ratio was injected. For example, the solution of 0.5 mmol of $Mn(HCOO)_2$ (Sigma-Aldrich) and 0.5 mmol of $Co(HCOO)_2$ (96%, Alfa-Aesar) in 3 ml of H_2O was injected in the reaction solution for $Co_{0.5}Mn_{0.5}$ nanocubes. After the injection, the reaction mixture was maintained at 363 K for 1.5 h. The resulting nanocrystals were washed with ethanol/hexane and retrieved by centrifugation.

For $Mn_3O_4@Co_yMn_{1-y}O_x$, 76 mg of Mn_3O_4 nanocubes were dispersed in the same mixture that was used for $Co_3O_4@Co_yMn_{1-y}O_x$ and the following procedures are the same.

3.2.3. Synthesis of $Co_3O_4@Mn_3O_4$ core-shell nanocrystals

The core-shell nanocrystals were synthesized following the reported method.[21] 80 mg of Co_3O_4 was dispersed in the mixture of 5 mmol of oleylamine, 3 mmol of HCl, and 15 ml of *o*-xylene. The reaction mixture was pre-heated to 333 K for 30 min and further heated to 363 K under magnetic stirring. At the temperature, 3 ml of 0.33 M $Mn(HCOO)_2$ aqueous solution was injected. After the injection, the reaction mixture was maintained at 363 K for 1.5 h. The resulting nanocrystals were washed with ethanol/hexane and retrieved by centrifugation.

3.2.4. Characterizations

TEM and EFTEM measurements were performed using the JEM-2100F (JEOL) instruments with an acceleration voltage of 200 kV. HAADF-STEM,

the corresponding EDS mapping measurements, and EELS line scan were conducted using the JEM-ARM200F operated at 200kV (Cold Field Emission Type, JEOL) in National Center for Inter-university Research Facilities, Seoul National University. For image recording and processing, FIJI, GPA Phase, and digital micrograph software were used. The atomic position peaking was conducted using STATSTEM software.[35] First, the drift corrected STEM image is filtered from its fast Fourier transformation (FFT) pattern by picking {100} diffraction spots to get the cation position at octahedral-sites. After converting the filtered FFT pattern to inverse FFT image, only octahedral-site cations appear in the image. The atomic positions of cations are picked and fitted with Gaussian function to get the real atomic position. Powder XRD patterns were obtained using a Rigaku D/max 2500 diffractometer (Rigaku, Japan) equipped with a rotating anode and a Cu K Kα radiation source (λ = 0.15418 nm). Raman spectra were recorded using A LabRAM HR Evolution (Horiba) with laser excitation at 532 nm, equipped at Research Institute of Advanced Material (RIAM) at Seoul National University (SNU). FT-IR spectra were obtained from FT-IR Vertex 70V (Horiba) from 250 to 4000 cm^{-1}. XPS measurement was conducted using the K-Alpha+ XPS system (Thermo Fisher Scientific) equipped at the Busan Center of the Korea Basic Science Institute (KBSI). The X-ray source was 1,486.6 eV monochromated Al Kα (X-ray energy of 12 kV, 72 W), the spot size was 400 μm, photoemission angle was 30°, and average depth of analysis was ~5 nm for silicon oxide. The XPS peaks

deconvolution was done using XPS peak 4.1 software. X-ray absorption spectroscopy was performed with 10 C beamline in Pohang Accelerator Laboratory (PAL). The obtained spectra were processed through Demeter software.[51] The Fourier transformation of EXAFS was done in a range of 3-11 Å $^{-1}$ with a Hanning window applied at 1-3 Å.

3.2.5. Electrochemical characterization

Electrochemical characterization was conducted in three-electrode configuration with Autolab PGSTAT302N potentiostat. In-house made fluorinated ethylene propylene cell was used for all electrochemical measurements. To avoid possible impurities from the electrochemical cell, the cell was cleaned by immersion in 0.5 M H_2SO_4 and multiple boiling in DI water (Millipore Mill-Q, 18.2 MΩ·cm, < 5 ppb TOC). Glassy carbon disk in rotating ring-disk electrode (RRDE, Pine Research, disk diameter = 5.6 mm) was used as working electrode substrate. Ag/AgCl (BASi , RE-6) and graphite rod (Alfa Aesar , 99.9995%) were used as reference and counter electrodes, respectively. The catalysts were prepared by deposition of as-synthesized nanocrystals on Vulcan XC-72 carbon support. 20 mg of as-synthesized nanocrystals and 40 mg of carbon support were mixed in 10 ml of chloroform with 2 h of ultrasonication. The catalysts were dried under vacuum and ligand was removed under air at 200 ^{o}C for 2 h. For electrochemical measurement, catalyst inks were made by ultrasonicating 10 mg of catalyst powder in 2 ml of DI water-isopropanol mixture (1:1 volume ratio), followed by addition of 60 μl of Nafion ionomer (Sigma-Aldrich, 5

wt%). For electrocatalyst thin-film deposition, the catalyst ink was pipetted and drop-casted onto the glassy carbon for 0.1 mg_{oxide} cm^{-2} of catalyst loading. For cyclic voltammetry, the catalyst film was immersed into Ar-saturated 1 M KOH electrolyte (Sigma-Aldrich, 99.995%,), and polarized between 0.4 and 1.2 V (vs. RHE) at scan rate of 20 mV s^{-1}. ORR measurement was conducted by polarizing the catalyst film between 0.4 and 1.1 V (vs. RHE) in O_2-saturated 1 M KOH electrolyte at scan rate of 20 mV s^{-1} and rotation speed of 1600 rpm. *iR*-correction was applied to all ORR measurements with 85% of ohmic resistance values measured from electrochemical impedance spectroscopy (E = 0.85 V, frequency range from 10 kHz to 1 Hz, potential amplitude of 10 mV). ORR polarization curve was plotted after subtracting background CV from Ar-saturated electrolyte. Onset potential value is defined at which current density reaches 5% of mass transfer-limited ORR current density. ORR kinetic current (at 0.9 V vs. RHE) was calculated from Koutecky-Levich equation and normalized to oxide mass loading to obtain ORR mass activity. Chronoamperometry was measured by holding electrode potential at 0.8 V (vs. RHE) and rotating it at a rate of 800 rpm in O_2-saturated 1 M KOH. All the electrochemical data were calibrated to RHE scale by measuring equilibrium potential on polycrystalline Pt electrode with the Ag/AgCl reference electrode in H_2-saturated 1 M KOH electrolyte.

3.2.6. Computational Details

Spin-polarized periodic density-functional theory (DFT) calculations were

performed using the generalized gradient approximation Perdew-Burke-Ernzerhof (GGA-PBE) exchange-correlation functional[52] and projector augmented wave (PAW) pseudopotential[53] as implemented in Vienna Ab initio Simulation Package (VASP, version 5.4.4.).[54] Convergence tolerances for energy and force were set to 10^{-4} eV and 0.05 eV/ Å, respectively, and kinetic energy cutoff was set to 500 eV (400 eV) for bulk (slab) structures. Monkhorst-Pack k-point[55] was set to $3 \times 3 \times 3$ ($3 \times 3 \times 1$) for bulk (slab) cubic structures and $4 \times 4 \times 3$ ($4 \times 2 \times 1$) for bulk (slab) tetragonal structures. To take into account strong on-site Coulombic interactions of localized *d*-electrons, Hubbard *U* correction scheme suggested by Dudarev et. al.[56] was applied with effective values U_{eff} $(U - J)$ of 3.32 eV and 3.90 eV for Co and Mn, respectively.

The theoretical limiting potentials for ORR were calculated following the associative mechanism,[57] which has been applied to various classes of catalysts, *i.e.*, $* + O_2 \rightarrow OOH^* \rightarrow O^* + H_2O \rightarrow OH^* \rightarrow * + H_2O$ with each step involving a protonation. Free energies of each reaction were calculated using the computational hydrogen electrode (CHE) method, which assumes an equilibrium between $\frac{1}{2}H_2$ (g) and (H^++e^-) at 0 V_{RHE} and standard conditions. The effect of the applied potential (*U*) was included to estimate the free energy of the proton-electron pair, i.e., $G(H^+ + e^-) = \frac{1}{2}G(H_2) - eU$. Zero-point energy, enthalpic and entropic corrections were calculated using the Harmonic (Ideal gas) approximation for adsorbates (gaseous molecules)

as implemented in Atomic Simulation Environment (ASE, Table 3.1).[58]

3.2.7. Computational Models of Spinel Oxides

To computationally predict ORR catalytic activity, we modelled various crystal structures and lattices of spinel oxides to consider various possibilities depending on the Mn/Co ratio. As Co_3O_4 and Mn_3O_4 prefer different spinel structures (cubic and tetragonal, respectively), we initially collected their bulk structures from Materials Project (cubic spinel Co_3O_4: "mp-18748", tetragonal spinel Mn_3O_4: "mp-18759") and relaxed them. In addition, to simulate mixed spinel structures, we also optimized tetragonal spinel Co_3O_4 ("mp-1285798") and cubic spinel Mn_3O_4, which were then used for the interpolation (Fig. 3.1a). In all cases, Co atoms are placed at the bottom since Mn prefers surface sites as confirmed by the experiments and DFT calculations. We modelled four-layered (001) surfaces with 8 formula units and 20 Å of a vacuum layer was added in *z*-direction to avoid imaginary interactions between repeating images (Fig. 3.1b). The computational models used for various Mn/Co ratio are described in the following:

(i) $Co_{1-x}Mn_x$ (x=0.08, 0.25, 0.50)

The experimentally determined *c/a* ratio changes as Mn/Co ratio increases up to x=0.50, indicating that the crystal structure changes as well (Table 3.2). Thus, we modelled both cubic and tetragonal spinel structures with the interpolated lattice parameters (Vegard's law), where the lattice parameters of pure spinel structures (Co_3O_4 and Mn_3O_4) and Mn/Co ratio were used for

the interpolation (Table 3.3).

(ii) $Co_{1-x}Mn_x$ (x=0.50, 0.75, 0.92)

We modelled the tetragonal spinel structure and lattices of Mn_3O_4 for x=0.50, 0.75, 0.92, where the experimental *c/a* does not change, and its value (1.64) is very close to the simulated one (1.63) of the tetragonal Mn_3O_4 (Table 3.1 and 3.3).

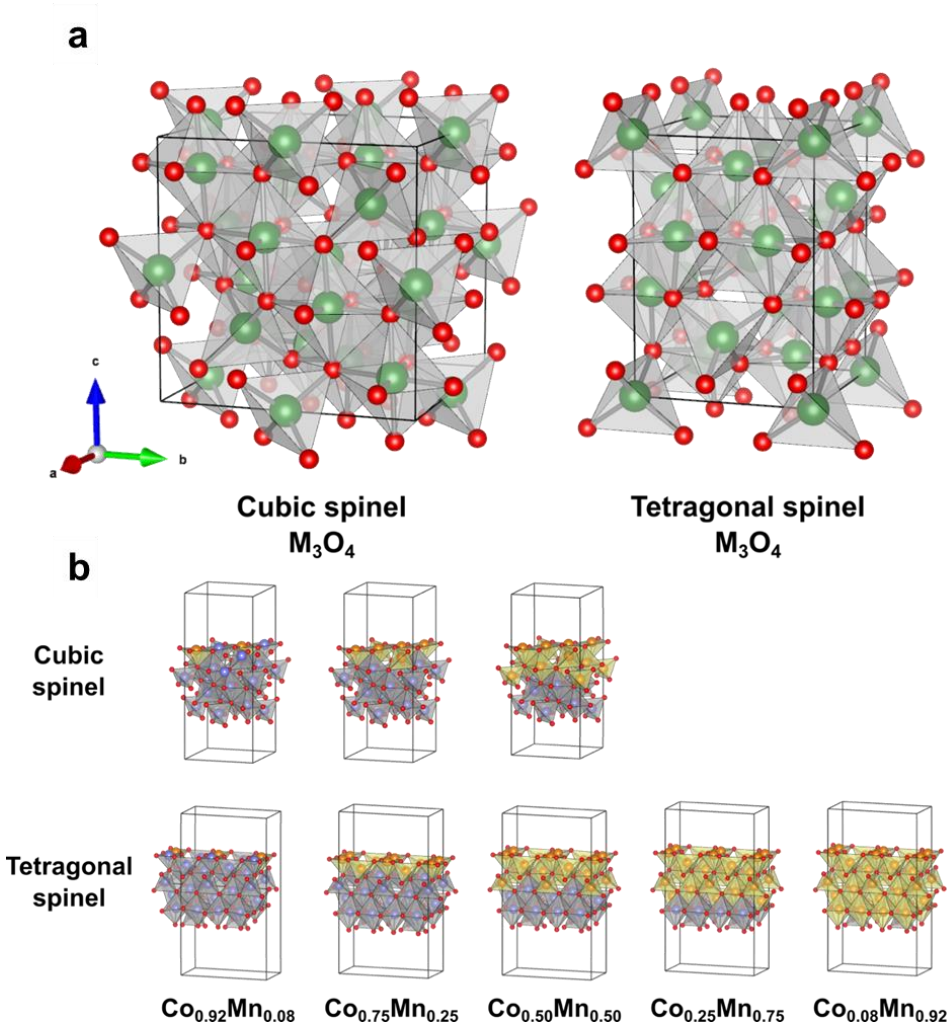

Figure 3.1. Models for DFT calculation (a) M_3O_4 (M = Co, Mn) cubic and tetragonal spinel bulk structures. Color codes: green (M) and red (O). (b) Four-layered mixed spinel surfaces for each Mn/Co ratio. Gray-polyhedral and blue balls correspond to Co, while yellow-polyhedral and orange balls corrspond to Mn.

Table 3.1. Free energy correction values for adsorbates and gaseous molecules. For H_2 and H_2O, partial pressures were set to 101,325 and 3,534 Pa, respectively. We note that gas-phase water at the saturated vapor pressure, 3,534 Pa, is in equilibrium with liquid water.[59]

	ZPE	$\int C_p\, dT$	*-TS*	Sum
		Adsorbates		
*O	0.05	0.04	-0.07	0.02
*OH	0.35	0.05	-0.09	0.32
*OOH	0.43	0.05	-0.09	0.39
		Molecules		
H_2	0.27	0.09	-0.40	-0.05
H_2O	0.57	0.11	-0.69	-0.01

Table 3.2. The experimentally determined lattice parameters and *c/a* values for various Mn/Co ratio.

	a	*c*	*c/a*
$Co_{0.90}Mn_{0.10}$	5.73	8.54	1.49
$Co_{0.75}Mn_{0.25}$	5.75	8.99	1.56
$Co_{0.50}Mn_{0.50}$	5.77	9.44	1.64
$Co_{0.25}Mn_{0.75}$	5.77	9.44	1.64
$Co_{0.10}Mn_{0.90}$	5.77	9.44	1.64

Table 3.3. The interpolated lattice parameters and *c/a* values for various Mn/Co ratio. The lattice parameters of pure spinel structures (Mn_3O_4, Co_3O_4) were used for the interpolation based on Mn/Co ratio (Vegard's law).

	Cubic spinel structures			Tetragonal spinel structures		
	a	*c*	*c/a*	*a*	*c*	*c/a*
$Co_{1.00}$	8.17	8.17	1.00	5.76	8.12	1.41
$Co_{0.92}Mn_{0.08}$	8.22	8.22	1.00	5.77	8.24	1.43
$Co_{0.75}Mn_{0.25}$	8.30	8.30	1.00	5.79	8.49	1.47
$Co_{0.50}Mn_{0.50}$	8.44	8.44	1.00	5.82	8.85	1.52
$Co_{0.25}Mn_{0.75}$	8.57	8.57	1.00	5.85	9.21	1.57
$Co_{0.08}Mn_{0.92}$	8.66	8.66	1.00	5.87	9.46	1.61
$Mn_{1.00}$	8.70	8.70	1.00	5.88	9.57	1.63

3.3. Results and Discussions

3.3.1 Structural characterization of spinel Co_3O_4@$Co_yMn_{1-y}O_x$ core-shell nanocubes

Spinel $Co_yMn_{1-y}O_x$ shell is deposited on the ~11 nm-sized Co_3O_4 nanocubes enclosed by (001) facets (Fig. 3.2) in an organic/aqueous reverse micelle solution. Co_3O_4 nanocubes are used to direct the exposing facet and phase of spinel $Co_yMn_{1-y}O_x$ surface. $Mn(HCOO)_2$ and $Co(HCOO)_2$ aqueous solutions are simultaneously injected, wherein formate anions slow down the precipitation rate of Mn/Co for epitaxial growth on the Co_3O_4 template. Similar to the growth of Mn_3O_4 on Co_3O_4 nanocubes in the recent study,[21] flat $Co_yMn_{1-y}O_x$ grains with similar spinel structure are epitaxially grown in <001> directions perpendicular to Co_3O_4 {100} surface plane. The slow deposition rate of Mn/Co on Co_3O_4 template makes $Co_yMn_{1-y}O_x$ oxide with high Co content deposited first due to the similar structure with the core. Then, the Mn/Co precursor ratio in the reaction solution is increased, the $Co_yMn_{1-y}O_x$ with higher Mn content can be deposited. Finally, several layers of $Co_yMn_{1-y}O_x$ with different Mn/Co ratios are deposited on the Co_3O_4 nanocube template with increasing Mn content from the core to the surface. Because of the layer-by-layer deposition of $Co_yMn_{1-y}O_x$ layers with slightly different Mn/Co ratios, the lattice strain from the discrepancy between the lattice distances of neighboring phases is minimized. Also, the shear strain, which can be found at the corner grain boundary of Co_3O_4@Mn_3O_4

nanocrystal, is also minimized owing to the small difference in aspect ratio of unit cell between the layers.[21] (Fig. 3.3a). The synthesized Co_3O_4@$Co_yMn_{1-y}O_x$ (Mn/Co = 1:1) nanocubes possess a cubic morphology with the overall size of ~15 nm and ~2-nm-thick shell (Fig. 3.3b). The lattice lines of the $Co_yMn_{1-y}O_x$ shell and Co_3O_4 core in the high-angle annular dark-field scanning transmission electron microscopy (HAADF-STEM) image are continuous due to their epitaxial growth onto flat surfaces. Shockley partial dislocation, stacking fault, and twinned disclination from the large strain are hardly observed.[33,34] Also, the gap generated from the tetragonal symmetry of $Co_yMn_{1-y}O_x$, which is the evidence for large shear strain, was minimized to less than 1° due to the composition gradient (red lines in Fig. 3.3b). Because of the varying Mn/Co composition from the core to the surface, the lattice fringe would gradually change according to the Mn/Co ratio. The gradually increasing inter-atomic distance between the neighboring cations at octahedral sites is measured from atomic position picking (Figs. 3.3c and 3.4).[35] The Fast Fourier Transformation (FFT) pattern of the transmission electron microscopy (TEM) image taken along the Co_3O_4 <001> zone axis shows continuous line-shaped extension patterns of square lattice of Co_3O_4, indicating continuously increasing lattice distance in the shell (Fig. 3.3d). Gradual increase of lattice distance is also observed for both e_{xx} and e_{yy} from geometric phase analysis (GPA, Fig. 3.5).[36] In contrast to Co_3O_4@Mn_3O_4 core-shell nanocubes (Fig. 3.6), the gradual increase in lattice distance indicates that the composition of the shell

is not homogeneous but changes gradually from the core to the surface without distinct strained interface. The energy-dispersive X-ray spectroscopy (EDS) elemental mapping of the nanocubes shows the coexistence of Co and Mn in the shell (Fig. 3.3e). EDS line scan and the intensity ratio between Co $L_{2,3}$- and Mn $L_{2,3}$-edges in line scan of electron energy loss spectra (EELS) directly shows gradual increase in Mn/Co-atomic ratio from core to the surface within the shell (Figs.3.3f and 3.7).

The gradient in composition was also applicable to other $Co_yMn_{1-y}O_x$ shells with different Mn/Co ratios. For a systematic comparison, $Co_yMn_{1-y}O_x$ shells with 5 different Mn/Co-atomic ratios are deposited by following the same synthetic method with different $Mn(HCOO)_2/Co(HCOO)_2$ ratios, denoted as $Co_{0.1}Mn_{0.9}$, $Co_{0.25}Mn_{0.75}$, $Co_{0.5}Mn_{0.5}$, $Co_{0.75}Mn_{0.25}$, and $Co_{0.9}Mn_{0.1}$ (Figs. 3.8a and 3.9). The composition gradient could be confirmed from gradual increase of inter-atomic distance from Co_3O_4 core to $Co_yMn_{1-y}O_x$ surface for all Mn/Co-atomic ratios (Fig. 3.8b), and their outermost Mn/Co-atomic ratio is referred from the Vegard's law.[37] The Mn/Co ratio of the outermost layer increases from $Co_{0.1}Mn_{0.9}$ to $Co_{0.5}Mn_{0.5}$, where most of the surface is covered by Mn in $Co_{0.5}Mn_{0.5}$. When the Mn content increases further, thicker Mn_3O_4 layer is generated at the surface with the Mn/Co mixed-phase underneath. The quantitative Mn/Co-atomic ratio of the shell from the X-ray photoelectron spectroscopy (XPS) analysis shows that the shell composition is dictated by the $Mn(HCOO)_2/Co(HCOO)_2$ ratio (Fig. 3.8c). Powder X-ray diffraction (PXRD) pattern, Raman, and Fourier

transform-infrared (FT-IR) spectra reveal that the nanocubes are cubic spinel with epitaxially grown $Co_yMn_{1-y}O_x$ shells (Fig. 3.10). We note that $Co_yMn_{1-y}O_x$ shell with composition gradient can also be epitaxially deposited on tetragonal spinel Mn_3O_4 nanocubes (Figs. 3.11-3.13).

To confirm the surface-preference of Mn in Co_3O_4@$Co_yMn_{1-y}O_x$ core-shell nanostructures, we compared DFT-calculated electronic energies of more than twenty different configurations of $Co_yMn_{1-y}O_x$ (Fig. 3.8d). The results demonstrate that the structures with high Mn surface densities are energetically more preferred for all Mn/Co compositions, confirming the strong surface preference of Mn in $Co_yMn_{1-y}O_x$. Therefore, at specific Mn/Co-atomic ratio, the composition gradient with Mn-rich surface leads to thermodynamically more stable shell structure than the homogeneously mixed shell. The experimental and computational results confirm that facet-defined and strain-free oxide surfaces with different Mn/Co ratios are successfully prepared as model oxide systems, where atomic gradient of Mn is present from surface to bulk (Fig. 3.8e).

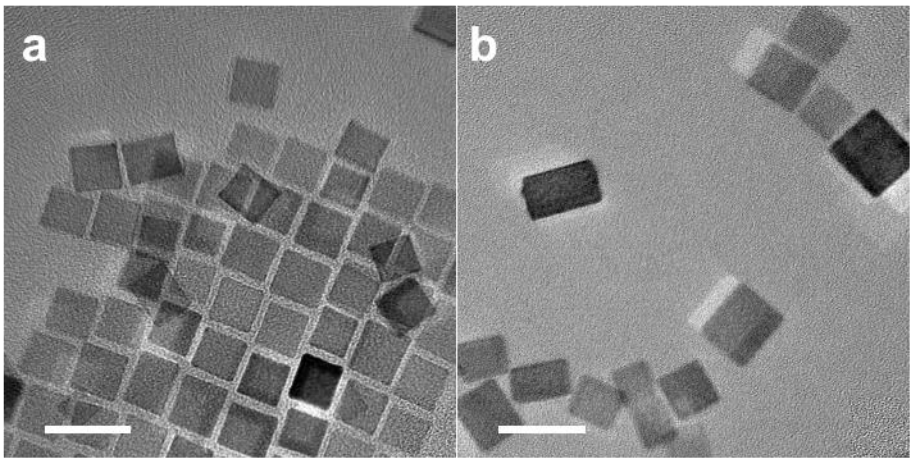

Figure 3.2. (a) A TEM image of Co_3O_4 nanocubes. (b) A TEM image of Mn_3O_4 nanocubes. Scale bar is 20 nm.

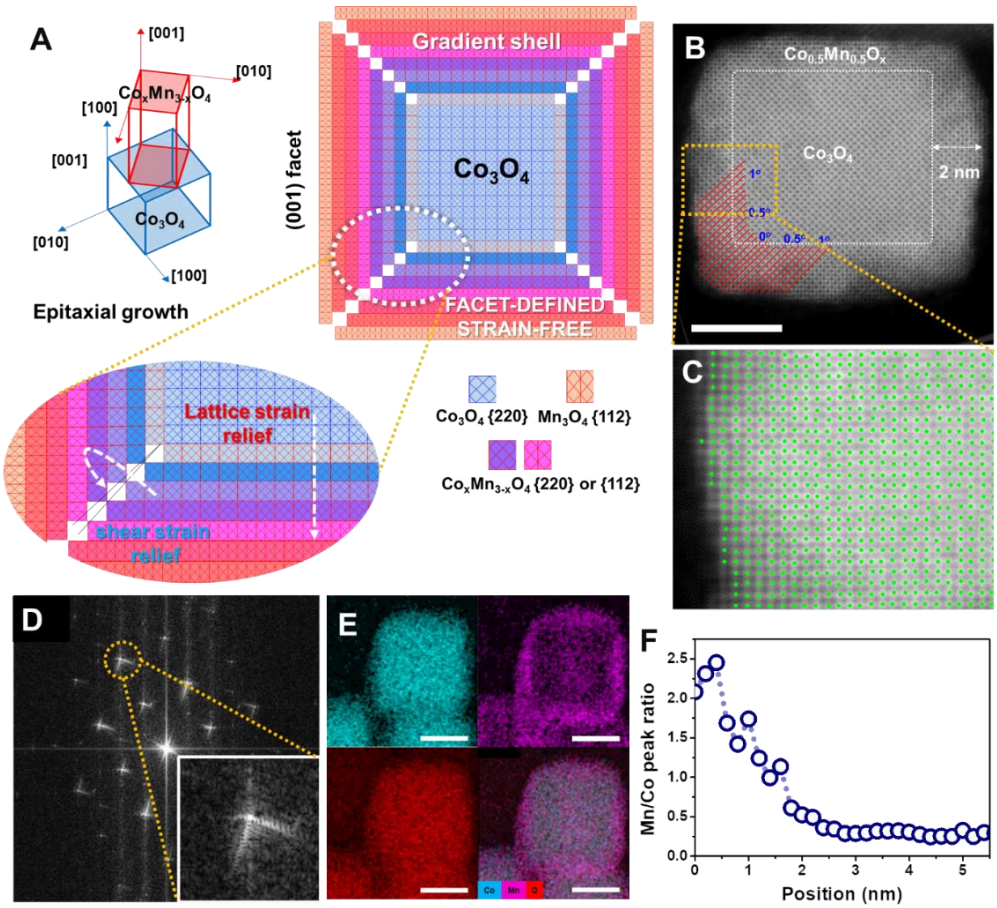

Figure 3.3. Synthesis of facet-defined Co_3O_4@$Co_yMn_{1-y}O_x$ core-shell nanocubes with composition gradient. (a) Schematic illustration of composition gradient for strain minimization. Left top, relative orientation of unit cells of epitaxially grown $Co_xMn_{3-x}O_4$ on Co_3O_4. The enlarged illustration shows layer by layer strain relief. (b) A HAADF-STEM image of a representative Co_3O_4@$Co_yMn_{1-y}O_x$ nanocube. Red lines show small gap closing at the corner. Scale bar is 5 nm. (c) Atomic positions of cations in octahedral-sites. (d) FFT pattern, enlarged FFT pattern (in set, linear-shaped pattern) and (e) EDS mapping image of a Co_3O_4@$Co_yMn_{1-y}O_x$ nanocube. Scale bar is 10 nm. (f) The ratio between Mn $L_{2,3}$-edge peak and Co $L_{2,3}$-

edge peak from EELS line scan taken in every 2 Å from the surface to the core.

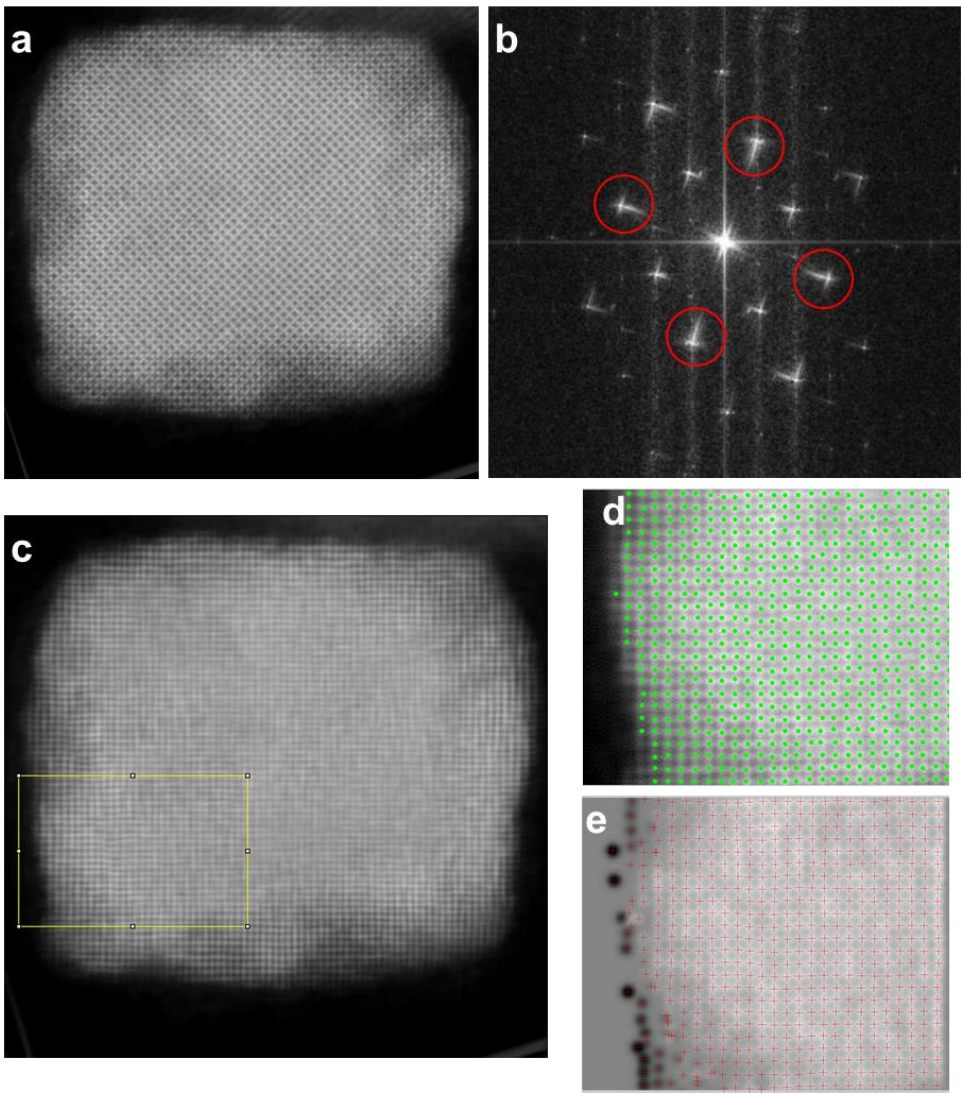

Figure 3.4. (a) original HAADF-STEM image. (b) FFT pattern obtained from original image (a). (c) Inverse FFT image of red-marked spots in (b). (d) Rough picking of atomic position. (e) Gaussian fitting of atomic position from (d). From the high-resolution STEM image, the atomic distance between the cations which reside in octahedral-sites of spinel unit cell could be measured from the several steps of atomic position peaking. First, the high resolution STEM image (a) is filtered from its fast Fourier

transformation (FFT) pattern by picking {100} diffraction spots to get the cation position at octahedral-sites (b). After converting the filtered FFT pattern to inverse FFT image, only octahedral site cations appear in the image (c). The rough atomic position is picked from the image (d). These atomic positions of cations are fitted with Gaussian function to get the real atomic position (e). From this position coordinates, the inter-atomic distance between neighboring cations in octahedral sites is plotted.

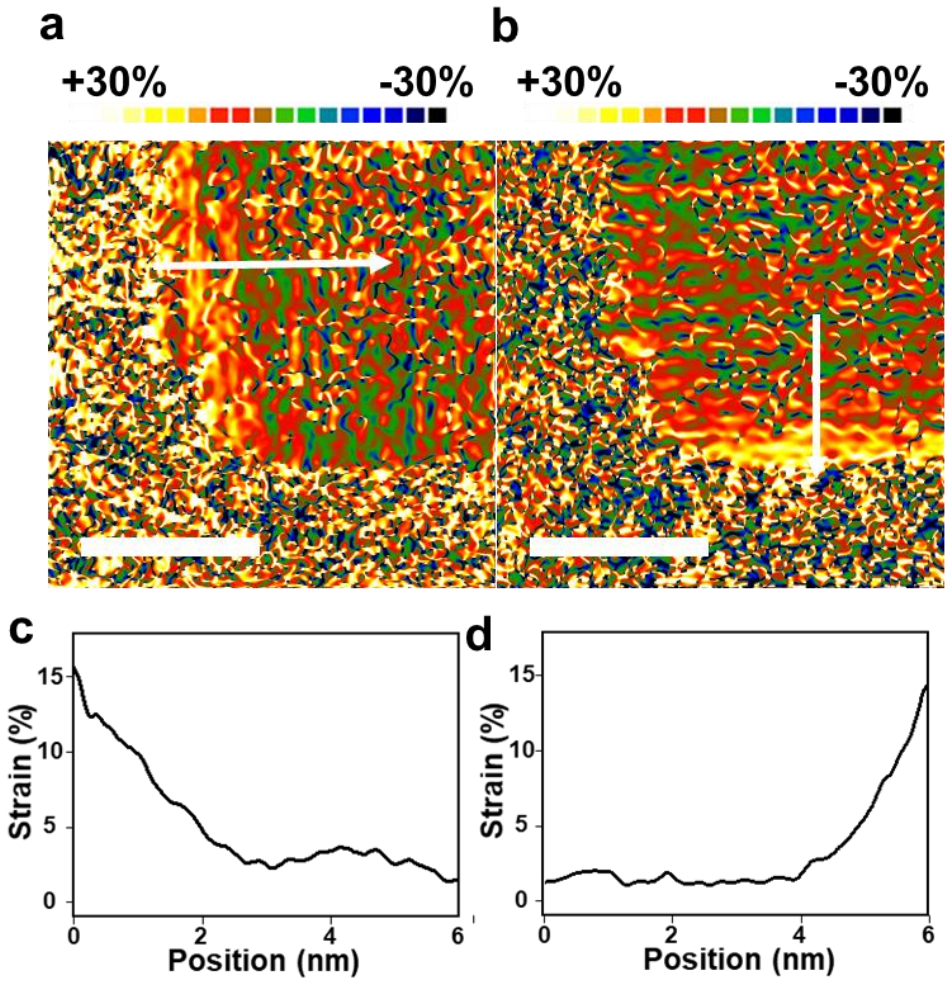

Figure 3.5. (a,b) GPA analysis of $Co_{0.5}Mn_{0.5}$ nanocubes showing e_{xx} strain field (a) and e_{yy} strain field (b). (c,d) e_{xx} strain plot (c) and e_{yy} strain plot (d) from GPA of $Co_{0.5}Mn_{0.5}$ nanocubes.

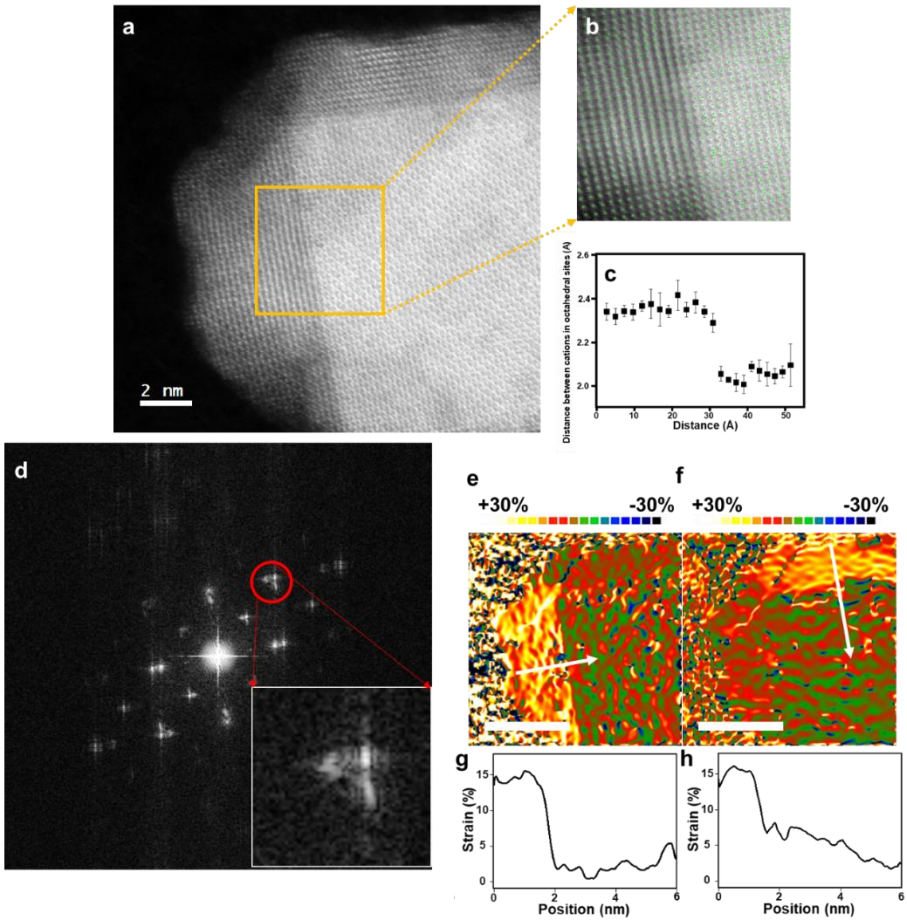

Figure 3.6. (a) HAADF-STEM image of Co_3O_4@Mn_3O_4 core shell nanocrystal. (b) atomic position peaking and Gaussian fitting for Co_3O_4@Mn_3O_4 core shell nanocrystal. (c) inter atomic distance plot of octahedral site cations according to the position. The step-like increase in the distance between neighboring octahedral site cations are observed. (d) FFT pattern of Co_3O_4@Mn_3O_4 core shell nanocrystal. Distinct spots are observed due to the discreet difference in lattice distance of Co_3O_4 and Mn_3O_4 at the interface. (e,f) GPA analysis of Co_3O_4@Mn_3O_4 nanocubes showing e_{xx} strain field (e) and e_{yy} strain field (f). (g,h) e_{xx} strain plot (g) and e_{yy} strain plot (h) from GPA of a Co_3O_4@Mn_3O_4 nanocube.

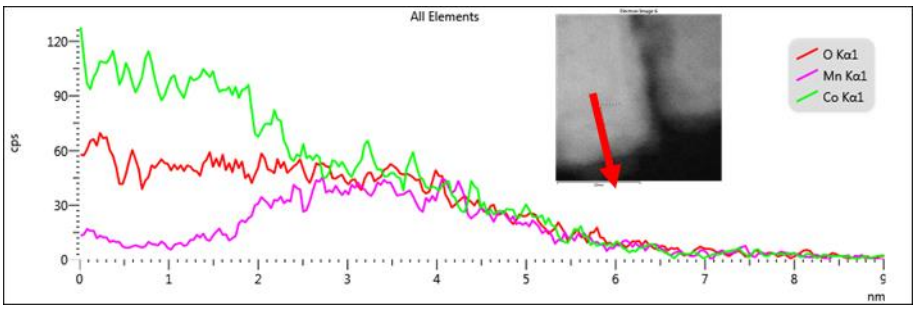

Figure 3.7. EDS line scan of $Co_{0.5}Mn_{0.5}$ nanocubes.

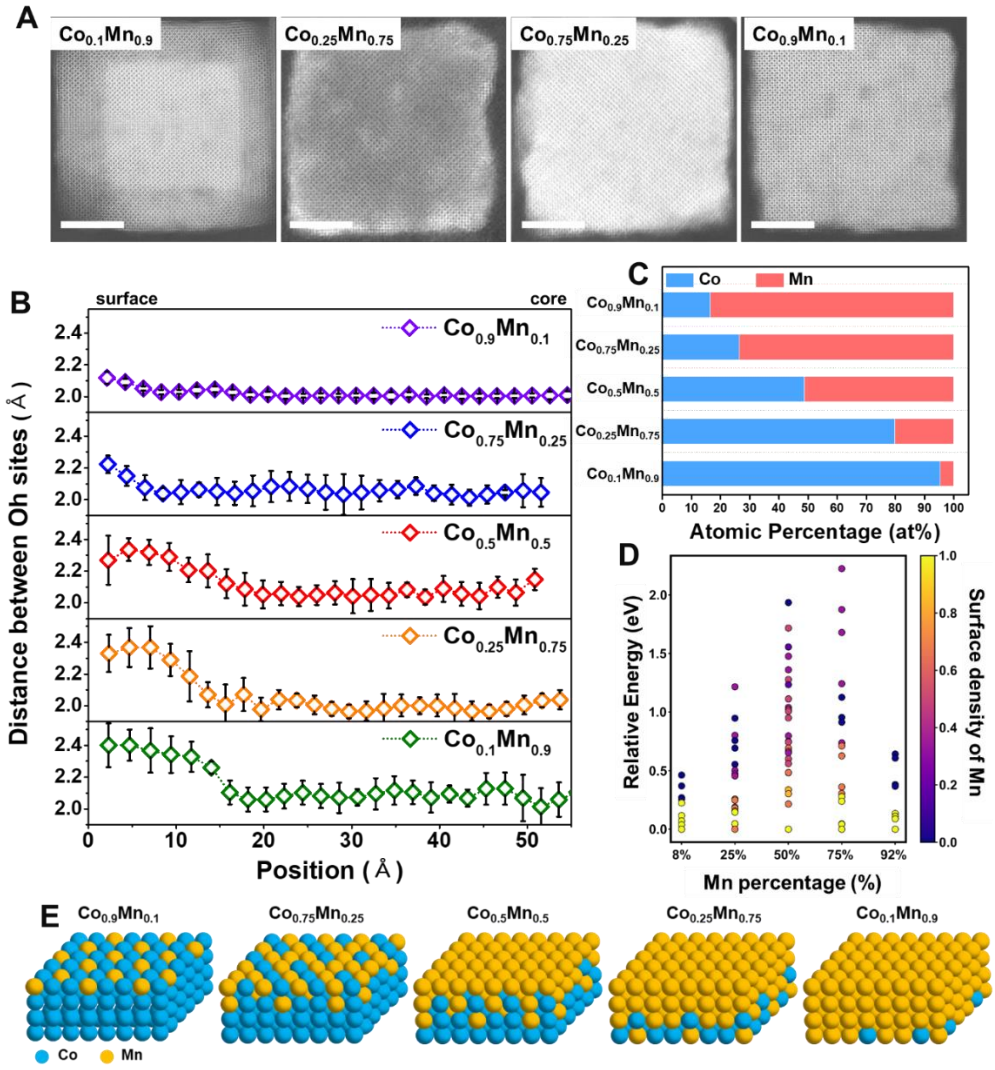

Figure 3.8. Surface Mn/Co control in facet-defined and strain-free spinel $Co_yMn_{1-y}O_x$ oxide surface. (a) HAADF-STEM images of $Co_{0.1}Mn_{0.9}$, $Co_{0.25}Mn_{0.75}$, $Co_{0.75}Mn_{0.25}$, and $Co_{0.9}Mn_{0.1}$ nanocubes. Scale bar is 5 nm. (b) Interatomic distance of cations in octahedral-sites plotted along the position from the surface to the core. (c) Mn and Co atomic percentage profile of Co_3O_4@$Co_yMn_{1-y}O_x$ nanocubes calculated by XPS. (d) DFT calculated relative energies for various Mn/Co ratio. The relative energies were

calculated with respect to the most stable configuration for each Mn/Co ratio. Marker colors correspond to their surface density of Mn, i.e., (the number of surface Mn)/(the number of total Mn). (e) Schematic illustration of the behavior of composition gradient and surface composition according to the Mn/Co ratio.

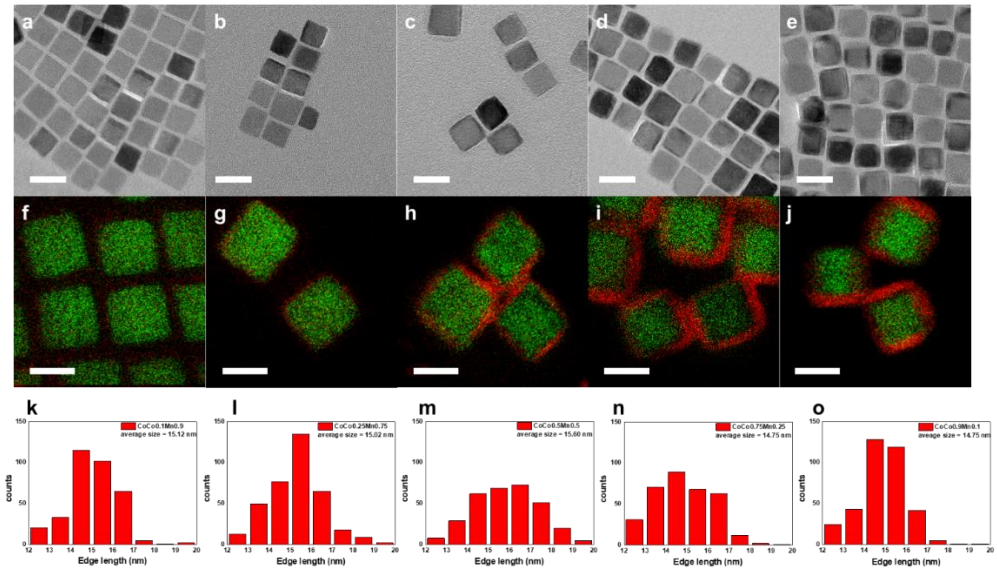

Figure 3.9. (a-e) TEM images of $Co_{0.1}Mn_{0.9}$ (a), $Co_{0.25}Mn_{0.75}$ (b), $Co_{0.5}Mn_{0.5}$ (c), $Co_{0.75}Mn_{0.25}$ (d), and $Co_{0.9}Mn_{0.1}$ (e) nanocubes. Scale bar is 20 nm. (f-j) Energy filtered transmittance electron microscopy (EF-TEM) mapping image of $Co_{0.1}Mn_{0.9}$ (f), $Co_{0.25}Mn_{0.75}$ (g), $Co_{0.5}Mn_{0.5}$ (h), $Co_{0.75}Mn_{0.25}$ (i), and $Co_{0.9}Mn_{0.1}$ (j) nanocubes. Scale bar is 10 nm. (k-o) Histogram of size distribution of $Co_{0.1}Mn_{0.9}$ (k), $Co_{0.25}Mn_{0.75}$ (l), $Co_{0.5}Mn_{0.5}$ (m), $Co_{0.75}Mn_{0.25}$ (n), and $Co_{0.9}Mn_{0.1}$ (o) nanocubes. The average sizes of the nanocubes were ~15 nm and Mn/Co was coexisting at the shell.

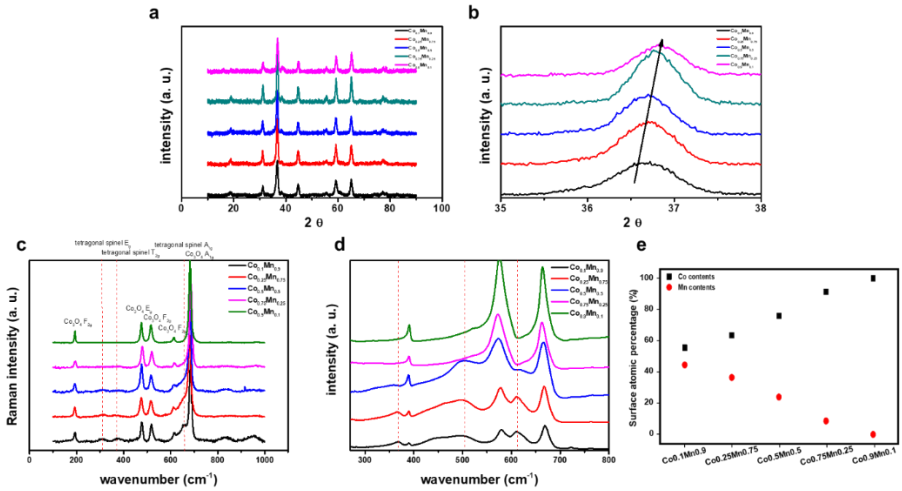

Figure 3.10. (a) XRD patterns of Co_3O_4@$Co_yMn_{1-y}O_x$ nanocubes. (b) detailed XRD patterns of Co_3O_4@$Co_yMn_{1-y}O_x$ nanocubes near 37°. All nanocubes were cubic spinel with small lattice distance difference due to the epitaxially grown spinel $Co_yMn_{1-y}O_x$ shell. (c) Raman spectra of Co_3O_4@$Co_yMn_{1-y}O_x$ nanocubes. (d) FT-IR spectra of Co_3O_4@$Co_yMn_{1-y}O_x$ nanocubes. Raman and FT-IR shows that all nanocubes are cubic spinel and increased Mn content cause the appearance of the tetragonal spinel oxide peaks. (e) ICP-AES elemental analysis of Co_3O_4@$Co_yMn_{1-y}O_x$ nanocubes. The overall composition is also ruled by the injecting Mn/Co precursor ratio.

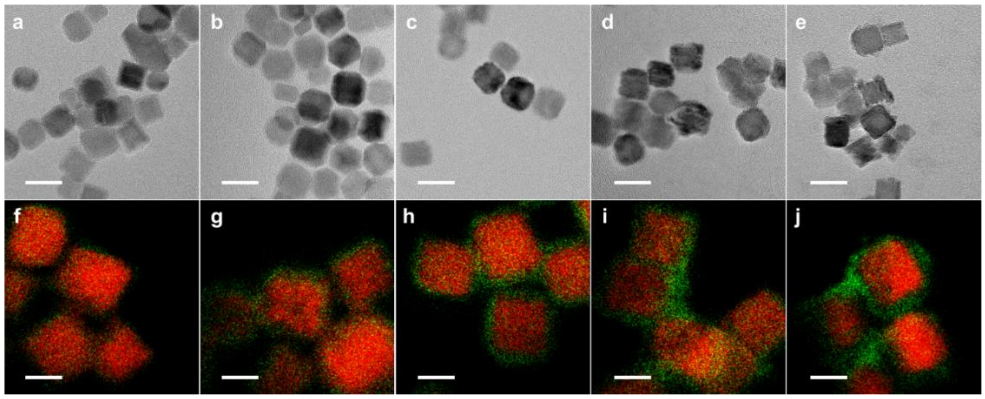

Figure 3.11. (a-e) TEM images of Mn3O4@$Co_{0.1}Mn_{0.9}$ (a), Mn_3O_4@$Co_{0.25}Mn_{0.75}$ (b), Mn_3O_4@$Co_{0.5}Mn_{0.5}$ (c), Mn_3O_4@$Co_{0.75}Mn_{0.25}$ (d), and Mn_3O_4@$Co_{0.9}Mn_{0.1}$ (e) nanocubes. Scale bar is 20 nm. (g-k) EF-TEM mapping image of Mn_3O_4@$Co_{0.1}Mn_{0.9}$ (f), Mn_3O_4@$Co_{0.25}Mn_{0.75}$ (g), Mn_3O_4@$Co_{0.5}Mn_{0.5}$ (h), Mn_3O_4@$Co_{0.75}Mn_{0.25}$ (i), and Mn_3O_4@$Co_{0.9}Mn_{0.1}$ (j) nanocubes. Scale bar is 10 nm. All nanocrystals have cubic morphology with ~15 nm size and EF-TEM shows the coexistence of Mn/Co in the shell.

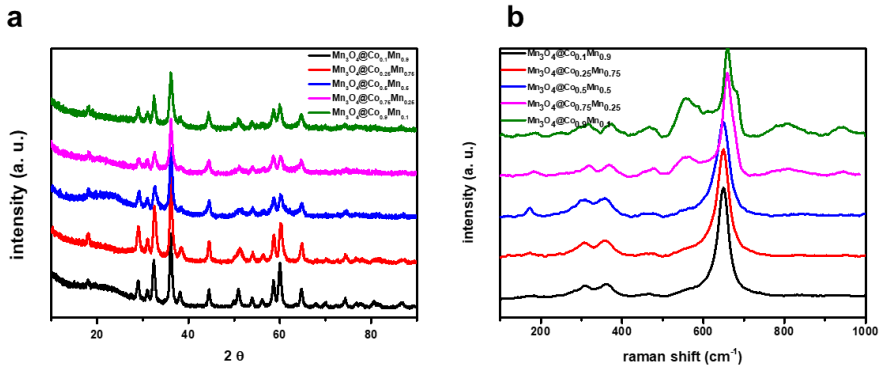

Figure 3.12. (a) XRD patterns of $Mn_3O_4@Co_yMn_{1-y}O_x$ nanocubes. (b) Raman spectra of $Mn_3O_4@Co_yMn_{1-y}O_x$ nanocubes. All nanocubes have tetragonal spinel structures and cubic phase emerges with high Co concentration.

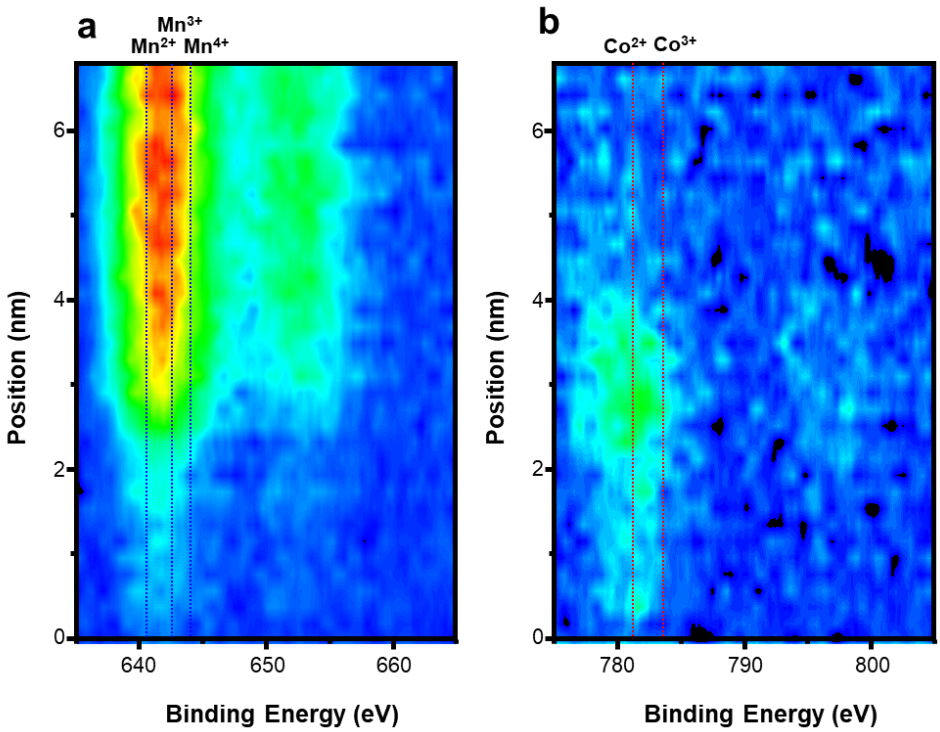

Figure 3.13. (a,b) EELS line scan of Mn $L_{2,3}$-edge (a) and Co $L_{2,3}$-edge (b) spectra of Mn_3O_4@$Co_{0.5}Mn_{0.5}$ nanocubes. The gradational composition change and Mn/Co charge transfer are also observable.

3.3.2 Charge distribution between Co and Mn in $Co_yMn_{1-y}O_x$ shell structure

The investigation of charge distribution on the oxide surface according to the Mn/Co ratio excepting facet- or strain-related factors was possible with synthesized nanocubes. First, line scans of Co and Mn L-edge EELS data are obtained.[38] The presence of high-valence Mn near the interface and Co^{2+} near the surface is established from the peak shifts of both Co and Mn L-edge to low–energy side, and the decrease of the peak intensity ratio of L_3/L_2 as moving from the surface to the core (Figs. 3.14a-c and 3.15). The co-existence of oxidized Mn and reduced Co ions is attributed to electron transfer from Mn to Co, especially when one of them is a minority in a spinel unit cell. For instance, Mn^{4+} is predominant in $Co_{0.9}Mn_{0.1}$ (Fig. 3.14c), but the presence of Co^{2+} along the shell of $Co_{0.1}Mn_{0.9}$ is clearly identified (Fig. 3.14a). Therefore, the charge transfer from Mn to Co occurs regardless of the Mn/Co-atomic ratio, generating oxidized Mn and reduced Co in the shell.

Further investigations on the surface charge distribution were carried out by using XPS and X-ray absorption near edge structure (XANES) analysis. In XPS spectra, both Co 2p and Mn 2p peaks shift to lower binding energy side with the increase of Mn/Co-atomic ratio due to different degrees of charge transfer (Fig. 3.14d,e). Co is found to be further reduced to Co^{2+} with decreasing Co content while Mn is further oxidized to Mn^{4+} with decreasing Mn content (Fig. 3.16) because most of the cations suffer from the charge

transfer when they are minorities. The difference in the absorption edge energy of Co K-edge in the XANES spectra is hardly discernible due to the Co_3O_4 core, but that of Mn K-edge spectra shifts to higher energy with lower Mn concentration owing to the increase in oxidation states of Mn (Fig. 3.17a,b,e). The XPS and XANES spectra for the nanocubes with Mn_3O_4 core show similar behavior of charge transfer, wherein Co is found to be reduced state at the low Co concentration (Figs. 3.17c,d and 3.18).

To support the preference of octahedral (O_h)-site for Mn and tetrahedral (T_d)-site for Co on facet-defined and strain-free oxide surface,[26,39] the extended X-ray absorption fine structure (EXAFS) is plotted in R-space using k^3-weighted Fourier-transformation (Figs. 3.14f and 3.19a). For Mn K-edge, with decreasing of Mn content, the first peak (~1.5 Å, transition metal (TM)-O bond) shifts to shorter bond, the ratio between the second peak (~2.5 Å, TM in O_h-site) and the third peak (~3.0 Å, TM in T_d-site) increases, and the third peak is merged to a single peak. These results indicate that the high portion of Mn^{4+} is at O_h-site without J-T distortion in Mn-poor nanocubes (from $Co_{0.9}Mn_{0.1}$ to $Co_{0.5}Mn_{0.5}$), and existence of surface Mn_3O_4 in Mn-rich nanocubes (from $Co_{0.5}Mn_{0.5}$ to $Co_{0.1}Mn_{0.9}$).[27,40] The broad pre-edge peak of Mn K-edge in XANES near 6542 eV also reveals the high O_h/T_d ratio in Mn-poor nanocubes (Fig. 3.19b).[41] The same trend is observed for $Mn_3O_4@Co_yMn_{1-y}O_x$ from its Co K-edge EXAFS, which shows low-valence Co tends to reside in T_d-sites (Fig. 3.19c,d). Likewise, the Mn/Co cation distribution on the oxide surface changes

according to the composition, not depending on the facet- or strain-related factors.

In Mn-poor oxide (Mn/Co = 0.08, 0.25, 0.5, see Supporting Information for Model Construction), the Bader charge analysis demonstrates that surface Mn atoms are more oxidized (+1.66e^-, +1.60e^-, +1.60e^-) compared to Mn_3O_4 (+1.58e^-), corroborating the electron transfer from Mn to Co. Furthermore, we observed strong oxidation of surface Mn when Mn/Co ratio is 0.08 (Fig. 3.14g), which agrees well with more oxidized Mn for $Co_{0.9}Mn_{0.1}$ that was confirmed by XPS (Fig. 3.14e). From these studies, we can experimentally and computationally confirm that the charge transfer from Mn to Co governs the surface cation distribution at the strain-free (001) facet (Fig. 3.14h).

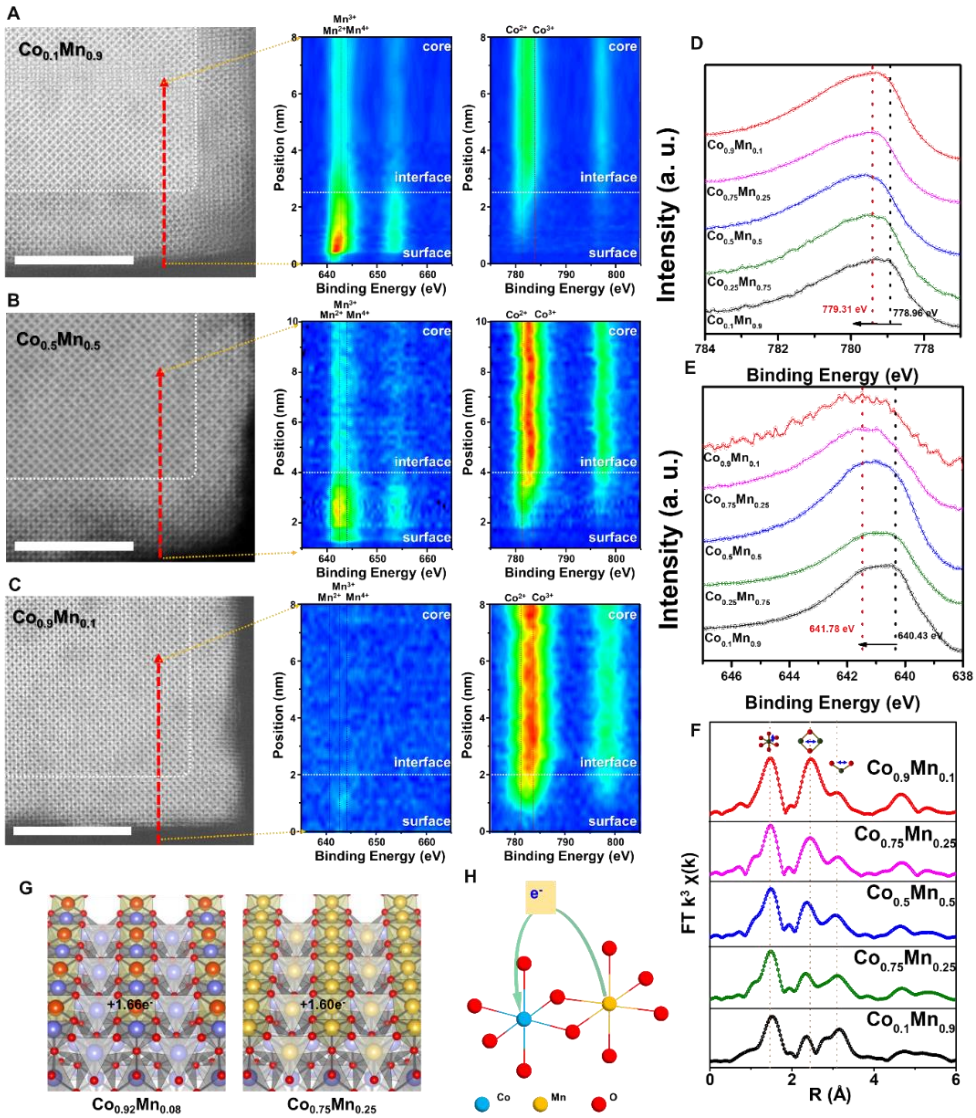

Figure 3.14. Cation distribution on the facet-defined and strain-free spinel $Co_yMn_{1-y}O_x$ oxide surface. (a-c) Line scan of Mn L-edge and Co-L edge EELS of the $Co_{0.1}Mn_{0.9}$ (a), $Co_{0.5}Mn_{0.5}$ (b), and $Co_{0.9}Mn_{0.1}$ (c) nanocubes. (d) Co 2p and (e) Mn 2p XPS spectra, and (f) k^3-weighted Fourier transformation of Mn K-edge EXAFS spectra of Co_3O_4@$Co_yMn_{1-y}O_x$ nanocubes. (g) Graphical representations of Bader charges for $Co_{1-x}Mn_x$ (x = 0.08, 0.25). Color codes: orange (Mn), blue (Co). Darker color corresponds

to higher Bader charges, indicating higher oxidation states. We confirmed more significant charge transfer from Mn (orange) to Co (blue) when Mn/Co ratio is smaller. (h) Schematic illustration of electron transfer from Mn to Co at the octahedral-site of spinel.

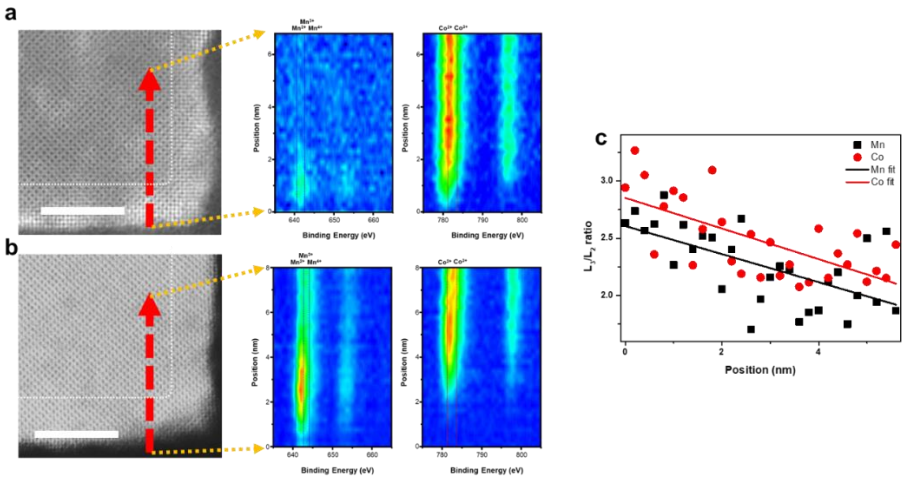

Figure 3.15. (a,b) HAADF-STEM images and line scan of Mn L-edge and Co L-edge EELS of the $Co_{0.25}Mn_{0.75}$ (a) and $Co_{0.75}Mn_{0.25}$ (b) nanocube. (c) The peak intensity ratio of L_3/L_2 for both Co and Mn in EELS line scan from the surface to the core of $Co_{0.5}Mn_{0.5}$. The increase in L_3/L_2 indicates decrease in oxidation state.

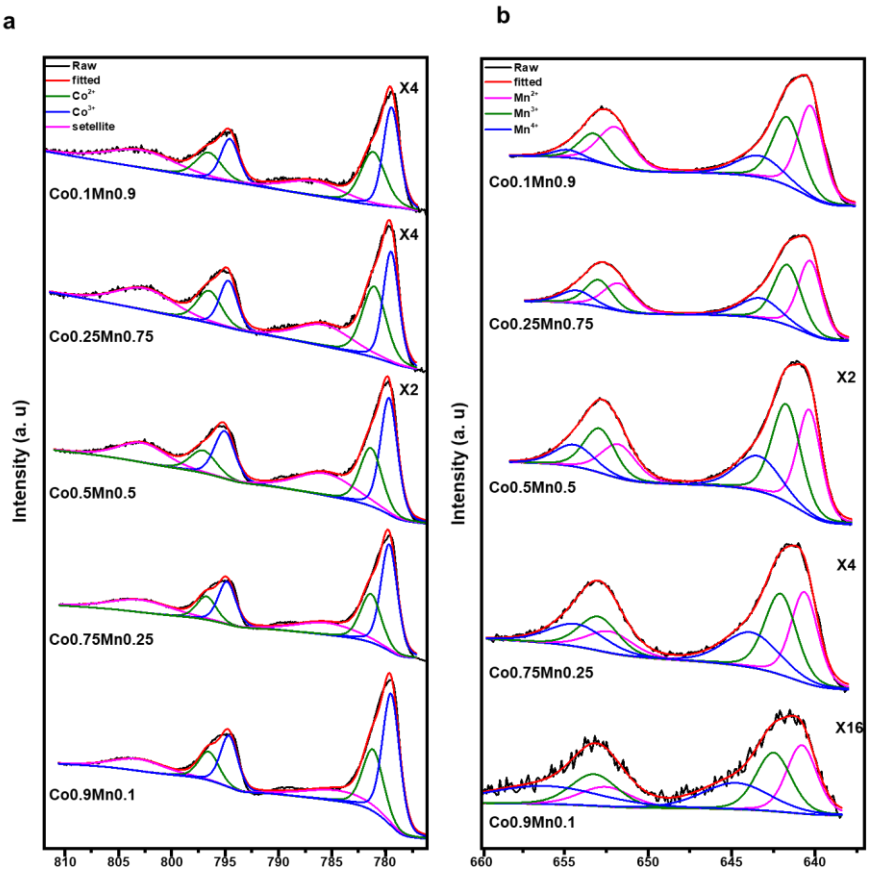

Figure 3.16. (a,b) Co 2p (a) and Mn 2p (b) XPS spectra of $Co_{0.25}Mn_{0.25}$ and $Co_{0.75}Mn_{0.25}$ nanocubes. Peak deconvolution of Co 2p XPS spectra of Co_3O_4@$Co_yMn_{1-y}O_x$. (b) Peak deconvolution of Mn 2p XPS spectra of Co_3O_4@$Co_yMn_{1-y}O_x$.

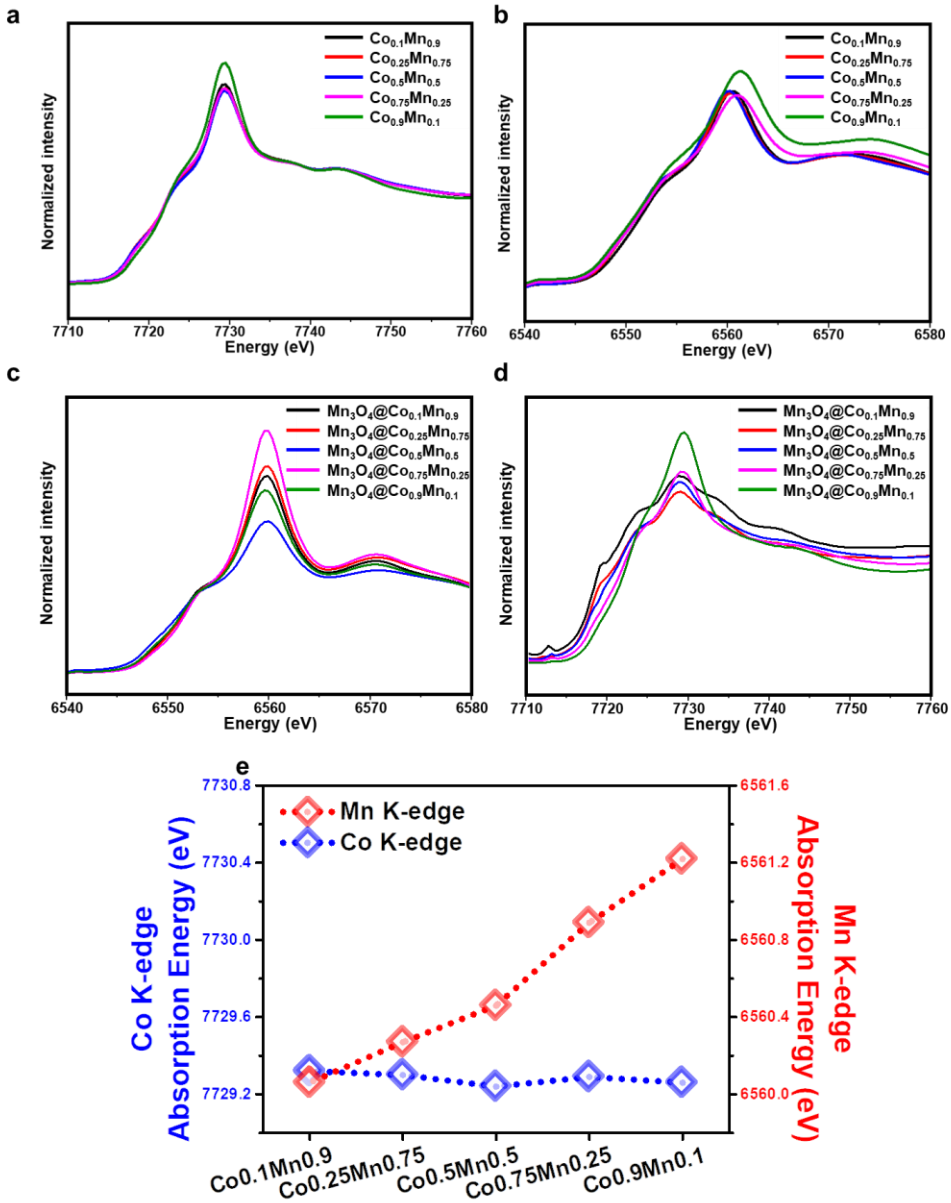

Figure 3.17. (a,b) Co K-edge (a) and Mn K-edge (b) XANES spectra of $Co_3O_4@Co_yMn_{1-y}O_x$ nanocubes. (c,d) Co K-edge (c) and Mn K-edge (d) XANES spectra of $Mn_3O_4@Co_yMn_{1-y}O_x$ nanocubes. (e) Absorption edge energy of Co K-edge (black spots) and Mn K-edge (red spots) XANES spectra of $Co_3O_4@Co_yMn_{1-y}O_x$.

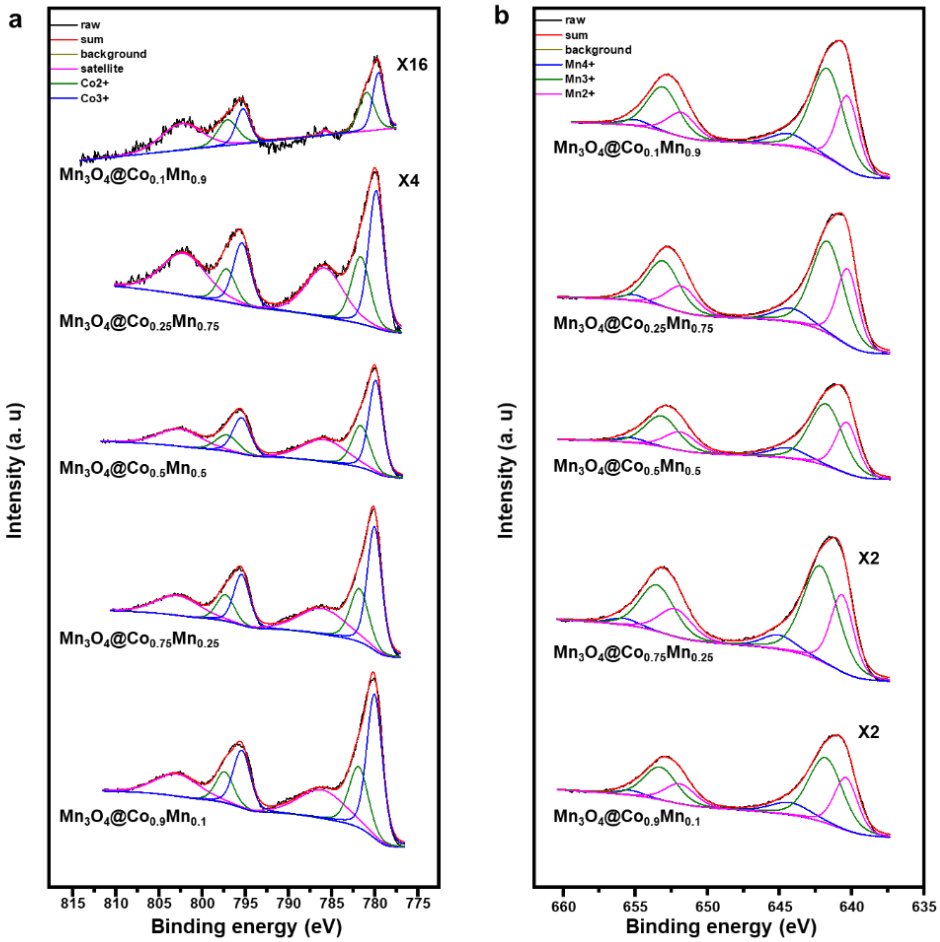

Figure 3.18. (a,b) Co 2p (a) and Mn 2p (b) XPS spectra of $Mn_3O_4@Co_yMn_{1-y}O_x$ nanocubes.

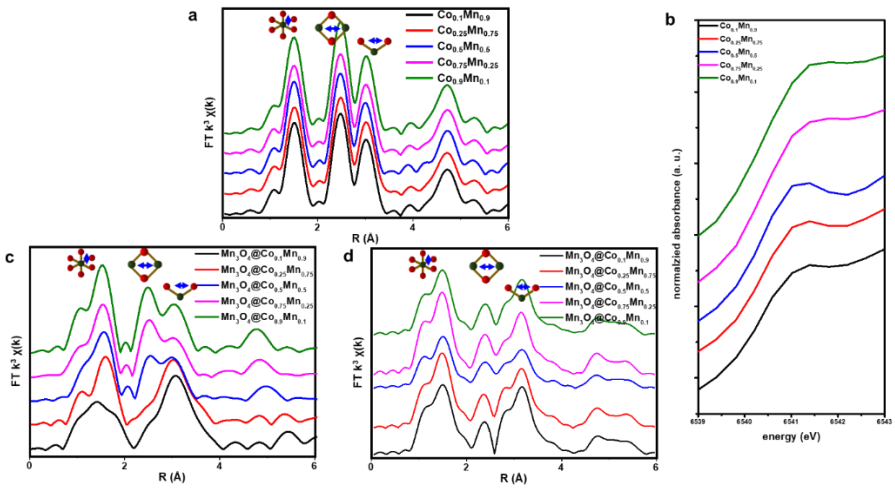

Figure 3.19. (a) Fourier transform of Co K-edge EXAFS spectra of Co_3O_4@$Co_yMn_{1-y}O_x$ nanocubes. The difference according to the Mn/Co ratio is little due to the high portion of the core Co_3O_4. (b) XANES pre-edge spectra of Co_3O_4@$Co_yMn_{1-y}O_x$ nanocubes. and Mn_3O_4@$Co_yMn_{1-y}O_x$ nanocubes. (c) Fourier transformation of Co K-edge EXAFS spectra of Mn_3O_4@$Co_yMn_{1-y}O_x$ nanocubes. Co cations tend to reside in Td site especially when they are minority cations. (d) Fourier transformation of Mn K-edge EXAFS spectra of Mn_3O_4@$Co_yMn_{1-y}O_x$ nanocubes. The difference according to the Mn/Co ratio is little due to the high portion of the core Mn_3O

3.3.3. Composition-structure-correlation with alkaline ORR activities on Co-Mn spinel surface

Without strain and facet-related factors, to understand how systematic changes of Mn/Co ratio and consequent electronic structure of $Co_yMn_{1-y}O_x$ surfaces are correlated to electrocatalysis, alkaline ORR activities are measured in 1 M KOH electrolyte as a model catalytic reaction. The spinel nanocrystals are deposited on carbon support (Vulcan XC-72), and ligands on oxide surface are mildly removed at 200 ^oC in air, preserving the surface structure (Fig. 3.20). Ligand-free oxide surfaces are confirmed by cyclic voltammetry (Fig. 3.21a). Notably, Mn^{3+}/Mn^{4+} redox peak gradually changes with increasing Mn/Co ratio, corroborating systematic control of the near-surface Mn/Co ratio. (Fig. 3.22) In ORR polarization curves (Fig. 3.21b), Mn cation on Co_3O_4 surface boosts overall ORR kinetics with lower overpotential, reaching comparable to benchmark Pt/C ($E_{1/2}$ = 0.906 V) for the best-performing $Co_{0.5}Mn_{0.5}$ ($E_{1/2}$ = 0.894 V). However, further increase of Mn in $Co_yMn_{1-y}O_x$ shell decreases ORR activity, revealing a volcano-like ORR activity trend with Mn/Co ratios. Similar to the activity, electron transfer number for ORR selectivity also shows the volcano trend with $Co_{0.5}Mn_{0.5}$ closest to 4-electron ORR pathway (Fig. 3.21c).

To quantitatively compare ORR electrocatalysis on facet- and strain-controlled environment, three activity metrics are used, including onset and half-wave potentials and mass activity at 0.9 V (Fig. 3.21d). Again, each activity metric shows volcano trends with $Co_{0.5}Mn_{0.5}$ at the top and

increasing/decreasing activity branches, suggesting structure-dependent ORR electrocatalysis on oxide surfaces. First, activity improvement on Mn-low branch could be originated from a combined effect of quantitative (increase in the number of active Mn-sites) and qualitative (higher turnover-frequency on each Mn-site) factors.[42,43] As Mn is more favorably populated on surface under defined facet, the outermost Mn/Co ratio reaches maximum at $Co_{0.5}Mn_{0.5}$ (Fig. 3.8b). Moreover, because of the electron transfer from Mn to Co, adequate charge transfer from $Mn^{3+/4+}$ cations in Oh-sites makes $Co_{0.5}Mn_{0.5}$ have the most ORR-active site (Fig. 3.14h).[27,43-45] However, further addition of Mn over $Co_{0.5}Mn_{0.5}$ does not provide quantitative merit on ORR because majority of the surface sites are already occupied by Mn. This activity even decreases in Mn-rich branch due to the weakened electronic interaction from subsurface Co under Mn_3O_4 surface (Fig. 3.8b).[44,45,46] When the ORR mass activity is normalized by Mn atomic ratio in Co-Mn oxide shell, much lower Mn specific activity can be recognized at Mn-rich branch than Mn-poor side (Fig. 3.21e). As a result, the highest activity of $Co_{0.5}Mn_{0.5}$ is achieved by delicate combination of increased ORR-active site density of octahedral Mn on the surface (quantitatively) and the optimal Mn valency from Co-rich subsurface layer (qualitatively), which leads to one of the highest alkaline ORR activities among Co-Mn spinel electrocatalysts (Table 3.4). Instead of cubic Co_3O_4, the $Co_yMn_{1-y}O_x$ shells on tetragonal Mn_3O_4 core (Mn_3O_4@$Co_yMn_{1-y}O_x$) also show the volcano-type ORR activity trend with Mn_3O_4@$Co_{0.25}Mn_{0.75}$ at the

top (Figs. 3.23-3.25). The structure with composition gradient enabled us to analyze the activity trend with same principle with tetragonal core under facet- and strain-controlled environment.

While strained phase is vulnerable to structural failure during electrocatalytic process,[47] improved structural stability is expected in Co_3O_4@$Co_yMn_{1-y}O_x$ due to the minimization of both lattice and shear strain by composition gradient (Fig. 3.3a). In chronoamperometry for prolonged operation of 14 hours at 0.8 V, $Co_{0.5}Mn_{0.5}$ exhibited excellent robustness with only 2% of the initial ORR activity decrease, compared to 12% loss of benchmark Pt/C catalysts (Figs. 3.21f, 3.26 and 3.27). Furthermore, the TEM images and XPS data show that the surface structures are preserved after the electrochemical analyses (Figs. 3.28 and 3.29).

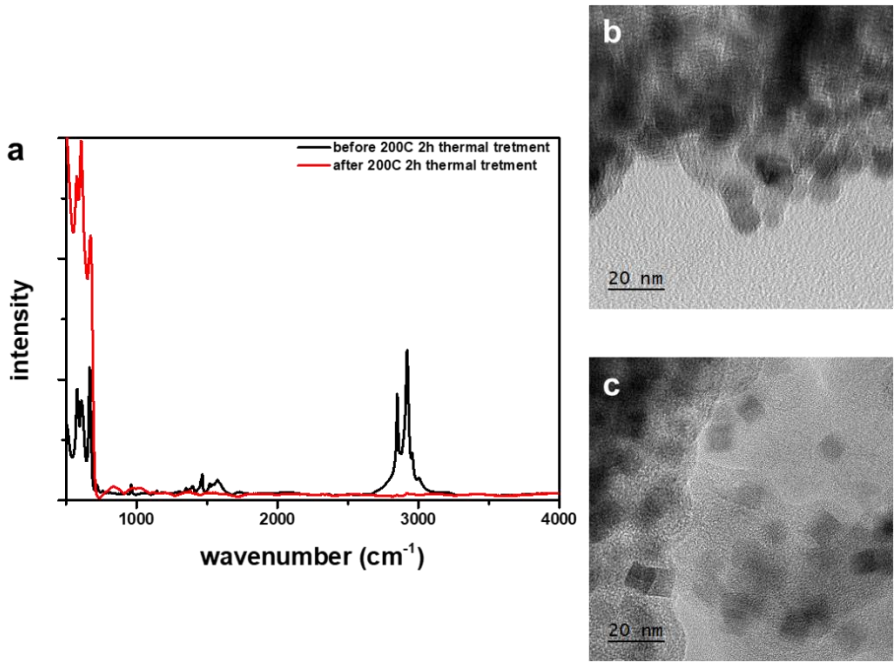

Figure 3.20. (a) FT-IR spectra of $Co_{0.5}Mn_{0.5}$ nanocubes before and after the ligand removal processing. (b) A TEM image of $Co_{0.5}Mn_{0.5}$ nanocubes after thermal treatment at 300 ^{o}C for 2h. The morphologies were not maintained and became round shape. (c) A TEM image of $Co_{0.5}Mn_{0.5}$ nanocubes after thermal treatment at 200 ^{o}C for 2h. The morphologies were maintained.

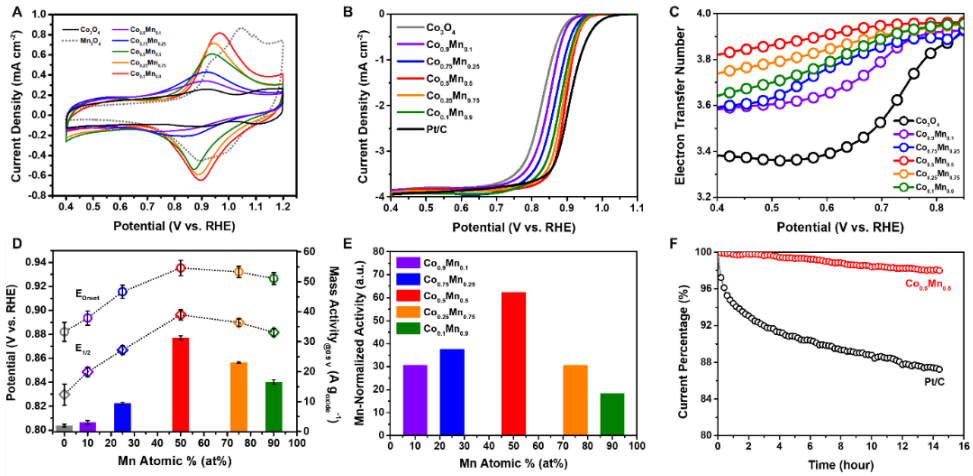

Figure 3.21. Electrochemical analyses of Co_3O_4@$Co_yMn_{1-y}O_x$ nanocubes in 1 M KOH electrolyte. (a) Cyclic voltammetry, (b) ORR polarization curves (rotating speed of 1600 rpm), (c) Electron transfer number in ORR, (d) Onset potential, half-wave potential, and mass activities at 0.9 V (vs. RHE) of Co_3O_4@$Co_yMn_{1-y}O_x$ nanocubes. (e) ORR activity of Co_3O_4@$Co_yMn_{1-y}O_x$ nanocubes at 0.9 V (vs. RHE) normalized by surface Mn ($Mn_{Surface}$) atomic percentages. (f) Chronoamperometry measurement at 0.8 V (vs. RHE) of $Co_{0.5}Mn_{0.5}$ and Pt/C at rotating speed of 800 rpm.

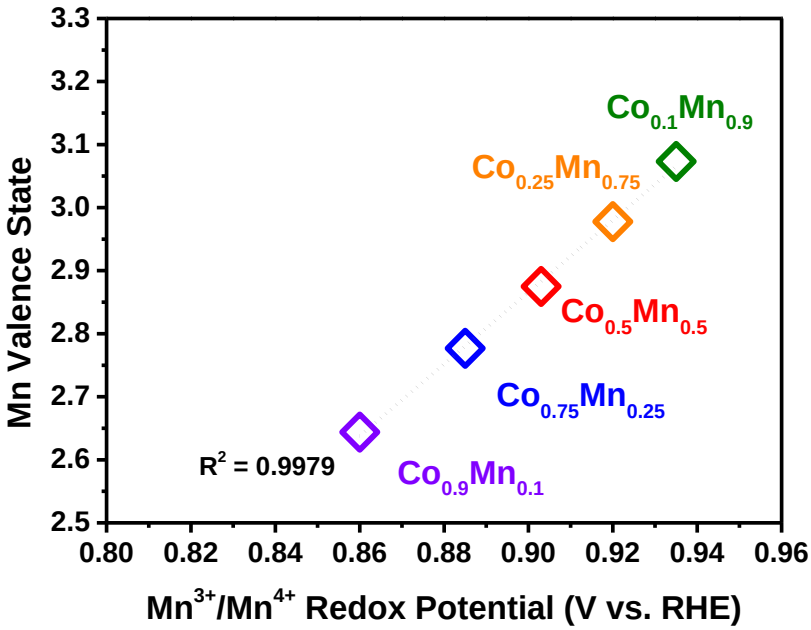

Figure 3.22. The correlation of Mn-redox potential and Mn valence state of Co_3O_4@$Co_yMn_{1-y}O_x$ nanocubes in Ar-saturated 1 M KOH.

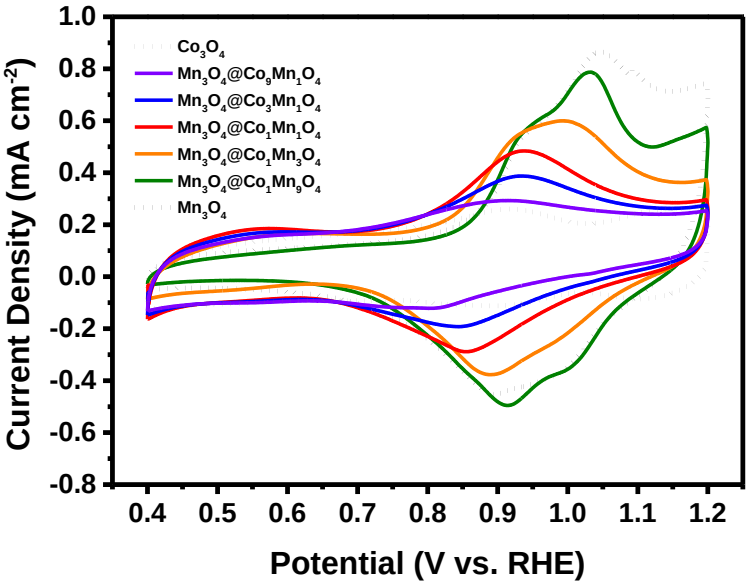

Figure 3.23. CV of Co_3O_4, Mn_3O_4, and Mn_3O_4@$Co_yMn_{1-y}O_x$ nanocubes in Ar-saturated 1 M KOH.

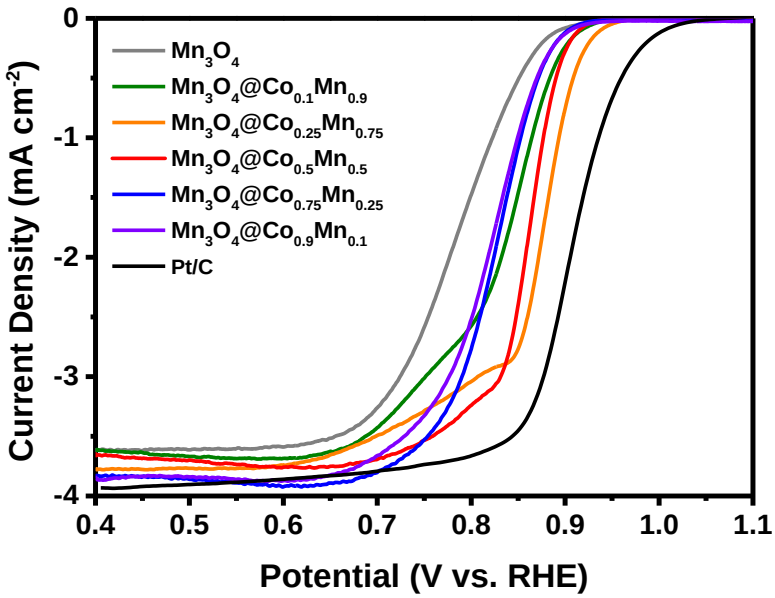

Figure 3.24. ORR polarization curves of $Mn_3O_4@Co_yMn_{1-y}O_x$ nanocubes in O_2-saturated 1 M KOH with rotating speed of 1600 rpm.

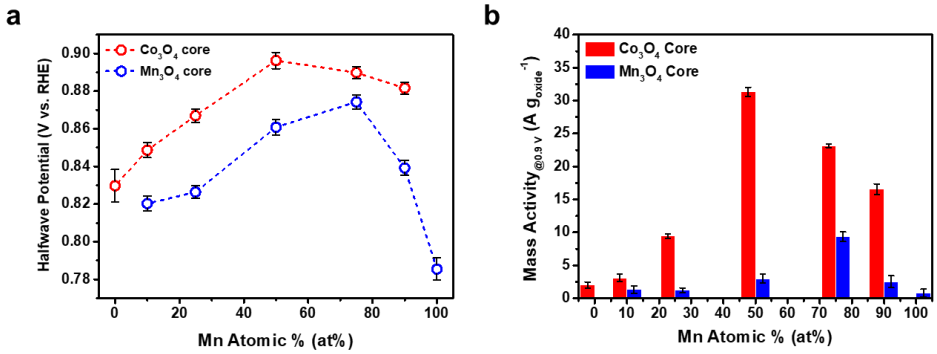

Figure 3.25. (a) ORR half-wave potentials of Co_3O_4@$Co_yMn_{1-y}O_x$ and Mn_3O_4@$Co_yMn_{1-y}O_x$ nanocubes. (b) ORR mass activity at 0.9 V (vs. RHE) of Co_3O_4@$Co_yMn_{1-y}O_x$ and Mn_3O_4@$Co_yMn_{1-y}O_x$ nanocubes.

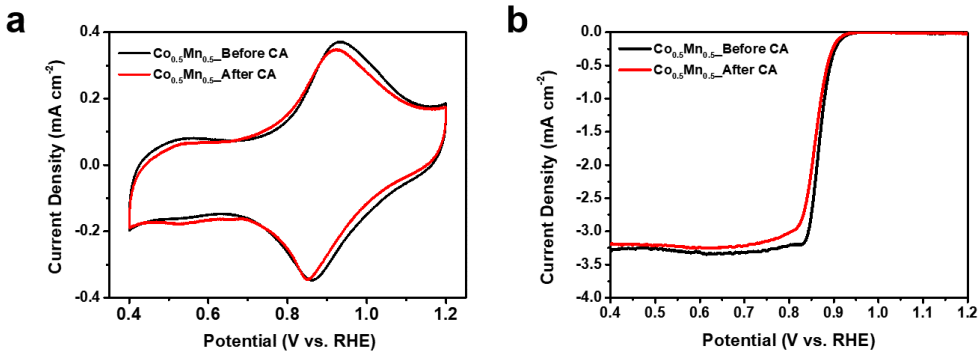

Figure 3.26. (a) Cyclic voltammetry (in Ar-saturated 1.0 M KOH) and (b) ORR polarization curves (in O_2-saturated 1.0 M KOH) of $Co_{0.5}Mn_{0.5}$ electrocatalyst before and after 15 hours of chronoamperometry (CA) stability test at 0.8 V (vs. RHE).

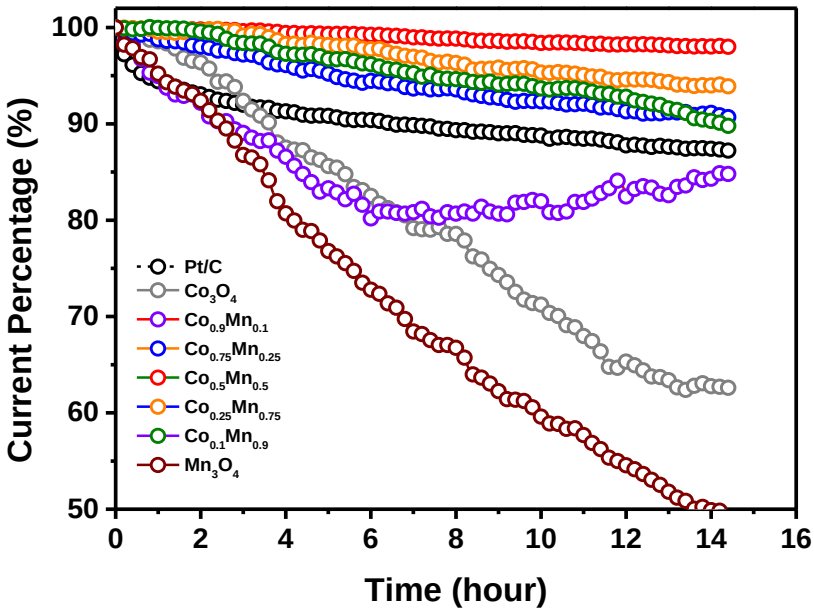

Figure 3.27. Chronoamperometry measurements of Co_3O_4, Mn_3O_4, Co_3O_4@$Co_yMn_{1-y}O_x$ nanocubes, and Pt/C at 0.8 V (vs. RHE) with rotating speed of 800 rpm.

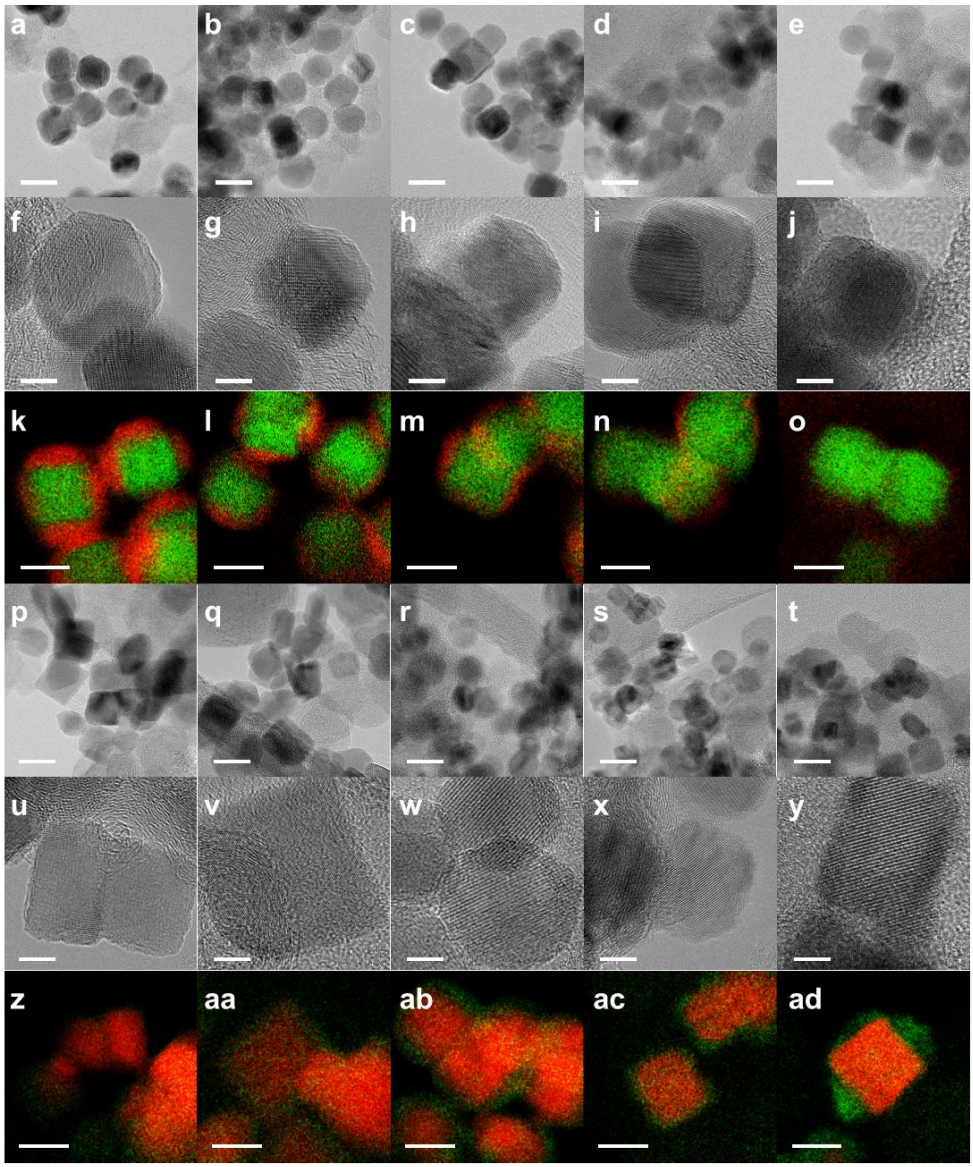

Figure 3.28. (a-ad) TEM images and EFTEM mapping images of nanocubes after the reaction. (a, f, k) $Co_{0.1}Mn_{0.9}$, (b, g, l) $Co_{0.25}Mn_{0.75}$, (c, h, m) $Co_{0.5}Mn_{0.5}$, (d, i, n) $Co_{0.75}Mn_{0.25}$, (e, j, o) $Co_{0.9}Mn_{0.1}$, (p, u, z) Mn_3O_4@$Co_{0.1}Mn_{0.9}$, (q, r, aa) Mn_3O_4@$Co_{0.25}Mn_{0.75}$, (r, w, ab) Mn_3O_4@$Co_{0.5}Mn_{0.5}$, (s, x, ac) Mn_3O_4@$Co_{0.75}Mn_{0.25}$, and (t, y, ad) Mn_3O_4@$Co_{0.9}Mn_{0.1}$. Scale bar is 20 nm for (a, b, c, d, e, p, q, r ,s, t), 5 nm for (f, g, h, i, j, u, v, w, x, y), and 10 nm for (k, l, m, n, o, z, aa, ab, ac, ad).

After the reaction, the morphology and composition distribution of the nanocrystals are maintained.

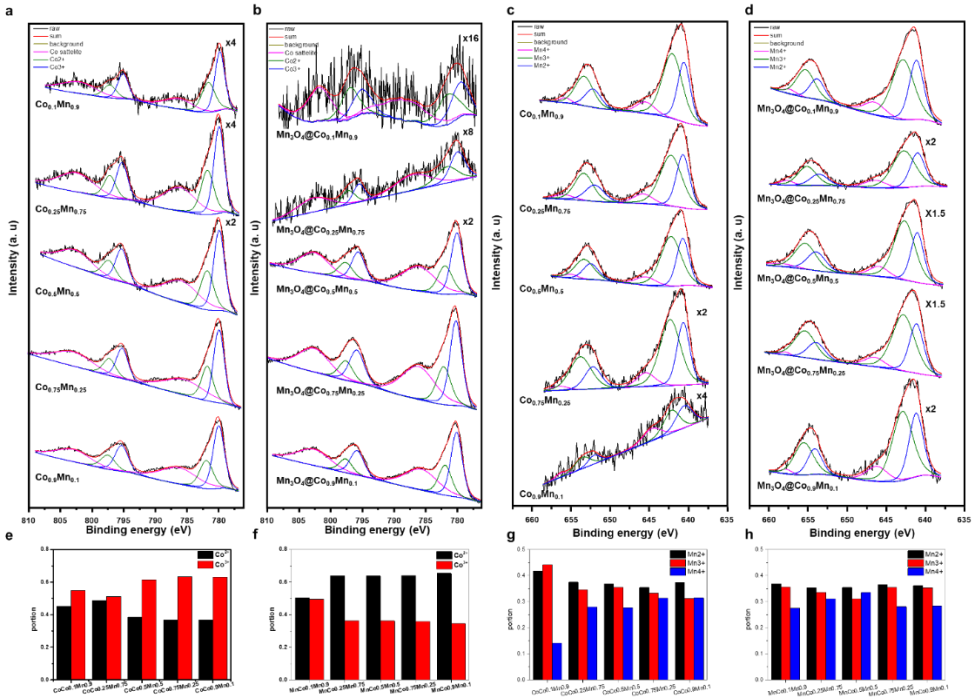

Figure 3.29. (a,b) Co 2p XPS spectra of $Co_3O_4@Co_yMn_{1-y}O_x$ (a) and $Mn_3O_4@Co_yMn_{1-y}O_x$ (b) nanocubes after the reaction. (c,d) Mn 2p XPS spectra of $Co_3O_4@Co_yMn_{1-y}O_x$ (c) and $Mn_3O_4@Co_yMn_{1-y}O_x$ (d) nanocubes after the reaction. (e,f) Co oxidation state of $Co_3O_4@Co_yMn_{1-y}O_x$ (e) and $Mn_3O_4@Co_yMn_{1-y}O_x$ (f) nanocubes after the reaction. (g,h) Mn oxidation state of $Co_3O_4@Co_yMn_{1-y}O_x$ (g) and $Mn_3O_4@Co_yMn_{1-y}O_x$ (h) nanocubes after the reaction. The oxidation state trend from the XPS peak deconvolution was unchanged after the reaction.

Table 3.4. Comparison of alkaline ORR activity and measurement conditions of various spinel oxide electrocatalysts.

Catalyst	Onset Potential [V vs. RHE]	Half-wave Potential [V vs. RHE]	Measurement Condition	Ref
MCF-0.8	0.95	0.89	1 M NaOH 0.1 mg_{oxide} cm^{-2}	*J. Am. Chem. Soc.* **2019** *141* 4412-4421
$CoMn_2O_4$/C **$MnCo_2O_4$/C**	0.91 0.92	0.844 0.855	1 M KOH 0.1 mg_{oxide} cm^{-2}	*Proc. Nat. Acad. Sci. U. S. A.* **2019** *116* 24425-24432
$Mn_{1.5}Co_{1.5}O_4$/C	0.92	0.85	1 M NaOH 0.1 mg_{oxide} cm^{-2}	*Nat. Commun.* **2019** *10* 1506
$MnCo_2O_3$/C	0.9	0.86	1 M KOH 0.1 mg_{oxide} cm^{-2}	*Chem. Mater.* **2019** *31* 9331-9337
Co_4N@CoO_x/C	0.93	0.875	1 M KOH 0.1 mg_{oxide} cm^{-2}	*J. Am. Chem. Soc.* **2019** *141* 19241-19245
Co_2FeO_4/NCNT	0.9	0.8	0.1 M KOH 0.2 mg_{oxide} cm^{-2}	*Angew. Chem. Int. Ed.* **2019** *58* 13291-13296
Co_3O_4-x HoNPs-90	0.91	0.834	0.1 M KOH 0.2 mg_{oxide} cm^{-2}	*Angew. Chem. Int. Ed.* **2019** *58* 13840-13844
Co_2VO_4	0.89	0.83	1 M KOH 0.25 mg_{oxide} cm^{-2}	*Adv. Mater.* **2020** *32* 1907168
$Zn_{0.4}Ni_{0.6}Co_2O_4$/NCNT	0.86	0.78	0.1 M KOH 0.21 mg_{oxide} cm^{-2}	*Angew. Chem. Int. Ed.* **2020** *59* 6492-6499
CuNiCo-5-5	0.92	0.79	0.1 M KOH 0.25 mg_{oxide} cm^{-2}	*ChemSuSChem* **2020** e202102404 (online published) https://doi.org/10.1002/cssc.202102404
$ZnCo_2O_4$-CNT-140/6	0.88	0.76	0.1 M KOH 0.25 mg_{oxide} cm^{-2}	*J. Electrochem. Soc.* **2020** *167* 050512
0.5%Ce-Co_3O_4	0.82	0.665	0.1 M KOH 0.1 mg_{oxide} cm^{-2}	*ChemistrySelect* **2021** *6* 3512-3518
MCF-Mn/KB	0.97	0.904	1 M KOH 0.1 mg_{oxide} cm^{-2}	*Adv. Mater.* **2021** 2107868 (online published) https://doi.org/10.1002/adma.202107868
Co_3O_4@$Co_{0.5}Mn_{0.5}O_x$	0.935	0.894	1 M KOH 0.1 mg_{oxide} cm^{-2}	(This study)

3.3.4. Theoretical investigation of structure-activity correlation on $Co_yMn_{1-y}O_x$ spinel surface

To investigate the accordance of the experimental model with calculation on well-defined structure, we performed spin-polarized DFT calculations to determine ΔG_{OH*}, the activity descriptor for ORR,[48] and predicted the theoretical limiting potential ($U_{L,\ ORR}$), defined as the highest potential at which all ORR reaction steps become exergonic. We considered various possibilities of crystal structures and lattices to plot the average and standard deviation of ΔG_{OH*}, where lower ΔG_{OH*} values indicate stronger binding affinities (Fig. 3.30). ΔG_{OH*} on $Co_{1-x}Mn_x$ (x=0.08, 0.25, 0.5) becomes stronger compared to Co_3O_4 as more Mn is introduced to the surface, while further increase in Mn (x=0.75, 0.92) inversely weakens ΔG_{OH*} (Fig. 3.30a). Correspondingly, the theoretical limiting potential demonstrated volcano trends, showing the highest U_L for Mn/Co=1, which is an excellent agreement with the overall trends in the experimental results (Fig. 3.30b). The free energy diagram confirms the lowest ORR overpotential for Mn/Co=1 due to its stronger binding of reaction intermediates compared to pure Co_3O_4 and Mn_3O_4 surfaces (Fig. 3.30c).

From both experimental and theoretical investigations excluding facet- and strain-related factors, we confirm that the enhancement in ORR activity with increasing Mn is originated from both quantitative (more surface Mn cations in O_h-sites, Fig. 3.30f) and qualitative (stronger ΔG_{OH*} on each Mn, Fig. 3.30a) aspects on a Mn-poor branch (from $Co_{0.9}Mn_{0.1}$ to

$Co_{0.5}Mn_{0.5}$).[27,44] However, on a Mn-rich branch (from $Co_{0.5}Mn_{0.5}$ to $Co_{0.1}Mn_{0.9}$), the thicker MnO_x underneath the Mn-saturated outermost surface leads to weakened ligand effect between top-lying Mn and subsurface Co cations. The charge density difference demonstrates that subsurface Co is less affected by OH* adsorption on $Co_{0.25}Mn_{0.75}$ compared to $Co_{0.5}Mn_{0.5}$, supporting the weakened ligand effect due to the elongated distance between the surface Mn and subsurface Co (Fig. 3.30d).[49] Consequently, DFT calculations suggest that appropriate ligand effects of subsurface Co on surface Mn play a key role in $Co_{1-x}Mn_x$ by tuning ΔG_{OH*} and thus improving ORR catalytic activity of Mn-sites. This good agreement between experimental and theoretical results is attributed to the strain-free and facet-defined nanomaterials.

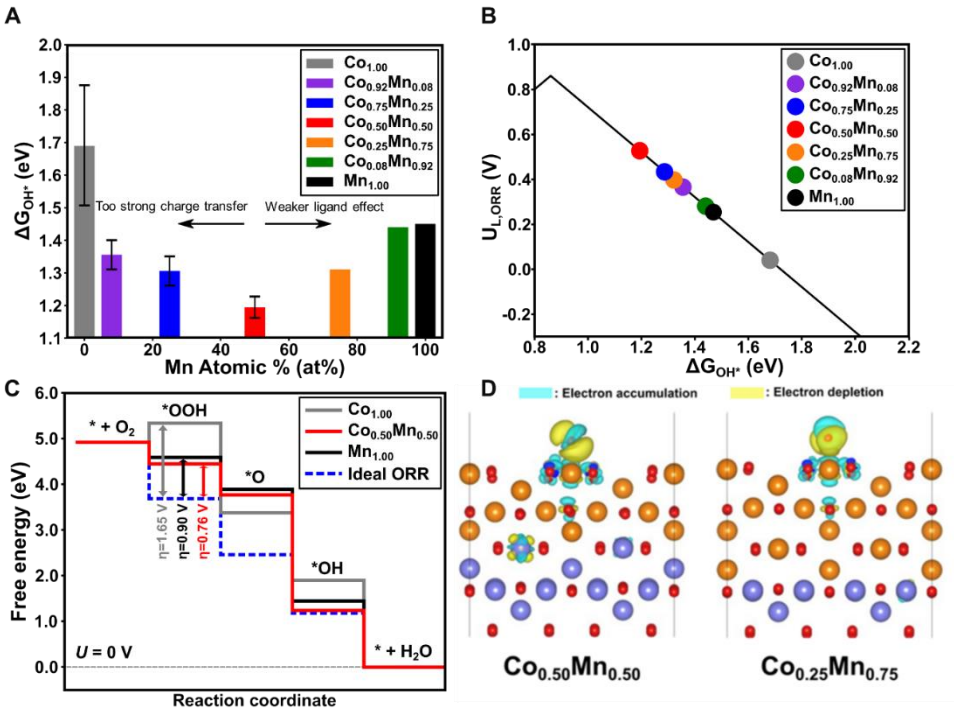

Figure 3.30. DFT calculations to understand the origin of ORR activity trend. (a) Average ΔG_{OH*} values of $Co_{1-x}Mn_x$. Error bars refer to standard deviations of ΔG_{OH*} for various models (see Computational Models of Spinel Oxides in the Supporting Information). (b) Theoretical ORR volcano plot to predict the limiting potential (U_L) from ΔG_{OH*} based on the standard scaling relation ($\Delta G_{OOH*} = \Delta G_{OH*} + 3.2$).[50] (c), The free energy diagram of four-electron associative ORR on $Co_{1-x}Mn_x$ (x = 0.0, 0.5, 1.0) at U = 0 V. Blue dashed line indicates the free energy diagram of the ideal catalyst. (d), Three-dimensional charge density difference upon *OH adsorption on $Co_{1-x}Mn_x$ (x = 0.5, 0.75). Blue and yellow regions indicate electron accumulation and depletion, respectively, where the isosurface level is set to 0.02 e/Å^3. Color codes: orange (Mn), blue (Co) and red (O).

3.4. Conclusion

In summary, the (001) facet-enclosed and strain-free Co-Mn spinel oxide surfaces can be synthesized from template-based epitaxial growth on Co_3O_4 nanocubes. Within the Co-Mn shell, both lattice and shear strain could be relieved due to the composition gradient. Under the facet- and strain-controlled environment, surface Mn/Co ratio could be manipulated to investigate the composition-dependent surface properties. On our well-defined oxide surface, the charge transfer from Mn to Co affects the valency of surface Mn cations in O_h-sites. Depending on the Mn/Co-atomic ratio, the ORR activity metrics shows volcano trend, and its origin is elaborated by close combination of experimental structure analyses and theoretical investigations. We believe that this facet- and strain-controlled oxide is a promising model platform to study the origin of improved catalytic activity on multimetallic nanomaterials in multiple (electro)catalytic applications.

** Parts of this chapter were published in the article, “Facet-Defined Strain-Free Spinel Oxide for Oxygen Reduction.” (*Nano Letters* **2022**, 22, 3636–3644.)

3.5. References

[1] Xie, C.; Niu, Z.; Kim, D.; Li, M.; Yang, P. *Chem. Rev.* **2020**, *120*, 1184–1249.

[2] Wang, X.; Ouyang, T.; Wang, L.; Zhong, J.; Liu, Z. *Angew. Chem. Int. Ed.* **2020**, *132*, 6554–6561.

[3] Núñez, M.; Lansford, J. L.; Vlachos, D. G. *Nat. Chem.* **2019**, *11*, 449-456.

[4] Strasser, P.; Gliech, M.; Kuehl, S.; Moeller, T. *Chem. Soc. Rev.* **2018**, *47* 715–735.

[5] Huang, L.; Zhang, X.; Wang, Q.; Han, Y.; Fang, Y.; Dong, S. *J. Am. Chem. Soc.* **2018**, *140*, 1142–1147.

[6] Stamenkovic, V. R.; Fowler, B.; Mun, B. S.; Wang, G.; Ross, P. N.; Lucas, C. A.; Markovic, N. M. *Science* **2007**, *315*, 493–497.

[7] Kang, Y.; Snyder, J.; Chi, M.; Li, D.; More, K. L.; Markovic, N. M.; Stamenkovic, V. R. *Nano Lett.* **2014**, *14*, 6361-6367.

[8] Xie, H.; Chen, F.; Nie, A.; Pu, T.; Rehwoldt, M.; Yu, D. Michael R. Zachariah,M. R.; Wang, C.; Shahbazian-Yassar, R.; Li, J.; Hu, L. *Science* **2018**, *359*, 1489–1494.

[9] Huang, L.; Zhang, X.; Han, Y.; Wang, Q.; Fang, Y.; Dong, S. *Chem. Mater.* **2017**, *29*, 4557−4562.

[10] Lu, Q.; Wang, A. L.; Gong, Y.; Hao, W.; Cheng, H.; Chen, J.; Li, B.; Yang, N.; Niu, W.; Wang, J.; Yu, Y.; Zhang, X.; Chen, Y.; Fan, Z.; Wu, X.-J.; Chen, J.; Luo, J.; Li, S.; Gu, L.; Zhang, H. *Nat. Chem.* **2018**, *10*, 1–6.

[11] van der Hoeven, J. E. S.; Jelic, J.; Olthof, L. A.; Totarella, G.; van Dijk-Moes, R. J. A.; Krafft, J.-M.; Louis, C.; Studt, F.; van Blaaderen, A.; de Jongh, P. E. *Nat. Mater.* **2021**, *20*, 1216-1220.

[12] Lyu, X.; Jia, Y.; Li, D.; Li, G.; Zhuang, L.; Wang, X.; Yang, D.; Wang, Q.; Du, A.; Yao, X. *Adv. Mater.* **2020**, *32*, 2003493.

[13] Yan, Y.; Shan, H.; Li, G.; Xiao, F.; Jiang, Y.; Yan, Y.; Jin, C.; Zhang, H.; Wu, J.; Yang, D. *Nano Lett.* **2016**, *16*, 7999–8004.

[14] Yuan, X.; Zhang, L.; Li, L.; Dong, H.; Chen, S.; Zhu, W.; Hu, C.; Deng, W.; Zhao, Z.-J.; Gong, J. *J. Am. Chem. Soc.* **2019**, *141*, 4791–4794.

[15] Luo, M.; Guo, S. *Nat. Rev. Mater.* **2017**, *2*, 1–14.

[16] Zhang, S.; Zhang, X.; Jiang, G.; Zhu, H.; Guo, S.; Su, D.; Lu, G.; Sun, S. *J. Am. Chem. Soc.* **2014**, *136*, 7734–7739.

[17] Li, J.; Sharma, S.; Wei, K.; Chen, Z.; Morris, D.; Lin, H.; Zeng, C.; Chi, M.; Yin, Z.; Muzzio, M.; Shen, M.; Zhang, P.; Peterson, A. A.; Sun, S. *J. Am. Chem. Soc.* **2020**, *142*, 19209–19216.

[18] Escudero-Escribano, M.; Malacrida, P.; Hansen, M. H.; Vej-Hansen, U. G.; Velázquez-Palenzuela, A.; Tripkovic, V.; Schiøtz, J.; Rossmeisl, J.; Stephens, I. E. L.; Chorkendorff, I. *Science*, **2016**, *352*, 73–76.

[19] Tang, C.; Zhang, N.; Ji, Y.; Shao, Q.; Li, Y.; Xiao, X.; Huang, X. *Nano Lett.* **2019**, *19*, 1336−1342.

[20] Han, S. I.; Lee, S. W.; Cho, M. G.; Yoo, J. M.; Oh, M. H.; Jeong, B.; Kim, D.; Park, O. K.; Kim, J.; Namkoong, E.; Jo, J.; Lee, N.; Lim, C.; Soh, M.; Sung, Y.-E.; Yoo, J.; Park, K.; Hyeon, T. *Adv. Mater.* **2020**, *32*, 2001566.

[21] Oh, M. H.; Cho, M. G.; Chung, D. Y.; Park, I.; Kwon, Y. P.; Ophus, C.; Kim, D.; Kim, M. G.; Jeong, B.; Gu, X. W.; Jo, J.; Yoo, J. M.; Hong, J.; McMains, S.; Kang, K.; Sung, Y.-E.; Alivisatos, A. P.; Hyeon, T. *Nature* **2020**, *577*, 359–363.

[22] Liang, Y.; Li, Y.; Wang, H.; Zhou, J.; Wang, J.; Regier, T.; Dai, H. *Nat. Mater.* **2011**, *10*, 780–786.

[23] Xia, W.; Mahmood, A.; Liang, Z.; Zou, R.; Guo, S. *Angew. Chem. Int. Ed.* **2016**, *55*, 2650–2676.

[24] Yang, Y.; Xiong, Y.; Holtz, M. E.; Feng, X.; Zeng, R.; Chen, G.; DiSalvo, F. J.; Muller, D. A.; Abruna, H. D. *Proc. Nat. Acad. Si. USA* **2019**, *116*, 24425-24432.

[25] Cheng, F.; Shen, J.; Peng, B.; Pan, Y.; Tao, Z.; Chen, J. *Nat. Chem.* **2011**, *3*, 79–84.

[26] Zhou, Y.; Sun, S.; Xi, S.; Duan, Y.; Sritharan, T.; Du, Y.; Xu, Z. J. *Adv. Mater*. **2018**, *30*, 1705407.

[27] Yang, Y.; Wang, Y.; Xiong, Y.; Huang, X.; Shen, L.; Huang, R.; Wang, H.; Pastore, J. P.; Yu, S-H.; Xiao, L.; Brock, J. D.; Zhuang, L.; Abruña, H. D. *J. Am. Chem. Soc.* **2019**, *141*, 1463–1466.

[28] Zhang, S. L.; Guan, B. Y.; Lu, X. F.; Xi, S.; Du, Y.; Lou, X. W. *Adv. Mater*. **2020**, *32*, 2002235.

[29] Kim, J.; Ko, W.; Yoo, J. M.; Paidi, V. K.; Jang, H. Y.; Shepit, M.; Lee, J.; Chang, H.; Lee, H. S.; Jo, J.; Kim, B. H.; Cho, S.-P.; van Lierop, J.; Kim, D.; Lee, K.-S.; Back, S.; Sung, Y.-E.; Hyeon, T.. *Adv. Mater*. **2021**, doi.org/10.1002/adma.202107868.

[30] Yang, Y.; Zheng, Y.; Cao, W.; Titov, A.; Hyvonen, J.; Manders, J. R.; Xue, J.; Holloway, P. H.; Qian, L. *Nat. Photonics* **2015**, *9*, 259-266.

[31] Kim, T.; Kim, K.-H.; Kim, S.; Choi, S.-M.; Jang, H.; Seo, H.-K.; Lee, H.; Chung, D.-Y.; Jang, E. *Nature* **2020**, *586*, 385-389.

[32] Kim, S.-W.; Zimmer, J. P.; Ohnishi, S.; Tracy, J. B.; Frangioni, J. V.; Bawendi, M. G. *J. Am. Chem. Soc.* **2005**, *127*, 10526-10532.

[33] Ding, Y.; Sun, X.; Lin Wang, Z.; Sun, S. *Appl. Phys. Lett.* **2012**, *100*, 111603.

[34] Bhattarai, N.; Casillas, G.; Ponce, A.; Jose-Yacaman, M. *Surf. Sci.* **2013**, *609*, 161–166.

[35] De Backer, A.; van den Bos, K. H. W.; Van den Broek, W.; Sijbers, J.; Van Aert, S. *Ultramicroscopy* **2016**, *171*, 104–116.

[36] Kim, K.-H. *Appl. Microsc.* **2015**, *45(2)*, 101–105.

[37] Rojas, R. M.; Vila, E.; Garcia, O.; de Vidales, J. L. M. *J. Mater. Chem.* **1994**, *4*, 1635–1639.

[38] Rask, J. H.; Miner, B. A.; Buseck, P. R. *Ultramicroscopy*, **1987**, *21*, 321–326.

[39] Restovic, A.; Rios, E.; Barbato, S.; Ortiz, J.; Gautier, J. L. *J. Electroanal. Chem.* **2002**, *522*, 141–151.

[40] Kim, H.; Yoon, G.; Park, I.; Park K. Y.; Lee, B.; Kim, J.; Park, Y.-U.; Jung, S.-K.; Lim, H.-D.; Ahn, D.; Lee, S.; Kang, K. *Energy Environ. Sci.* **2015**, *8*, 3325–3335.

[41] Carta, D.; Casula, M. F.; Falqui, A.; Loche, D.; Mountjoy, G.; Sangregorio, C.; Corrias, A. *J. Phys. Chem. C*, **2009**, *113*, 8606–8615.

[42] Zhou, Y.; Xi, S.; Wang, J.; Sun, S.; Wei, C.; Feng, Z.; Du, Y.; Xu, Z. J. *ACS Catal.* **2018**, *8*, 673-677.

[43] Eom, C. J.; Kuo, D.-Y.; Adamo, C.; Moon, E. J.; May, S. J.; Crumlin, E. J.; Schlom, D. G.; Suntivich, J. *Nat. Commun.* **2018**, *9*, 4034.

[44] Suntivich, J.; Gasteiger, H. A.; Yabuuchi, N.; Nkanishi, H.; Goodenough, J. B.; Shao-Horn, Y. *Nat. Chem.* **2011**, *3*, 546-550.

[45] Stoerzinger, K. A.; Risch, M.; Han, B.; Shao-Horn, Y. *ACS Catal.* **2015**, *5***,** 6021-6031.

[46] Ryabova, A. S.; Napolskiy, F. S.; Poux, T.; Istomin, S. Y.; Bonnefont, A.; Antipin, D. M.; Baranchikov, A. Y.; Levin, E. E.; Abakumov, A. M.; Kerangeven, G.; Antipov, E. V.; Tsirlina, G. A.; Savinova, E. R. *Electrochim. Acta* **2016**, *187***,** 161-172.

[47] Zhang, A.; Liang, Y.; Li, H.; Zhang, B.; Liu, Z.; Chang, Q.; Zhang, H.; Zhu, C.-F.; Geng, Z.; Zhu, W.; Zeng, J. *Nano Lett.* **2020**, *20*, 8229–8235.

[48] Viswanathan, V.; Hansen, H. A.; Rossmeisl, J.; Nørskov, J. K. *ACS Catal.* **2012**, *2*, 1654-1660.

[49] Back, S.; Jung, Y. *ChemCatChem* **2017**, *9*, 3173-3179.

[50] Kulkarni, A.; Siahrostami, S.; Patel, A.; Nørskov, J. K. Understanding catalytic activity trends in the oxygen reduction reaction. *Chem. Rev.* **2018**, *118*, 2302-2312.

[51] Ravel, B.; Newville, M. *J. Synchrotron Radiat.* **2005**, *12*, 537–541.

[52] Perdew, J. P.; Burke, K.; Ernzerhof, M. *phys. Rev. Lett.* **1996**, *77*, 3865.

[53] Blöchl, P. E. *Phys. Rev. B* **1994**, *50*, 17953.

[54] Kresse, G., Hafner, J. *Phys. Rev. B* **1993**, *48*, 13115.

[55] Monkhorst, H. J.; Pack, J. D. *Phys. rev. B* **1976**, *13*, 5188.

[56] Dudarev, S.; Botton, G.; Savrasov, S.; Humphreys, C.; Sutton, A. *Phys. Rev. B* **1998**, *57*, 1505.

[57] Larsen, A. H.; Mortensen, J. J.; Blomqvist, J.; Castelli, I. E.; Christensen, R.; Dułak, M.; Friis, J.; Groves, M. N.; Hammer, B.; Hargus, C. *J. Phys. Condens. Matter* **2017**, *29*, 273002.

[58] Peterson, A. A.; Nørskov, J. K. *J. Phys. Chem. Lett*. **2012**, *3*, 251–258.

Biography

1. International Publications

1) "Revealing Charge Transfer at the Interface of Spinel Oxide and Ceria during CO Oxidation"; Sinmyung Yoon, **Jinwoung Jo**, Beomjoon Jeon, Jihyeon Lee, Min Gee Cho, Myoung Hwan Oh, Beomgyun Jeong, Tae Joo Shin, Hu Young Jeong, Jeong Young Park, Taeghwan Hyeon, and Kwangjin An, *ACS Catalysis* **11**, 1516-1527 (2021).
2) "Facet-Defined Strain-Free Spinel Oxide for Oxygen Reduction"; **Jinwoung Jo**, Ji Mun Yoo, Dong Hyeon Mok, Ho Yeon Jang, Jiheon Kim, Wonjae Ko, Kyungbeen Yeom, Megalamane S. Bootharaju, Seoin Back, Yung-Eun Sung, Taeghwan Hyeon, *Nano Letters* **22**, 3636–3644 (2022).
3) "Design and synthesis of multigrain nanocrystals via geometric misfit strain"; Myoung Hwan Oh, Min Gee Cho, Dong Young Chung, Inchul Park, Youngwook Paul Kwon, Colin Ophus, Dokyoon Kim, Min Gyu Kim, Beomgyun Jeong, X. Wendy Gu, **Jinwoung Jo**, Ji Mun Yoo, Jaeyoung Hong, Sara McMains, Kisuk Kang, Yung-Eun Sung, A. Paul Alivisatos, Taeghwan Hyeon, *Nature* **577**, 359-363 (2020).
4) "Epitaxially Strained CeO_2/Mn_3O_4 Nanocrystals as an Enhanced Antioxidant for Radioprotection"; Sang Ihn Han, Sang-woo Lee,

Min Gee Cho, Ji Mun Yoo, Myoung Hwan Oh, Beomgyun Jeong, Dokyoon Kim, Ok Kyu Park, Junchul Kim, Eun Namkoong,, **Jinwoung Jo**, Nohyun Lee, Chaehong Lim, Min Soh, Yung-Eun Sung, Jongman Yoo, Kyungpyo Park, Taeghwan Hyeon, *Advanced Materials* **32**, 2001566 (2020).

5) "Structural Insights into Multi-Metal Spinel Oxide Nanoparticles for Boosting Oxygen Reduction Electrocatalysis"; Jiheon Kim, Wonjae Ko, Ji Mun Yoo, Vinod K. Paidi, Ho Yeon Jang, Michael Shepit, Jongmin Lee, Hogeun Chang, Hyeon Seok Lee, **Jinwoung Jo**, Byung Hyo Kim, Sung-Pyo Cho, Johan van Lierop, Dokyoon Kim, Kug-Seung Lee, Seoin Back, Yung-Eun Sung, and Taeghwan Hyeon, *Advanced Materials* **34**, 2107868 (2022).

6) "Enhanced hot electron generation by inverse metal–oxide interfaces on catalytic nanodiode"; Hyosun Lee, Sinmyung Yoon, **Jinwoung Jo**, Beomjoon Jeon, Taeghwan Hyeon, Kwangjin An, Jeong Young Park, *Faraday Discussions* **214**, 353-364 (2019).

7) "Shape-tunable multiplexed phototransistor array using stretchable colour-sensitive quantum dot nanocomposites"; Jun-Kyul Song, Junhee Kim, Jiyong Yoon, Ja Hoon Koo, Kyumin Kang, Hyunjin Jung, Sung-Hyuk Sunwoo, Seungwon Yoo, Hogeun Chang, **Jinwoung Jo**, Woonhyuk Baek, Sanghwa Lee, Mikyung Shin, Taeghwan Hyeon, Dae-Hyeong Kim, *Accepted*.

2. International Conferences

1) **Jinwoung Jo,** Taeghwan Hyeon; "Enhancement in CO Oxidation reactivity from the Charge Transfer through the Interface between Spinel Oxide and Ceria", Poster presentation at *KCS meeting Fall 2021, held at BEXCO, Busan, Korea, in October 2021*.

2) **Jinwoung Jo,** Taeghwan Hyeon; "Control of facet and strain on surface of spinel oxide nanocrystals for oxygen reduction", Poster presentation at *KIChE meeting Spring 2022, held at ICC, Jeju, Korea, in April 2022.*

초록

지난 수십년간, 여러 산화물을 한 나노입자 안에 접합시킨 구조인 이종구조 산화물 나노입자가 이종 핵형성을 이용한 콜로이드 합성법을 통해서 합성되어왔다. 나노입자 안에 생긴 특이한 계면 구조는 산화물 나노입자 자체의 촉매적 활성에 영향을 주어, 전기화학촉매, 유기촉매, 광촉매 등 여러 촉매 반응에 활성이 높은 산화물 촉매를 만들도록 도와주었다. 이 논문에서는 일산화탄소 산화 반응 및 전기 촉매적 산소 환원 반응을 연구하기 위해 계면이 조절된 코발트산화물-세륨산화물 나노입자와 노출면이 정해진 산화코발트-코발트/망간산화물 나노입자를 합성하는 방법을 제시한다.

먼저, 산화 세륨과 여러 스피넬 구조의 산화물 간의 계면을 조절한 나노큐브에 대한 새로운 합성법을 개발함으로서 산화물 촉매를 이용한 산화반응에서 계면의 역할을 탐색할 수 있었다. 세륨 산화물이 결합된 산화 코발트는 최대 12배 더 높은 일산화탄소 산화반응 활성을 나타냈다. 반응 도중 여러 분석 기법을 이용하여 결합된 산화세륨이 반응 중 부족해진 산소를 보충함으로써 활성이 높은 산화코발트의 환원을 막아준다는 것을 알 수 있었다. 3개의 면이 산화세륨으로 덮인 산화코발트

나노입자는 최대화된 계면 형성 정도를 보였으며, 이로 인해 산소가 결핍된 조건에서도 가장 높은 일산화탄소 산화반응 활성을 나타냈다. 이 연구는 산화물간의 계면에서 나노 규모에서 발생하는 산화반응의 메커니즘에 대한 깊은 이해를 제공하는 연구였다. 나노 다이오드를 사용하여 수소 산화 반응 도중 화학전류를 측정했을 때에도 동일한 경향이 나타났고, 이는 활성 향상의 기원이 계면에서의 전하 이동임을 보여준다.

둘째, 산화 코발트 나노큐브 템플릿 위에서 에피택시 성장을 사용하여 다양한 표면 조성을 가지고 (001) 면으로 뒤덮힌 스피넬 산화물 표면을 합성하였다. 조성의 기울기가 생기게 하여 층층이 스트레인이 완화하되게 하였고, 이로서 촉매 활성에 대한 표면 스트레인 효과를 최소화하였다. 이 시스템에서 실험과 계산을 통해 모델 산소 환원 반응 활성을 연구한 결과, 망간/코발트 비율에 따라 화산모양의 활성 경향을 그리는 것을 알 수 있었다. 최적의 전자 이동이 옥타헤드럴 위치의 망간에서 이웃 코발트로 일어나는 나노입자는 망간/코발트 비율이 1:1일 때였고, 이때 활성은 상용 백금 촉매와 비슷했고, 안정성 역시 매우 좋았다. 노출면과 표면 스트레인을 제어함으로써 전기 촉매 공정에서 조성-구조-활성 관계를 연구하기 위한 잘 정의된 플랫폼을 만드는데 성공하였다.

주요단어: 산화물, 이종구조, 촉매, 나노물질, 스피넬, 계면

학번: 2016-22356